https://doi.org/10.15388/vu.thesis.1012
https://orcid.org/0000-0002-0134-2286

VILNIUS UNIVERSITY
CENTER FOR PHYSICAL SCIENCES AND TECHNOLOGY

Pavel Piatrou

Investigation of Electromagnetic Processes During Magnetic Pulse Forming and Welding

DOCTORAL DISSERTATION

Natural Sciences,
Physics (N 002)

VILNIUS 2026

The dissertation was prepared between 2022 and 2026 at the Center for Physical Sciences and Technology.

Academic Supervisor – Prof. Dr. Voitech Stankevič **(**Center for Physical Sciences and Technology, Natural Sciences, Physics, N 002)

This doctoral dissertation will be defended in a public meeting of the Dissertation Defence Panel:

Chairman – Assoc. Prof. Dr. Zigmas Balevičius (Center for Physical and Technology Sciences and Technology, Natural Sciences, Physics, N 002).
Members:
Prof. Dr. Jonas Gradauskas (Center for Physical and Technology Sciences, Natural Sciences, Physics, N 002),
Prof. Dr. Habil. Marcin Morawiec (Gdańsk University of Technology, Technological Sciences, Electrical and Electronic Engineering, T 001),
Dr. Paulius Ragulis (Center for Physical Sciences and Technology, Natural Sciences, Physics, N 002),
Assoc. Prof. Dr. Nikolaj Višniakov (Vilnius Gediminas Technical University, Technological Sciences, Materials Engineering, T 008).

The dissertation shall be defended at a public meeting of the Dissertation Defence Panel at 10:00 on 3 December 2026 in Room/meeting room D401 of the State Research Institute Center for Physical Sciences and Technology.
Address: Saulėtekio ave., 3, D401, Vilnius, Lithuania
Tel. +37052649211; e-mail: office@ftmc.lt

https://doi.org/10.15388/vu.thesis.1012
https://orcid.org/0000-0002-0134-2286

VILNIAUS UNIVERSITETAS
FIZINIŲ IR TECHNOLOGIJOS MOKSLŲ CENTRAS

Pavel Piatrou

Elektromagnetinių procesų tyrimas magnetinio impulsinio formavimo ir suvirinimo metu

DAKTARO DISERTACIJA

Gamtos mokslai,
Fizika, (N 002)

VILNIUS 2026

Disertacija rengta 2022–2026 metais Fizinių ir technologijos mokslų centre.

Mokslinis vadovas – prof. dr. Voitech Stankevič (Fizinių ir technologijos mokslų centras, gamtos mokslai, fizika, N 002).

Gynimo taryba:
Pirmininkas – doc. dr. Zigmas Balevičius (Fizinių ir technologijos mokslų centras, gamtos mokslai, fizika, N 002).
Nariai:
prof. dr. Jonas Gradauskas (Fizinių ir technologijos mokslų centras, gamtos mokslai, fizika, N 002),
prof. habil. dr. Marcin Morawiec (Gdansko technologijos universitetas, Lenkija, technologijos mokslai, elektros ir elektronikos inžinerija, T 001),
dr. Paulius Ragulis (Fizinių ir technologijos mokslų centras, gamtos mokslai, fizika, N 002),
doc. dr. Nikolaj Višniakov (Vilniaus Gedimino technikos universitetas, technologijos mokslai, medžiagų inžinerija, T 008).

Disertacija ginama viešame / uždarame Gynimo tarybos posėdyje 2026 m. gruodžio mėn. 3 d. 10 val. Valstybinio mokslinių tyrimų instituto Fizinių ir technologijos mokslų centro D401 posėdžių salėje.
Adresas: Saulėtekio al., 3, D401, Vilnius, Lietuva
Tel. +37052649211; el. paštas: office@ftmc.lt

LIST OF ABBREVIATIONS

CFRP – Carbon Fibre Reinforced Polymer
CMR – Colossal Magnetoresistance
EMF – Electromotive Force
EMPT – Electromagnetic pulse technology
EXW – Explosion Welding
FEM – Finite Element Method
FM – Ferromagnetic
FS – Field Shaper
MPC – Magnetic Pulse Crimping
MPF – Magnetic Pulse Forming
MPP – Magnetic Proximity Probe
MPW – Magnetic Pulse Welding
MR – Magnetoresistance
PDV – Photonic Doppler Velocimetry
PI-MOCVD - pulsed-injection metal-organic chemical vapor deposition
PSD – Position Sensitive Detector
PTFE – Polytetrafluoroethylene
TEM – Transmission Electron Microscopy
UAS – Unmanned Aerial Systems
XRD – X-ray diffraction

CONTENTS

INTRODUCTION 9
The Aim of the Work 11
Objectives 12
Scientific Novelty 12
Practical Value of the Research Findings 13
Statements to defend 14
Author contribution 15
Structure of the thesis 16
Acknowledgements 17
LIST OF PUBLICATIONS 18
1 LITERATURE REVIEW 20
1.1 Electromagnetic Pulse Technology for Forming and Welding 20
1.2 Tool Coils in Electromagnetic Pulse Technology 30
1.3 Application of Electromagnetic Pulse Technology 33
1.3.1 Magnetic Pulse Forming 33
1.3.2 Magnetic Pulse Welding and Cladding 33
1.3.3 Magnetic Pulse Crimping 37
1.3.4 Magnetic Pulse Cutting 37
1.4 Experimental Diagnostics and Monitoring of EMPT parameters 38
1.4.1 Discharge Current and Voltage Measurements 38
1.4.2 Flyer Velocity and Displacement Measurement 39
1.4.2.1 Optical sensors 39
1.4.2.2 Magnetic proximity sensors 41
1.4.3 Impact Time and Collision Velocity Detection 42
1.4.4 Magnetic Field Measurement 43
1.5 Post-Process Control in EMPT 49
1.6 FEM-Based Modelling of EMPT Processes 50
1.7 Conclusions of Chapter 1 53

2 METHODOLOGY 54
2.1 Magnetic Pulse Welding Setup 54
2.2 Materials and Workpiece 56
2.3 Experimental Setup for Proximity Sensing 58
2.4 Electrical Measurements 59
2.5 CMR B-scalar sensor 60
2.6 Magnetic Field Measurement Probes and System 60
2.7 Numerical Modelling in COMSOL Multiphysics 62
2.8 Tensile Testing and Joint Characterisation 64
2.9 Conclusions of Chapter 2 66
3 RESULTS AND DISCUSSION 67
3.1 Short Pulsed Magnetic Field Measurements 67
3.1.1 Magnetic Field Meter with EMF Compensation 67
3.1.2 Experimental Validation of the Magnetic Field Meter in Pulsed Magnetic Field 70
3.1.3 Conclusions of Section 3.1 72
3.2 Magnetic Field Probes Designs 73
3.2.1 Low Resistivity CMR B-Scalar Sensor 73
3.2.2 CMR B-Scalar Magnetic Field Probes for MPW Investigation 74
3.2.3 Conclusions of Section 3.2 78
3.3 Investigation of Magnetic Field Dynamics in the Gap Between the Flyer and Field Shaper During MPW Process 79
3.3.1 Current Measurement 79
3.3.2 Magnetic Field Measurement 80
3.3.3 Analysis of Experimental Results 86
3.3.4 Coupled Electromagnetic–Mechanical Modelling of MPW Process 89
3.3.5 Tensile Testing of the Welded Joints 91
3.3.6 Conclusions of Section 3.3 95
3.4 Magnetic Proximity Sensing in the MPW Setup Using a CMR B-Scalar Sensor 97

3.4.1 Principle and Configuration of CMR-Based Proximity Probe..... 97
3.4.2 CMR-based MPP Measurements 100
3.4.2.1 Proximity Measurement to a Stationary Ferromagnetic Plate.... 100
3.4.2.2 Proximity Measurement of Rotating Ferromagnetic and Non-Ferromagnetic Disks 101
3.4.3 Modelling of CMR-based MPPs..... 103
3.4.4 Application of the Proximity Sensing Principle to MPW 106
3.4.5 Conclusions of Section 3.4..... 109
GENERAL CONCLUSIONS 111
SANTRAUKA 113
ĮVADAS..... 113
Tikslas 114
Tyrimo uždaviniai 114
Mokslinis naujumas..... 115
Praktinė vertė..... 116
Ginamieji teiginiai..... 117
1. LITERATŪROS APŽVALGA 118
2. METODOLOGIJA 119
3. REZULTATAI IR APTARIMAS 122
3.1 Trumpų didelės amplitudės magnetinio lauko impulsų matavimai.. 122
3.2 CMR B-skaliarinių magnetinio lauko jutiklių kūrimas..... 125
3.3 Elektromagnetinių ir mechaninių procesų tyrimas magnetinio impulsinio suvirinimo metu..... 128
3.4 Magnetinio artumo matavimų CMR B-skaliariniais jutikliais tyrimas.. 139
BENDROSIOS IŠVADOS..... 144
PUBLIKACIJŲ SARAŠAS 145
CURRICULUM VITAE 147
REFERENCES..... 148

INTRODUCTION

The increasing demand for lightweight, energy-efficient, and high-performance engineering structures has accelerated the use of hybrid components manufactured from dissimilar metallic materials [1, 2, 3]. Such components combine the advantages of different materials, enabling improvements in mechanical strength, weight reduction, corrosion resistance, and thermal performance [4, 5, 6, 7]. Consequently, advanced manufacturing technologies capable of forming and joining dissimilar metallic components have become increasingly important in the automotive, aerospace, and robotics industries.

Electromagnetic pulse technology (EMPT) is a family of high-speed, non-contact manufacturing processes used for forming, welding, crimping, cladding, and cutting electrically conductive materials [8, 9]. It employs high-current capacitor discharges through a tool coil to generate transient magnetic fields that exert electromagnetic forces on the electrically conductive workpiece, causing its rapid deformation.

The underlying physics is governed by the coupling of electromagnetic induction and the Lorentz force. According to Faraday's law, a rapidly changing magnetic flux induces eddy currents in the electrically conductive workpiece. The interaction of these currents with the magnetic field produces a Lorentz body force $\vec{f} = \vec{J} \times \vec{B}$. Due to the skin effect, the induced currents are concentrated within a thin surface layer of the workpiece, localising the electromagnetic force near its surface. Integrating the normal component of this force over the thickness of the workpiece provides an effective magnetic pressure, $p = B^2 / 2\mu_0$, acting on the workpiece surface [10]. This impulsive magnetic pressure can accelerate the workpiece to velocities of the order of hundreds of meters per second within a few microseconds [8]. This physical principle is exploited in magnetic pulse forming (MPF) [8, 9], magnetic pulse welding (MPW) [11], and magnetic pulse crimping (MPC) [12], in which the magnetic pressure is used, respectively, to shape tubular and sheet workpieces, to produce solid-state joints between similar and dissimilar metals, and to compress a tube radially onto a fitting or conductor.

The application of magnetic pressure offers several advantages in modern manufacturing. Because the pressure is applied without mechanical contact, tool wear, surface damage, and the need for lubricants are avoided, and the absence of moving tooling makes the process readily automated and suitable for integration into manufacturing lines for mass production [9, 13]. In forming operations, the high strain rates attained extend the forming limits of

many alloys and suppress springback [8]. In welding applications, joining is achieved without bulk melting of the workpieces, so that heat-affected zones, filler materials, and shielding gases inherent to fusion welding are avoided, making MPW an environmentally favourable alternative to conventional joining technologies [8, 14].

Despite these advantages, EMPT processes are governed by a sequence of energy conversions that is difficult to follow experimentally: electrical energy stored in the capacitor is transferred into the energy of the transient magnetic field, part of which is converted into kinetic energy of the workpiece and subsequently dissipated as plastic deformation work and, in MPW, in the impact process. These conversions are also difficult to describe analytically, because the electrical, electromagnetic, and mechanical phenomena evolve simultaneously and influence one another.

This mutual influence is most clearly seen in the deformation itself. As the workpiece deforms, the gap between the field-generating tool and the workpiece changes, modifying the mutual inductance of the tool–workpiece system; this in turn affects the discharge current. The altered current and the deformed geometry together reshape the field distribution in the gap, and hence the magnetic pressure acting on the workpiece. Thus, the deformation feeds back on the magnetic pressure that generates it, and neither the field nor the motion of the workpiece can be determined independently of the other.

Finite-element modelling has therefore become an important tool for analysing these processes, based on the simultaneous numerical solution of Maxwell's equations in the quasi-static approximation, the equations of motion of the deforming workpiece, and the equations of the discharge circuit [15, 16]. Such a model requires as input the geometry of the electromagnetic system, the electrical and magnetic properties of the materials, the parameters of the discharge circuit, and the mechanical and constitutive behaviour of the workpiece. Its solution provides the time evolution of quantities such as the discharge current, the magnetic field, the magnetic pressure, and the deformation and velocity of the workpiece. Experimental measurement of one or more of these quantities is required to assess the accuracy of the model.

Among these quantities, the magnetic field in the gap between the field-generating tool and the workpiece is the one that determines the magnetic pressure, and hence the force driving the deformation. Direct measurement of the field in the gap therefore provides the data required to validate the electromagnetic part of coupled numerical models. Obtaining such data is experimentally demanding. The combination of high magnetic-field amplitudes (of the order of tens of tesla), rapid temporal variations of the field (rise times of a few microseconds), and strong electromagnetic interference

imposes stringent requirements on the measurement system. Moreover, the limited accessibility and small dimensions of the gap restrict both the placement and the size of the sensor [17, 18].

Several measurement principles have been applied to transient magnetic fields in magnetic pulse processes, but each is constrained within the gap itself. Inductive (B-dot) probes measure dB/dt and require integration of a signal that is itself exposed to interference [19]. Hall sensors respond to a single field component and therefore require precise orientation [17]. Fibre-optic probes based on the Faraday effect are sensitive to the mechanical vibration [20]. Colossal magnetoresistance (CMR) B-scalar sensor [21] have been used to record the magnetic field during MPW [18]. In that configuration, however, the sensor was placed in a hole drilled in the field-generating tool, so that the measurement itself perturbs the induced current distribution in the tool, and hence the magnetic pressure in the region where the field is measured.

This dissertation addresses these challenges through experimental investigation of the magnetic-field dynamics during MPW. The work focuses on non-invasive measurement of the transient field in the gap between the field-generating tool and the workpiece using a CMR B-scalar probes, and on correlating the measured field evolution with the discharge current, the workpiece deformation, and finite-element simulations. A coupled electromagnetic–mechanical model that accounts for the dynamically changing gap between the field-generating tool and the workpiece is developed and validated against the measured field dynamics. These results provide new experimental insight into the electromagnetic–mechanical interactions governing EMPT processing, and demonstrate that direct in-gap field measurements enable identification of the onset of plastic deformation and of the impact instant, while the validated model yields the flyer velocity.

The Aim of the Work

The aim of this work is to investigate the transient electromagnetic and mechanical processes occurring during magnetic pulse welding by means of direct, time-resolved measurement of the magnetic field in the field shaper–workpiece gap, using a non-invasive measurement method developed for this purpose in combination with coupled numerical modelling.

Objectives

1. To develop a measurement method for high-amplitude transient magnetic fields in electromagnetic pulse technologies, providing suppression of the parasitic electromotive force induced in the probe wiring and probe dimensions compatible with a field shaper–flyer gap of 0.6 mm.
2. To measure the dynamics of the magnetic field in the gap between the field shaper and the flyer workpiece during magnetic pulse welding, for different standoff distances and discharge energies.
3. To develop a coupled electromagnetic–mechanical 2D axisymmetric finite element model of magnetic pulse welding in which the gap between the field shaper and the flyer is treated as a deforming domain, so that the deformation of the flyer acts back on the field distribution in the gap, and to verify the model against the measured field waveform and the measured instant of impact.
4. To identify, from the measured magnetic field waveform and its time derivative, the characteristic stages of the process — the onset of deformation of the flyer, its motion, and its collision with the parent — and to determine their instants of occurrence.
5. To relate the measured field dynamics and the calculated flyer velocity before impact to the strength of the resulting joint.
6. To establish whether the magnetic field recorded after the impact carries information on the final position of the flyer surface, and thereby whether the same measurement yields both the dynamics of the process and the final geometry of the welded assembly.

Scientific Novelty

1. A non-invasive experimental method was developed for direct measurement of transient magnetic fields inside the working gap of magnetic pulse welding systems, enabling magnetic-field measurements under actual welding conditions without modifying the technological tooling.
2. A coupled electromagnetic–mechanical 2D axisymmetric finite-element model was developed with a deformable air-gap mesh that follows flyer workpiece deformation during magnetic pulse welding. This approach allows the dynamically changing gap between the field shaper and the flyer tube to be incorporated into the simulation and enables reproduction of the experimentally observed magnetic-field dynamics.

3. It was experimentally demonstrated that the temporal evolution of the measured magnetic field directly reflects flyer deformation and collision dynamics, providing a new experimental approach for investigating magnetic pulse welding.
4. The possibility of using a CMR B-scalar sensor as a magnetic proximity sensor was demonstrated using two excitation approaches: a permanent magnet and the pulsed magnetic field generated by the welding coil. This enabled proximity-based evaluation of final flyer position within a single MPW cycle.

Practical Value of the Research Findings

1. An experimental magnetic pulse welding setup was developed and implemented at the State Research Institute Center for Physical Sciences and Technology (FTMC). This setup enables investigation of MPW processes under high-current pulsed conditions and also provides a platform for testing magnetic-field measurement systems and sensor probes.
2. Thin-wire probes and probes integrated on flexible printed circuit boards were developed using CMR B-scalar sensors. These probes can be placed in narrow and difficult-to-access regions of an MPW system, including the field shaper–flyer gap of 0.6 mm. Together with the measurement module developed in this work, they allow magnetic field pulses of about 16 μs duration and amplitudes up to 20 T to be recorded under the strong electromagnetic interference characteristic of electromagnetic pulse technology.
3. A coupled electromagnetic–mechanical finite element model in which the field shaper–flyer gap is treated as a deforming domain was developed and verified against the measured field waveform and the measured instant of impact. The model yields the flyer velocity before impact for a given discharge energy and standoff distance, and can therefore be used to select these parameters when designing a welding operation.
4. It was shown that the magnetic field recorded in the gap during a single discharge yields both the instants of the mechanical events of the process and the final position of the flyer surface after welding, so that no additional displacement or position sensor is required. This makes the measurement applicable to the monitoring of repeated welding operations on an existing setup, since the probe occupies only the gap that is present in any case.

5. The work extends the CMR B-scalar sensor technology developed at FTMC to two new fields of application, electromagnetic pulse welding and magnetic proximity sensing of metallic objects.

Statements to defend

1. Compact CMR B-scalar probes based on $La_{0.8}Sr_{0.2}Mn_{1.15}O_3$ thin films, fabricated on flexible PCBs, enable non-invasive magnetic-field measurements in field shaper–flyer gaps as narrow as 0.6 mm. Bipolar square-wave excitation of the probe, implemented in the developed measurement module, suppresses parasitic electromotive forces in the sensor wiring, enabling transient magnetic-field measurements, with fields up to 20 T and pulse durations as short as 16 μs.
2. The magnetic flux density dynamics measured in the field shaper–flyer gap using the developed measurement system with the subsequent data analysis provides experimental information on the magnetic pulse welding process including determination of the onset and subsequent dynamics of the flyer deformation, the instant of flyer–parent impact and the final position of the flyer during magnetic pulse welding.
3. Incorporating a deforming air-gap domain between the field shaper and the flyer, with a mesh size no larger than the initial field shaper–flyer gap, into the coupled electromagnetic–mechanical COMSOL Multiphysics model enables simulation of the changing geometry caused by the radial motion of the flyer, as well as the resulting magnetic flux density variation in time and flyer radial velocity. The simulated flyer–parent impact time and peak magnetic flux density agree with the measured values within 5% and 8%, respectively.
4. Due to proximity-sensing mechanism, the magnetic flux density dynamics measured after flyer–parent impact depends on the final radial position of the flyer relative to the field shaper. This position can be determined from the second and subsequent half-waves of the magnetic-field waveform, during the same capacitor discharge that provides information on flyer deformation and impact dynamics within the first half-wave. The relative uncertainty of the position determination does not exceed 5.5% over the investigated range of field shaper–flyer distances. Consequently, measurement of the magnetic field dynamics, together with the simulated flyer impact velocity and the tensile-test results, makes it possible to relate the welding parameters to the quality of the resulting joint.

Author contribution

The author designed, assembled and commissioned the experimental magnetic pulse welding setup at FTMC, including the practical implementation of its main components and the selection of the capacitor. He programmed and configured the industrial controller used for the operation and the safety functions of the setup.

The author fabricated and tested the CMR B-scalar probes. He deposited the electrical contacts on the CMR thin-film structures and measured the electrophysical characteristics of films with different Mn excess. On the basis of these measurements he selected the sensing structures and integrated them manually into the probe assemblies, which included the preparation of bifilar twisted wires, soldering to the sensor contacts, passivation of the sensor, shielding and electrical insulation. He calibrated the completed probes in magnetic fields at different temperatures.

Together with the developers of the measurement system, the author contributed to the testing and optimisation of the microsecond-duration pulsed magnetic field meter under short-pulse conditions within the project 3400-PL612, No. P-TPP-23-081, "Microsecond Duration Pulsed Magnetic Field Meter", and prepared materials for the project report.

The author designed and manufactured by 3D printing the holders for the proximity probes and for the placement of the probe inside the field shaper, which fixed the probe position and protected the sensor from mechanical damage during the MPW experiments.

The author carried out the measurements of the discharge current and of the magnetic field dynamics during MPW, processed the recorded waveforms, and interpreted them in terms of the deformation and impact of the flyer tube.

The author developed the coupled electromagnetic–mechanical 2D axisymmetric finite element model of the MPW process. The principal difficulty was that the gap between the field shaper and the flyer changes during the pulse; the author resolved it by introducing a deforming mesh in the gap, which gives two-way coupling in which the electromagnetic field accelerates the flyer while the resulting displacement changes the gap and, with it, the transient field distribution.

The author planned the programme of tensile testing, selected the combinations of discharge energy and standoff distance to be examined, produced the welded specimens and prepared them for testing. The tensile tests and the optical microscopy of the separated surfaces were performed by colleagues at Vilnius TECH university. The author processed and interpreted

the resulting load–displacement curves and micrographs and related them to the magnetic field measurements and to the calculated flyer velocity.

The author investigated the use of CMR B-scalar sensors as magnetic proximity sensors, with a permanent magnet and with the pulsed field of the welding coil as the excitation source, performed the measurements with stationary and rotating targets, and built the finite element model of the magnet–target system.

The author processed and interpreted the experimental and numerical results, prepared the text and the figures of the dissertation and the first drafts of the related publications, and presented the results at international and national conferences.

Structure of the thesis

The thesis consists of an introduction, three chapters, general conclusions, a summary in Lithuanian, a list of publications and a list of references.

The first chapter is a literature review. It covers the physical principles of magnetic pulse welding, the generation of pulsed magnetic fields and their interaction with conductive workpieces, existing approaches to measuring magnetic fields and flyer motion in electromagnetic pulse technology, and the properties of manganite-based CMR B-scalar sensors.

The second chapter describes the methods: the experimental MPW setup, the materials and workpiece geometry, the CMR B-scalar probes and the magnetic field measurement system developed in this work, the procedures for measuring the discharge current and the magnetic field, the coupled electromagnetic–mechanical 2D axisymmetric finite element model, and the tensile testing of the welded joints.

The third chapter presents the results in four sections. The first covers the measurement of short high-amplitude magnetic field pulses and the suppression of the parasitic EMF in the measurement module. The second describes the low-resistance CMR B-scalar sensors and the probe designs that allow measurements in a 0.6 mm gap. The third analyses the magnetic field dynamics in the field shaper–flyer gap during MPW, relates features of the measured waveform to the deformation and impact of the flyer, compares them with the numerical model, and examines the strength of the resulting joints. The fourth investigates CMR B-scalar sensors for proximity sensing, both with a permanent magnet as the excitation source and within the MPW setup itself, where the final flyer position after welding is obtained from the same measurement.

Acknowledgements

I am sincerely grateful to my supervisor, Prof. Dr. Voitech Stankevič, for his guidance, support and encouragement throughout my doctoral studies, for introducing me to a demanding and rewarding research topic, and for the opportunity to develop my scientific and experimental skills in this field.

I thank the Head of the Department, Prof. Dr. Nerija Žurauskienė, for her advice, consultations and continued support, and for the friendly and stimulating environment in which I have built my scientific career.

I am deeply grateful to Prof. Dr. Saulius Balevičius for sharing his experience in preparing and presenting research results for publication, for scientific discussions and for his encouragement.

My thanks go to Dr. Skirmantas Keršulis for valuable scientific discussions and for his help with the experimental work and the instrumentation.

I am especially grateful to Dr. Vilius Vertelis, Jorūnas Dobilas and Dr. Elisabetta Sieni for their help with the numerical modelling of the electromagnetic and mechanical processes studied here.

I thank Dr. Valentina Plaušinaitienė and Dr. Milita Vagner for preparing the CMR thin films used in this work.

I sincerely thank Dr. Mindaugas Viliūnas, Dr. Algirdas Baškys, Dr. Martynas Šapurov, Dr. Vytautas Bleizgys, Dr. Justas Dilys and the staff of UAB Geozondas for developing the new-generation magnetic field measurement system used here.

I thank Dr. Vitalijus Rudzinskas for carrying out the tensile tests of the welded joints and for his help in interpreting the results.

My deepest gratitude goes to my family, and especially to my parents, who always encouraged me to pursue science. Sadly, they did not live to see this moment, but their support and their belief in me have remained with me throughout. I dedicate this achievement to their memory.

I am deeply grateful to my wife, Palina, for her love, empathy, understanding and patience, and for choosing to share her life with me through the demanding period of completing this dissertation.

Finally, I thank all the teachers and colleagues I have had the privilege of meeting on my academic and professional journey. Each of them, in different ways, shaped my development as a researcher, an engineer and a person.

LIST OF PUBLICATIONS

Basis of the thesis

(A1) Balevičius, Saulius; **Piatrou, Pavel**; Vertelis, Vilius; Stankevič, Voitech; Keršulis, Skirmantas; Dobilas, Jorūnas; Dilys, Justas; Žurauskienė, Nerija. Magnetic proximity sensor based on colossal magnetoresistance effect. Sensors and Actuators A: Physical, 375, 2024, 115518. doi: 10.1016/j.sna.2024.115518

(A2) **Piatrou, Pavel**; Stankevic, Voitech; Zurauskiene, Nerija; Kersulis, Skirmantas; Viliunas, Mindaugas; Baskys, Algirdas; Sapurov, Martynas; Bleizgys, Vytautas; Antonovic, Darius; Plausinaitiene, Valentina; Skapas, Martynas; Vertelis, Vilius; Levitas, Borisas. Magnetic Field Meter Based on CMR-B-Scalar Sensor for Measurement of Microsecond Duration Magnetic Field Pulses. Sensors, 25(6), 2025, 1640. doi: 10.3390/s25061640

(A3) **Pavel Piatrou**, Voitech Stankevic, Skirmantas Kersulis, Vilius Vertelis, Elisabetta Sieni, Vitalijus Rudzinskas, Jorunas Dobilas, Milita Vagner, Nerija Zurauskiene, Direct Measurement Of Magnetic Field Dynamics For Characterization Of Magnetic Pulse Welding Process. IEEE Access, 2026. doi: 10.1109/ACCESS.2026.3715879

Other publications

(A4) Sapurov, Martynas; Baskys, Algirdas; Slivka, Kazimieras; Bleizgys, Vytautas; Stasys, Karolis; Simniskis, Rimantas; Zlosnikas, Valerijus; Urbonas, Kęstutis; Dervinis, Aldas; Paulikas, Sarunas; Paulauskas, Nerijus; Pomarnacki, Raimondas; Gursnys, Darius; Mazeiko, Leslav; Cymliakova, Violeta; **Piatrou, Pavel**; Dilys, Justas. “ RF power saving system for smart homes.” – Heliyon, 10(21), 2024, e39862.
doi: 10.1016/j.heliyon.2024.e39862

List of conference presentations

(C1) V. Stankevič, **P. Piatrou**, N. Žurauskienė, S. Keršulis, Magnetic Field Measurement in Magnetic Pulse Forming and Welding Systems, Workshop on IEEE MTTW Conference, Riga Technical University, Latvia, October 4-6, 2023

(C2) **P. Piatrou**, J. Dobilas, V. Stankevič, Magnetic Field Dynamics During Magnetic Pulse Forming, Workshop on IEEE MTTW Conference, Riga Technical University, Latvia, October 4-6, 2023

(C3) **P. Piatrou**, V. Vertelis, V. Stankevič, S. Keršulis, J. Dilys, V. Rudokas, V. Bleizgys, V. Plaušinaitiene, M. Viliūnas, N. Žurauskienė, Short Pulsed Magnetic Field Measurement System for Analysis of Magnetic Field Dynamics During Magnetic Pulse Welding and Forming, 10th Euro-Asian Pulsed Power Conference (EAPPC 2024), Amsterdam, Netherlands, September 22 to 26, 2024.

(C4) **P.Piatrou**, V. Stankevič, Magnetic Field Dynamics During Magnetic Pulse Forming And Crimping, FTMC Doctoral and Young Scientists Conference FizTeCh2024, October 15–17 2024

(C5) **P. Piatrou**, V. Stankevic, N. Žurauskienė, S. Keršulis, V. Vertelis, Recent Advances In The Study Of Magnetic Field Dynamics During Magnetic Pulse Crimping, 12th IEEE Workshop on Advances in Information, Electronic and Electrical Engineering (AIEEE'2025), Vilnius, Lithuania, May 15–17, 2025.

(C6) **P. Piatrou**, V. Stankevič, S. Keršulis, V. Vertelis, N. Žurauskienė Magnetic Lauko Dinamika Magnetinio Impulsinio Suvirinimo Procese. 46-oji Lietuvos nacionalinė fizikos konferencija, 2025 m. spalio 8 – 10 d. KTU, Kaunas, Lietuva

(C7) **P.Piatrou**, V. Stankevič, Investigation Of Electromagnetic Processes During Magnetic Pulse Forming And Welding, FTMC Doctoral and Young Scientists Conference FizTeCh2025 October 21–22 2025

(C8) **P. Piatrou**, V. Stankevic, S. Kersulis and N. Zurauskiene Investigation Of Transient Processes in Magnetic Pulse Welding System Using CMR B-scalar Sensors, Advanced Properties and Processes in Optoelectronic Materials and Systems (20th APROPOS), Vilnius, Lithuania, 30 September – 2 October 2026.

1 LITERATURE REVIEW

1.1 Electromagnetic Pulse Technology for Forming and Welding

In this dissertation, the term electromagnetic pulse technology (EMPT) refers to a family of non-contact manufacturing processes in which pulsed magnetic fields generated by a tool coil are used to accelerate and deform electrically conductive workpieces. Depending on the geometry of the tool coil, the workpiece, and the auxiliary tooling, these manufacturing processes can be used to perform forming, welding, crimping, cladding, and cutting operations on tubular, sheet, and profile-shaped workpieces [8, 9].

The underlying mechanism driving these processes is the electromagnetic force generated by the interaction between the induced currents in the workpiece and the pulsed magnetic field produced by the tool coil (Fig. 1.1). Treating the workpiece as a continuous conductive medium, this interaction can be described by a body force distributed through its volume. In general, the electromagnetic body force density f (N/m³) consists of the electric force density $\rho_e E$ (N/m³), associated with the volume charge density ρ_e (C/m³) and the electric field strength E (V/m), and the magnetic force density $J \times B$ (N/m³), associated with the induced current density J (A/m²) and the magnetic flux density B (T) [22]:

$$\vec{f} = \rho_e \vec{E} + \vec{J} \times \vec{B}, \tag{1.1}$$

In metallic workpieces the material is usually treated as quasi-neutral, and the electric term $\rho_e E$ is therefore neglected; the mechanical loading is then governed by the magnetic term alone:

$$\vec{f} = \vec{J} \times \vec{B}, \tag{1.2}$$

In typical EMPT configurations, the geometry of the tool coil and the workpiece are selected so that the dominant component of f acts along the required direction of deformation [8]. For tubular workpieces, this force is predominantly radial and can be used for compression, expansion, crimping, welding or cladding. For sheet workpieces, it acts mainly normal to the surface and can be used for forming, welding, or cutting.

By Faraday's law of induction, a time-varying magnetic field produces an induced electric field in a nearby conductive workpiece and, with it, eddy currents. The magnetic field in EMPT has a characteristic frequency in the kilohertz range [8], so these currents are concentrated near the surface of the workpiece. The decay of the current density with depth below the conductor surface can be described by:

$$J(x) = J_0 e^{-x/\delta}, \tag{1.3}$$

where $J(x)$ (A/m^2) is the current density at depth x (m); J_0 (A/m^2) is the current density at the surface; and δ (m) is the skin depth [23]. For a harmonic current, the skin depth can be estimated as:

$$\delta = \sqrt{\frac{2}{\omega\mu\sigma}}, \tag{1.4}$$

where ω (rad/s) is the angular frequency of the current; μ (H/m) is the magnetic permeability; and σ (S/m) is the electrical conductivity of the material [23]. This expression shows that the induced currents become more localised near the surface when the frequency, electrical conductivity, or magnetic permeability increases.

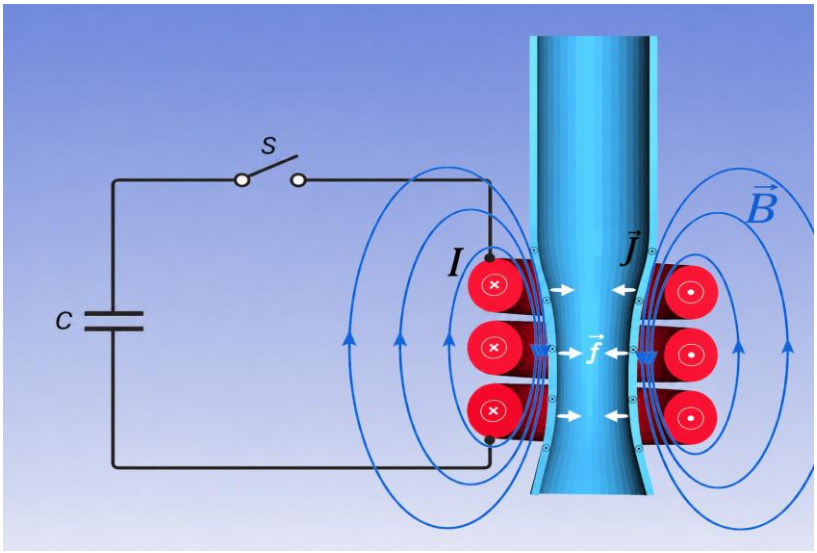


Fig. 1.1 Cross-section of the electromagnetic interaction between a cylindrical tool coil and a conductive tube. The coil current I generates an axial magnetic field of flux density $\boldsymbol{B}$, which induces an eddy current density $\boldsymbol{J}$ in the tube wall. The symbols ⊙ and ⊗ denote current directed out of and into the plane of the figure, respectively. The resulting Lorentz force density $\boldsymbol{f} = \boldsymbol{J} \times \boldsymbol{B}$ (Eq. 1.2) is directed radially inwards and compresses the tube.

The skin depth is an important parameter for EMPT, because for the magnetic pressure to act efficiently, the workpiece thickness should be larger than the skin depth. In this case, the electromagnetic body force density is mainly localised within the near-surface skin layer. When this distributed force is represented as a surface load, the equivalent magnetic pressure can be obtained by integrating the normal component of the electromagnetic body force density over the thickness of the workpiece. Following Psyk et al. [8], the magnetic pressure can be expressed as the difference between the squared magnetic field strength in the coil–tube gap, H_{gap}, and that inside the tube,

H_{pen}. In the case of a tubular workpiece with inner radius r_i and outer radius r_o (see Fig. 1.2), the magnetic pressure p can be calculated as:

$$p(r,t) = \int_{r_o}^{r_i} f(r,t)dr = \frac{\mu}{2}\left(H_{gap}^2(t) - H_{pen}^2(t)\right), \tag{1.5}$$

Using the relation $B = \mu H$, this dependence can be expressed equivalently in terms of magnetic flux density in the coil-tube gap B_{gap} and that inside the tube B_{pen}:

$$p(t) = \frac{1}{2\mu}\left(B_{gap}^2(t) - B_{pen}^2(t)\right), \tag{1.6}$$

Owing to the skin effect, the main contribution to the integral in Eq. (1.5) comes from the near-surface layer of workpiece facing the tool coil. For efficient EMPT operation the workpiece thickness should therefore be larger

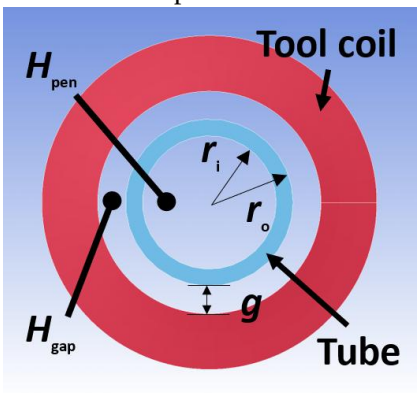


Fig. 1.2 Schematic of a coil–tube arrangement: H_{gap} is the magnetic field strength in the gap between the coil and the tube, and H_{pen} is the field strength penetrating into the tube, of inner radius r_i and outer radius r_o. The coil–tube gap is denoted g.

than the skin depth, so that the induced currents shield the transient magnetic field from the interior. The magnetic flux density on the coil-facing side then greatly exceeds that on the opposite side, and a net magnetic pressure acts on the workpiece.

If the field is effectively excluded from the interior of the workpiece, the penetrated magnetic flux density B_{pen} can be neglected compared with B_{gap}. In this case, Eq. (1.6) reduces to:

$$p(t) = \frac{B_{gap}^2(t)}{2\mu}, \tag{1.7}$$

According to the review by Psyk et al. [8], based on the experimental investigations and analytical calculations of Mühlbauer and von Finckenstein [24] for tube compression processes, the simplification $B_{pen} \approx 0$ is allowable when both of the following conditions are satisfied:

$$\frac{\delta}{r_i} < 0.2, \tag{1.8}$$

$$\frac{s}{\delta} \geq 2, \tag{1.9}$$

where s is the wall thickness of the workpiece (m). Psyk et al. [8] also reported that, according to the analytical estimations of Dietz et al. [10], this simplification can be considered acceptable when the wall thickness is at least 1.5 times larger than the skin depth:

$$\frac{s}{\delta} \geq 1.5, \tag{1.10}$$

The magnitude of the error introduced by this simplification can be estimated from the exponential decay given by Eq. (1.3). The current density at the far side of a wall of thickness s is $J(s) = J_0\, e^{-s/\delta}$. If $s = 1.5\delta$, the current density decreases to $e^{-1.5} \approx 0.223$ of its surface value. Since the magnetic field obeys the same diffusion equation as the current density, both are attenuated over the same characteristic length, so that $B_{pen}/B_{gap} \approx e^{-s/\delta}$. The magnetic pressure depends on the square of the magnetic flux density, and the relative contribution of the penetrated field to Eq. (1.6) is therefore approximately $(B_{pen}/B_{gap})^2 \approx e^{-2s/\delta}$. For the criterion of Eq. (1.10), $s = 1.5\delta$, this contribution is $(e^{(-1.5)})^2 \approx 0.05$, or about 5 %; for the more restrictive criterion of Eq. (1.9), $s = 2\delta$, it falls to $(e^{(-2)})^2 \approx 0.018$, or about 1.8 %.

An EMPT setup typically consists of a high-voltage power supply, a capacitor bank, a switching device, and a tool coil, which may optionally be equipped with a field shaper (concentrator). A general overview of the electrical scheme of an EMPT system is shown in Fig. 1.3.

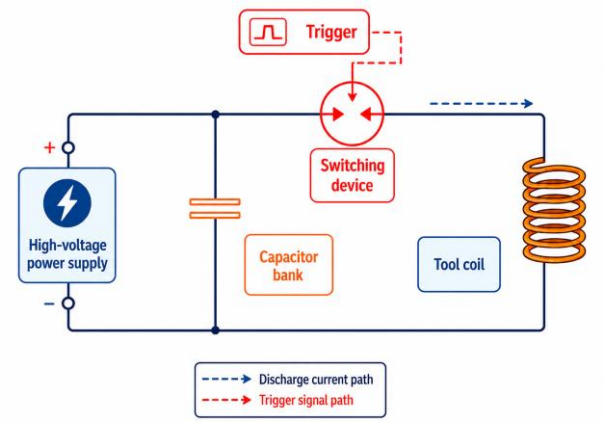


Fig. 1.3 General overview of the EMPT electrical circuit, comprising a high-voltage power supply, a capacitor bank, a triggered switching device with trigger and a tool coil.

The high-voltage power supply charges the capacitor bank to a predefined voltage before the discharge. The capacitor bank is the main energy storage element of the EMPT setup. The amount of stored electrical energy E (J) is determined by the capacitance C (F) of the capacitor bank and the charging voltage U (V) and can be expressed as [8]:

$$E = \frac{CU^2}{2}, \tag{1.11}$$

The switching device initiates the discharge by closing the high-current circuit after receiving a trigger signal. In an EMPT setup, this function can be performed by various high-power switches, such as triggered spark gaps [25, 26], ignitrons [27], semiconductor-based switches [28, 29]. These devices must withstand the charging voltage before triggering and conduct a large transient current during the discharge.

The tool coil is the key element of an EMPT setup and converts the discharge current into a transient magnetic field. Its geometry determines the spatial distribution of the magnetic field, the induced eddy currents in the workpiece, and the resulting magnetic pressure. Tool coil designs are considered in more detail in Section 1.2.

After triggering the switching device, the energy stored in the capacitor bank is rapidly released through the circuit, producing a high-amplitude current. The current I flowing through the tool coil exhibits a damped oscillatory waveform with an exponentially decaying amplitude [30, 31]:

$$I(t) = I_0 \mathrm{e}^{-\alpha t} \sin(\omega t), \tag{1.12}$$

where I_0 is the initial current amplitude (A), α is the damping coefficient (s^{-1}), ω is the angular frequency of the damped oscillation (rad/s), and t is the time (s). Both α and ω are determined by the equivalent resistance R, inductance L, and capacitance C of the discharge circuit [30, 32]:

$$\alpha = \frac{R}{2L}, \tag{1.13}$$

$$\omega = \sqrt{\frac{1}{LC} - \frac{R^2}{4L^2}}, \tag{1.14}$$

For an empty coil configuration, i.e., without a workpiece, the magnetic field generated by the tool coil is determined mainly by the discharge current and the coil geometry, so that an increase in the peak current leads to an increase in the peak magnetic field in the working gap. However, in a real EMPT setup, the tool coil does not operate as an isolated inductor, because the conductive workpiece is located inside it. In a simplified equivalent-circuit representation (Fig. 1.4), the tool coil is considered as the primary circuit, while the workpiece can be treated as a short-circuited secondary circuit of a

transformer. The transient magnetic field generated by the primary circuit induces eddy currents in the workpiece according to Faraday's law, and by Lenz's law these currents generate their own magnetic field, which opposes the variation of the primary magnetic field.

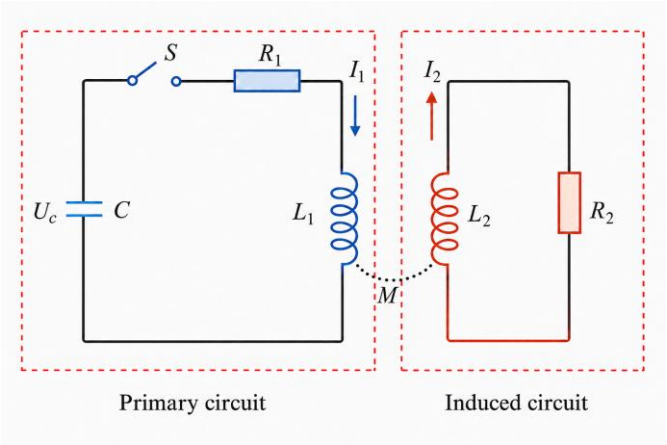


Fig. 1.4 Equivalent circuit of an EMPT setup. The primary circuit, of resistance R_1, inductance L_1 and current I_1, comprises the capacitor C charged to the voltage U_c, the switch S; the secondary circuit, of resistance R_2, inductance L_2 and current I_2, is formed by the workpiece. The two circuits are coupled through the mutual inductance M (Eq. 1.15).

For the equivalent circuit shown in Fig. 1.4, the governing equations can be obtained by applying Kirchhoff's voltage law to the primary and secondary circuits [33]:

$$\begin{cases} R_1 I_1(t) + L_1 \dfrac{dI_1(t)}{dt} + M \dfrac{dI_2(t)}{dt} = U_c(t) \\ R_2 I_2(t) + L_2 \dfrac{dI_2(t)}{dt} + M \dfrac{dI_1(t)}{dt} = 0 \end{cases}, \tag{1.15}$$

where R_1, L_1, and $I_1(t)$ are the equivalent resistance, inductance, and current of the primary circuit formed by the capacitor bank, transmission line, and tool coil, whereas R_2, L_2, and $I_2(t)$ are the equivalent resistance, inductance, and induced current of the secondary conductive circuit represented by the workpiece. Here, M is the mutual inductance between the two circuits and $U_c(t)$ is the capacitor voltage. The electrical response of the system is therefore determined not only by the nominal parameters of the primary circuit, but also by electromagnetic coupling with the conductive workpiece.

Since the workpiece behaves as a short-circuited secondary circuits, the induced currents in it introduce an additional effective resistance and an effective inductance into the discharge circuit. An increase in the effective

resistance increases the damping of the current oscillations, whereas a change in the effective inductance alters the oscillation period. The amplitude, frequency, and damping of the discharge current therefore depend not only on the nominal capacitance, resistance, and inductance of the primary circuit, but also on the geometry, conductivity, permeability, thickness, and position of the workpiece.

Weddeling et al. [32] proposed an analytical approach for estimating the acting magnetic pressure in magnetic pulse crimping (MPC). In their approach, the discharge system is first reduced to an equivalent RLC circuit, and the discharge current I is described by a damped sinusoidal function Eq. (1.12). The magnetic field strength H in the gap between the direct-acting compression coil and the tubular workpiece is then related to the discharge current through the number of coil windings n and the active coil length l_{coil}:

$$H(t) = \frac{n\, I(t)}{l_{coil}}, \tag{1.16}$$

Under the conditions of Eqs. (1.8)–(1.10), the penetrated magnetic field inside the tube can be neglected, and the magnetic pressure is expressed as a function of the squared magnetic field strength in the coil–workpiece gap (Eq. 1.5). By combining Eqs. (1.12), (1.16), and (1.5) when $H_{\mathrm{pen}} = 0$, an approximate time-dependent expression for the magnetic pressure p is obtained:

$$p(t) = \frac{\mu}{2} \frac{n^2}{l_{coil}^2} \frac{U^2}{(\omega L_{res})^2} e^{-2\alpha t} \sin^2(\omega t)\,, \tag{1.17}$$

where L_{res} is the resulting inductance of the simplified RLC circuit (H); U is the charging voltage (V).

Eq. (1.17) shows that the magnetic pressure is proportional to the square of the charging voltage U and of the number of coil turns n, and inversely proportional to the squares of the coil length l_{coil}, the resulting inductance L_{res}, and the angular frequency ω. The terms $e^{-2\alpha t}$ and $\sin^2(\omega t)$ arise because the pressure is proportional to H^2, and the magnetic field strength itself is proportional to the discharge current I.

In this model, the sign of the discharge current does not affect the direction of magnetic pressure, since the pressure depends on the square of the magnetic field strength. Both the positive and the negative half-cycles of the current waveform therefore contribute constructively to the magnetic pressure on the workpiece.

In the same work, Weddeling et al. [32] stated that, owing to the motion of the workpiece, the resulting inductance L_{res} and resistance are time-dependent. Including this dependence would not allow the analytical solution of the RLC

circuit equation; therefore, in their analytical model the workpiece motion is neglected, and the resulting inductance and resistance are assumed constant.

During forming or welding, the workpiece moves and deforms under the action of electromagnetic forces. The gap between the tool and the workpiece, the mutual inductance M between them (Eq. 1.15), and the distribution of the eddy currents therefore all change with time. Since these quantities determine the effective impedance of the discharge circuit, the current waveform may in principle carry information about the evolution of the electromagnetic coupling during deformation.

This effect was studied experimentally by Sofi et al. [34], who investigated the influence of the tubular workpieces, the field shaper, and field-shaper material on the current waveform of a MPW setup. At the same charging voltage, changing the field-shaper material altered the duration of the discharge current pulse from approximately 80 μs to approximately 170 μs, and the presence of the tubular workpiece increased the peak current.

Current measurements in EMPT are typically carried out non-invasively using Rogowski coils, which are well suited for recording large transient currents (about 100 kA) without direct electrical contact with the conductor [17]. The current waveform is, however, an integral response of the entire discharge circuit, and it therefore lacks sensitivity to local changes in the working gap. Stankevic et al. [18] showed that, when a field shaper is used, deformation of the flyer changes the coil current only slightly, while the magnetic field in the gap changes substantially.

Dond et al. [35] investigated the effect of the coil–workpiece gap on the discharge circuit parameters and on the deformation of the workpiece during electromagnetic tube expansion. Their model treats the tubular workpiece as a short-circuited single-turn secondary circuit coupled to the *N*-turn tool coil. The mutual inductance *M* is expressed through the coupling coefficient *K*:

$$M = K\sqrt{L_{coil}L_{wp}}, \tag{1.18}$$

where L_{coil} and L_{wp} are the self-inductances of the tool coil alone and the workpiece, respectively.

The coupling coefficient *K* was determined in two independent ways. Experimentally it was obtained from the inductance of the coil measured with and without the tube in place. Numerically it was obtained from a finite-element model as the ratio of the peak eddy current in the tube to the ampere-turns of the coil. Both determinations gave a coupling coefficient that decreases with the coil–workpiece gap g (see Fig. 1.2), and over a gap range of 3 to 12 mm the dependence was fitted by an exponential decay:

$$K(h) = A_0 e^{-B_0 h}, \tag{1.19}$$

where A_0 and B_0 are fitting constants. Increasing the gap raised the combined coil–workpiece inductance and lowered the combined resistance, and the measured peak coil current decreased accordingly.

Dond et al. further distinguished two situations. In the first, the tube retains its initial cylindrical shape and the gap is uniform along its length. In the second, the tube undergoes non-uniform deformation, so the gap varies along the tube and changes throughout the pulse. Taking h at the point of largest deformation, their simulations gave a higher coupling coefficient for the deforming tube than for the undeformed one at the same value of *h*. They concluded that the relation obtained for the undeformed geometry cannot be used to determine how the discharge circuit parameters vary during forming. In MPW the geometry is more complex still, since the flyer deforms non-uniformly and the collision with the stationary parent workpiece is oblique, with the collision point propagating along the joint, which makes an analytical description of the evolving coupling considerably more difficult.

According to Lueg-Althoff et al. [36], the radial acceleration of the flyer tube is governed by the difference between magnetic pressure p and the resistance of the material to plastic deformation:

$$\rho s \frac{d^2u(r,t)}{dt^2} = p(t) - p_d(t), \tag{1.20}$$

where ρ is the material density (kg/m^3), s is the wall thickness (m), u is the radial displacement of the flyer (m) and p_d represents the pressure necessary for plasticization (Pa). For a thin-walled tube, the authors used the estimate of p_d:

$$p_d = \sigma_c \frac{s}{r_{tube}}, \tag{1.21}$$

where σ_c is yield stress of the material (Pa), r_{tube} the tube radius (m). For an arbitrary wall thickness with outer radius, r_{out} (m) and inner radius, r_{in} (m):

$$p_d = \frac{2}{\sqrt{3}} k_f \ln\left(\frac{r_{out}}{r_{in}}\right), \tag{1.22}$$

where the product $(2/\sqrt{3})k_f$ represents the effective plastic resistance stress of the tube wall according to the von Mises criterion.

As the tube is compressed, its radius decreases, its wall thickness increases and the material hardens, and each of these effects increase p_d during the process. In the analytical model, however, p_d is taken as constant.

Rearranging Eq. (1.20), gives the radial acceleration:

$$\frac{d^2u(r,t)}{dt^2} = \frac{p(t) - p_d}{\rho s}, \tag{1.23}$$

The tube therefore begins to move only once magnetic pressure exceeds the p_d. If $p(t) \leq p_d$, the model predicts no plastic deformation and no radial motion. The velocity is obtained by integrating the acceleration over time:

$$v(t) = \frac{du(r,t)}{dt} = \int \frac{p(t) - p_d}{\rho s}\, dt\,, \tag{1.24}$$

Following the approach originally proposed by Dietz et al. [37] and adapted by Lueg-Althoff et al. [36], the magnetic pressure $p(t)$ is approximated by a triangular, piecewise linear function representing to the first half-wave of the discharge current. The triangle is constructed from the measured current waveform, with its apex at the time of maximum pressure and its base ending at the first zero crossing of the current. The impact velocity is taken from the calculated velocity curve at the moment when the radial displacement of the flyer reaches the initial standoff distance.

Lueg-Althoff et al. [36] compared the calculated velocity curves with velocities measured by Photonic Doppler Velocimetry (PDV). Deviations between calculation and measurement were observed, but the model reproduced the general trend of the flyer velocity and showed that the impact velocity can be estimated from the measured discharge current. According to the model, the plastic deformation and the acceleration of the flyer occur within the first current half-wave: the acceleration grows while the magnetic pressure rises, and after the current maximum the pressure decreases but the tube continues to accelerate as long as the pressure remains above pd. The maximum flyer velocity is therefore reached after a delay with respect to the current maximum.

Electromagnetic pulse technology represents is a complex family of processes from both analytical and practical viewpoints. The electromagnetic–mechanical interaction involves many coupled parameters, including coil geometry and impedance, the presence and material of field shapers, workpiece geometry, electrical conductivity, magnetic permeability, thickness, initial gap between the coil and workpiece, as well as charging voltage, capacitance, and switching characteristics of the circuit. Together, these parameters determine the discharge current waveform, the spatial distribution of the magnetic field, the induced eddy currents, the resulting magnetic pressure, and the deformation response of the workpiece.

At the same time, different EMPT operations, such as forming, crimping, cutting, welding, and cladding, require different coil designs, field shaper geometries, and tooling configurations. This leads to a wide variety of working conditions and makes direct comparison between different studies difficult.

Because of this complexity, and because the discharge circuit, the electromagnetic field and the mechanical response are coupled to one another, analytical treatments are generally restricted to simplified one-dimensional or quasi-static representations. Finite-element modelling is therefore widely used for the analysis and design of EMPT operations.

The magnetic field in the gap between the tool and the workpiece determines the magnetic pressure and therefore the acceleration of the workpiece during the current pulse. This local quantity is difficult to access experimentally. The discharge current is recorded routinely, but it is the response of the whole discharge circuit and does not give the field in the gap. Time-resolved measurement of the magnetic field in the gap is reported in comparatively few studies.

The following sections of the literature review address four main aspects in more detail: first, the design and geometry of tool coils and field shapers; second, the principles and specific features of EMPT operations, including forming, crimping, welding, cladding, and cutting; third, experimental diagnostics and sensing techniques; and fourth, state-of-the-art FEM-based modelling approaches, including implementations in COMSOL Multiphysics and LS-DYNA.

1.2 Tool Coils in Electromagnetic Pulse Technology

Different tool coil configurations are used depending on the geometry of the workpiece and the required direction of electromagnetic pressure. For tubular workpieces, cylindrical or solenoidal coils are commonly used. In tube compression, crimping, and welding, the coil surrounds the outer workpiece (Fig. 1.5 (a)) and generates magnetic pressure directed inward the flyer tube. In contrast, internal expansion coils are placed inside tubular workpieces (Fig. 1.5 (b)) and are used when the workpiece has to be expanded outward.

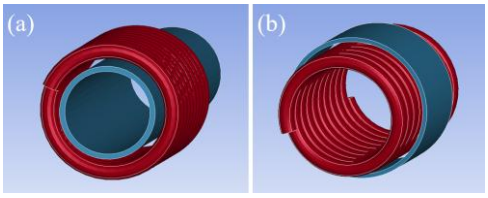


Fig. 1.5 (a) Tool coil configurations for tubular workpieces: (a) compression coil, with the workpiece inside the coil; (b) expansion coil, with the workpiece outside the coil.

Flat coils or single-turn loop coils with various shapes (Fig. 1.6) are applied when a localised pressure distribution is required [38]. Flat spiral coils, often referred to as pancake coils [39, 40, 41], generate magnetic pressure over a planar region (Fig. 1.7).

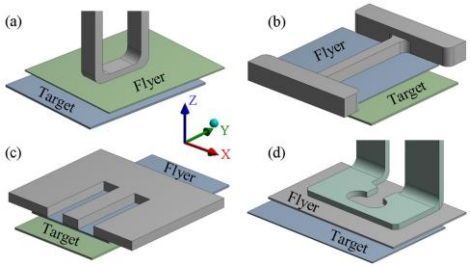


Fig. 1.6 Flat coils for MPW of sheets, with (a) rectangular, (b) H- or I-shaped, (c) E-shaped and (d) O-shaped working conductors. Adopted from [38].

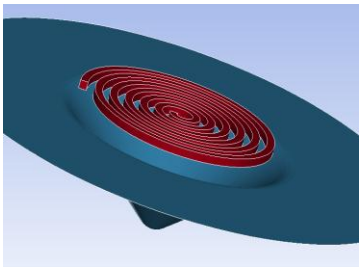


Fig. 1.7 Schematic of a pancake coil and the sheet workpiece after deformation.

The number of turns determines the inductance of the coil and the field it produces. Single-turn coils have a low inductance and can carry high transient currents. Multi-turn coils produce a higher magnetic field per unit current, but they raise the circuit inductance and therefore reduce the peak current, and the electromagnetic forces acting between adjacent turns increase. Multi-turn coils therefore require mechanical reinforcement and electrical insulation between the turns.

The electromagnetic forces generated during EMPT acts mechanically not only on the workpiece but also on the tool coil itself. The Bitter coil (Fig. 1.8), originally developed for high-field magnets, is one design used in EMPT for its mechanical strength [42]. Zaitov and Kolchuzhin [43] developed an analytical method and finite-element model of a Bitter coil and verified them experimentally by the impedance and magnetic-field measurements.

A Bitter coil is assembled from a stack of metallic disks, typically made of copper or aluminium, which are cut along the radius. Each disk operates as a single turn in the coil. These disks are insulated from each other by dielectric spacers. The entire assembly is securely tightened with bolts to withstand significant mechanical stress which created by electromagnetic forces during the capacitor discharge.

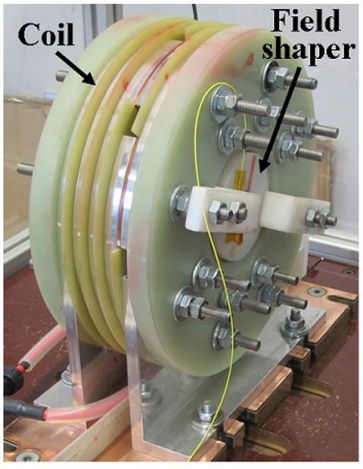


Fig. 1.8 Bitter coil, the arrow indicates the field shaper inserted in its bore. Adopted from [42].

In many practical EMPT setups, the tool coil is combined with a field shaper (FS) (Fig. 1.9 (a)). The terms field shaper and field concentrator are used interchangeably in the literature [44, 45]. The field shaper is a cylindrical part with a radial slit, in which

the inner surface features a stepped, tapered or concave profile [46] so that the inner surface area is much smaller than the outer one (see Fig. 1.9(a)). Field shapers are made from a highly conductive metal alloys and are used with both pancake coils [47] and cylindrical coils [48].

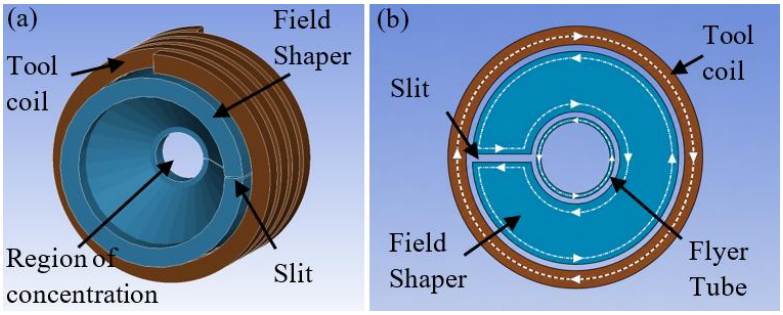


Fig. 1.9 (a) Cylindrical tool coil with the field shaper and the cylindrical region of magnetic field concentration inside its bore; (b) side view of the tool coil with the field shaper and the flyer tube. The white dotted arrows indicate the direction of the coil current and of the currents induced on the surfaces of the field shaper and in the flyer tube.

When a pulsed discharge current flows through the tool coil (Fig. 1.9 (b), white arrows), a transient magnetic field is generated around the coil. This field induces eddy currents on the outer surface of the FS which, by Lenz's law, flow in the direction opposite to the current in the tool coil. The axial slit redirects this current from the outer surface to the inner surface, that is, to the concentration area, where it flows in the same direction as the current in the tool coil. Since the inner concentration area is much smaller than the outer surface, the current density there is considerably higher, and the magnetic field is concentrated in the narrow gap between the field shaper and the flyer tube. This concentrated magnetic field induces an eddy current in the outer surface of the flyer tube and the interaction between this current and the magnetic field produces Lorentz forces that act radially on the tube and initiate plastic deformation once the resulting stresses exceed the flow stress of the material [8].

The field shaper therefore redirects the induced current onto a smaller area and concentrates the magnetic field in the working gap, which increases the magnetic pressure acting on the flyer tube compared with a directly acting coil. In addition, a FS can reduce the required discharge energy, improve the flexibility of the setup for different tubular workpiece diameters, and mechanically reinforce and protect the tool coil from the high magnetic pressure generated in the concentration area [8].

The slit, however, makes the magnetic field azimuthally non-uniform, so that the magnetic pressure varies around the circumference of the flyer tube.

Zaytsev et al. [46] showed that the largest reductions in magnetic field occur at angular positions corresponding to the slit. Since magnetic pressure is proportional to B^2 (see Eq. 1.7), even a relatively small variation in magnetic flux density can produce a more pronounced difference in magnetic pressure. Such non-uniformity leads to non-uniform compression of the flyer tube and can affect the quality of the welded joint along the circumference.

1.3 Application of Electromagnetic Pulse Technology

Electromagnetic pulse technology comprises several operation modes: magnetic pulse forming (MPF), magnetic pulse welding (MPW), magnetic pulse crimping (MPC), magnetic pulse cladding, and magnetic pulse cutting. They differ in their technological objective and in the required coil–workpiece configuration.

1.3.1 Magnetic Pulse Forming

In MPF, electromagnetic forces are used to deform the workpiece plastically into the desired shape. Depending on the coil–workpiece arrangement, MPF is used for the compression or expansion of tubular components and hollow profiles, as well as for forming, embossing, and local shaping of sheet-metal parts. The forming result is governed by the discharge current waveform, the coil geometry, the conductivity and thickness of workpiece, the initial gap, the die or support geometry, and the spatial distribution of the magnetic pressure [8].

The advantages of MPF follow from its contact-free and high-speed character. Since the workpiece is loaded by magnetic pressure rather than by a rigid punch, friction and local contact-pressure concentrations are reduced, and lubrication and removal of tool marks are often not required. The high deformation velocity also changes the mechanical response of the workpiece: very high strain rates, together with inertia effects, can improve formability, reduce springback, and produce a more favourable strain distribution compared with contact-pressure forming [49, 50].

1.3.2 Magnetic Pulse Welding and Cladding

Magnetic pulse welding (MPW) is an advanced, eco-friendly [14], solid-state joining technology in which magnetic forces accelerate one workpiece, the flyer, towards another, the parent, producing a high-velocity collision between them. This collision results in a metallurgical bond. The bonding

mechanism is attributed either to solid-state bonding without melting or to localised melting followed by rapid solidification [51].

A schematic layout of the MPW process is shown in Fig. 1.10. The capacitor bank is discharged through the tool coil, producing a short high-amplitude current pulse that generates a transient magnetic field in the working region of the coil. When the magnetic field penetrates the conductive flyer workpiece, eddy currents are induced near its surface. The interaction between the induced current density and the magnetic field produces an electromagnetic force density (see Eq. 1.2). In tube-compression MPW, this force is directed toward the parent workpiece and accelerates the flyer tube inward. As a result, the flyer tube undergoes high-speed deformation and impacts the parent tube, leading to the formation of a metallurgical bond at the collision interface.

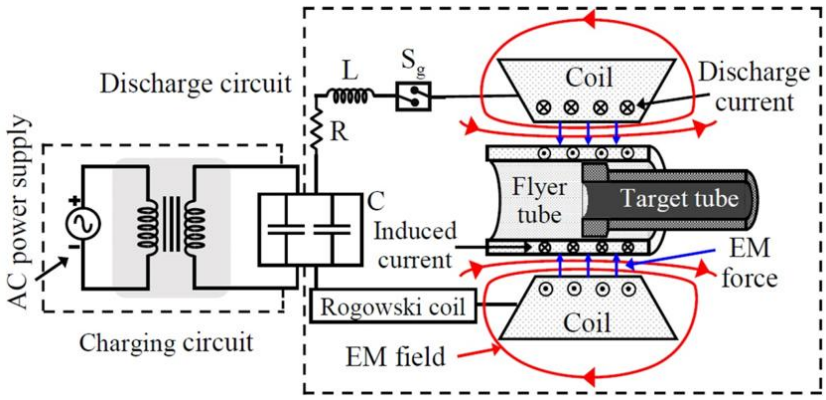


Fig. 1.10 Schematic layout of a MPW setup for joining tubes, showing the charging circuit and the discharge circuit. C is the capacitor bank, R and L the resistance and inductance of the discharge circuit, and S_g the spark gap; the discharge current is measured with a Rogowski coil. The red arrows indicate the magnetic field, the blue arrows the electromagnetic force acting on the flyer tube, and the symbols ⊗ and ⊙ the direction of the induced currents in the coil and in the flyer tube. The stationary tube, labelled target tube in the figure, is referred to as the parent workpiece throughout this thesis. Adopted from [42]

Similar to explosion welding (EXW) [52], MPW belongs to the group of high-velocity collision welding processes, in which bonding is achieved by the impact of the materials to be joined, including dissimilar material combinations. Compared with EXW, MPW has lower safety requirements and is a cleaner process, since no explosive substances or residues are involved [17].

In conventional fusion welding of dissimilar material, differences in melting temperature, thermal expansion coefficient, thermal conductivity, and

metallurgical compatibility can promote the formation of brittle intermetallic compounds, residual stresses and heat-affected zones [53, 54]. Since MPW is a solid-state impact welding process with very short interaction time and no external heat source, these thermally induced problems are reduced or avoided [55].

A characteristic feature of many high-quality MPW joints is a wavy interface between the joined metals. As shown schematically in Fig. 1.11, the flyer approaches the parent material with the impact velocity v_{imp}, while the collision point propagates along the interface with the collision velocity v_c. The interaction occurs at the collision angle β, which is formed between the flyer and the parent surface at the moving collision front.

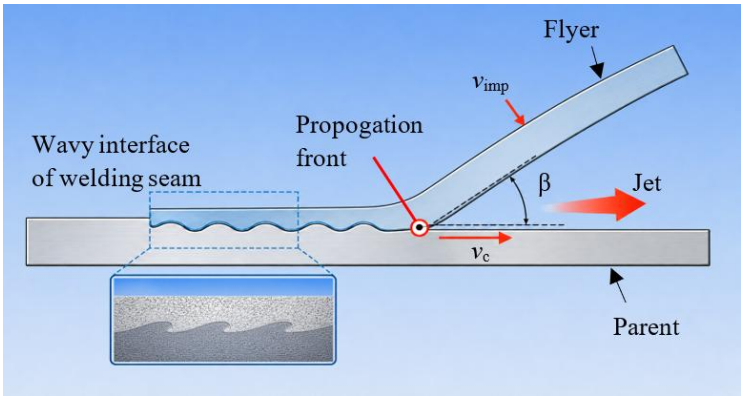


Fig. 1.11 Flyer impact in MPW. The flyer meets the parent at an impact velocity v_{imp} and collision angle β, while the collision point, labelled propagation front in the figure, travels along the interface at the velocity v_c. The red arrow shows the jet, expelled ahead of the collision point. The enlarged region shows the wavy interface characteristic of a sound impact weld.

Under suitable collision conditions a jet is expelled ahead of the collision point (see Fig. 1.11), which removes surface oxides and contaminants and brings clean metal surfaces into contact. The subsequent plastic deformation and localised material flow produce the metallurgical bond and often a wavy interface. The waves promote mechanical interlocking between the metals and are commonly regarded an indicator of successful bonding [56].

In a simplified geometric representation of oblique impact welding, the collision velocity v_c (m/s), that is, the velocity at which the welding front propagates, is related to the flyer impact velocity v_{imp} (m/s), and the collision angle β, as [57]:

$$v_c = \frac{v_{imp}}{2\sin(\beta/2)}, \tag{1.25}$$

This relation was derived for parallel cladding, in which the two plates are initially parallel and the collision point moves along both of them at the same velocity. In magnetic pulse welding the collision angle is produced by the deformation of the flyer itself, so the relation is applied as an approximation.

The weldability window describes the range of collision conditions under which an impact-welded joint can be formed [56]. As shown in Fig. 1.12, the collision velocity is plotted along the horizontal axis, while the collision angle is plotted along the vertical axis. A sound weld is obtained only within a limited region of this plane. If the collision velocity or angle is too low, the impact energy is insufficient and no weld is formed. If they are too high, excessive interfacial melting occurs and the bond is degraded. The weldability window is bounded not only by the limits of sufficient impact pressure and acceptable deformation, but also by the conditions required for stable jet formation [58].

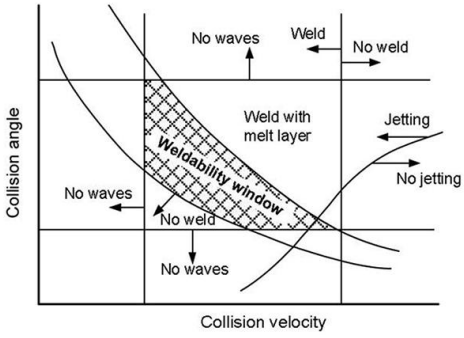


Fig. 1.6 Weldability window for impact welding. A sound weld is obtained only within the enclosed region. Adopted from [58]

Depending on the material combination and local collision conditions, the welding interface can remain nearly straight, develop regular waves, form vortices, or contain local intermediate layers and melt pockets [59]. These features are affected by the impact velocity, the collision angle, the initial standoff distance, and material properties such as density, yield strength, thermal conductivity. For example, Raoelison et al. [60] showed for Al/Al welding that varying the initial standoff distance and charging voltages changes the size of the interfacial waves. A small initial standoff distance produces a bonded interface with small waves sizes. As the standoff distance increases, the flyer accelerates over a longer distance and reaches a higher impact velocity, which produces more intensive plastic flow at the interface and increases both wave amplitude and wavelength. An excessively large standoff distance can reduce weld integrity, since the resulting higher impact

velocity may produce excessive pressure and interfacial shear, leading to material expulsion, crack initiation, and brittle behaviour of the welded joint.

Magnetic pulse cladding is based on the same high-velocity oblique collision as MPW, but produces a continuous bonded layer over the surface of a substrate rather than a localised joint [61]. The collision conditions and the bonding mechanisms are therefore those described above.

1.3.3 Magnetic Pulse Crimping

Magnetic pulse crimping (MPC) is related to magnetic pulse welding (MPW), since both processes are based on high-rate deformation of a conductive workpiece. Whereas MPW aims to create a metallurgical bond, MPC relies on plastic deformation to produce mechanical compression between the components. Compared with mechanical crimping, MPC is a contactless process that allows high-speed joining of conductive tubular parts and terminals [12], which makes it suitable for applications requiring strong mechanical fixation and low tool-induced contamination [62].

1.3.4 Magnetic Pulse Cutting

In electromagnetic pulse cutting, the magnetic pressure produces localised high-rate deformation of the workpiece and drives it toward a cutting edge or die, resulting in shearing along a predefined path. Zimniak [63] studied magnetic pulse cutting of metal sheets and showed that conventional cutting equipment can be adapted to this technology, reducing the mechanical work required from the punch and press. Successful cutting requires not only sufficient magnetic pressure, but also adequate localization of the electromagnetic loading and an appropriate design of the cutting edge and support tooling. Psyk et al. [8] noted that cutting operations can be combined with MPF, MPW technology.

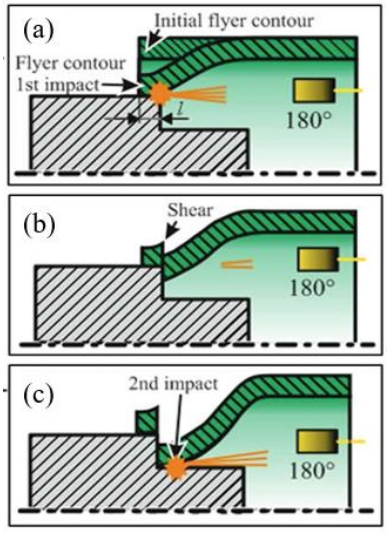


Fig. 1.7 Combined joining and shearing configuration: (a) flyer contour at the first impact; (b) shearing of the flyer at the edge of the parent; (c) flyer contour at the second impact. Adopted from [64]

Bellmann et al. [64], for example, used a combined joining and shearing

configuration to investigate the development of the collision-induced flash during MPW (Fig. 1.13). A stepped parent-part geometry limited the available collision length, and the flyer was sheared at the edge of the parent part after propagating over a predefined distance.

1.4 Experimental Diagnostics and Monitoring of EMPT parameters

Experimental diagnostics and in-situ monitoring are required in EMPT, because the quality of formed, crimped, or welded components to be assessed indirectly through the process parameters recorded during the pulse. From measurements of the discharge current, the magnetic flux density, the workpiece velocity and displacement, and the collision conditions, the transient dynamics of the process can be evaluated and related to the integrity of the joint or to the formed geometry.

1.4.1 Discharge Current and Voltage Measurements

The discharge current and the capacitor charging voltage are the most basic measured quantities in EMPT, since the pulsed current in the tool coil is the source of the transient magnetic field, and hence of the induced eddy currents, the magnetic pressure, and the deformation of the workpiece. In typical EMPT systems, the discharge current ranges from several tens to a few hundred kiloamperes [11] and has a damped oscillatory waveform with a characteristic frequency of several tens of kilohertz. As discussed above, this current is described by the discharge equation of the RLC circuit, Eq. (1.12), in which the capacitance, resistance, and inductance of the system determine the peak current, the pulse duration, the damping, and the oscillation frequency.

The current waveform is usually measured non-invasively with a Rogowski coil (Fig. 1.14) [38, 42], which produces a voltage proportional to the time derivative of the current:

$$U_R(t) = M_R \frac{dI(t)}{dt}, \tag{1.26}$$

where $u_R(t)$ is the output voltage of Rogowski coil (V); M_R is mutual inductance between the coil and the current-carrying conductor (H); and $I(t)$ is the discharge current (A). The output is integrated, either by an analogue integrator or numerically, to recover $I(t)$.

Rogowski coils are well suited to EMPT because they require no electrical contact with the current-carrying conductor and, having no ferromagnetic core, do not saturate at high currents. The recorded waveform yields the peak current, the rise time, the period and the damping coefficient of the discharge.

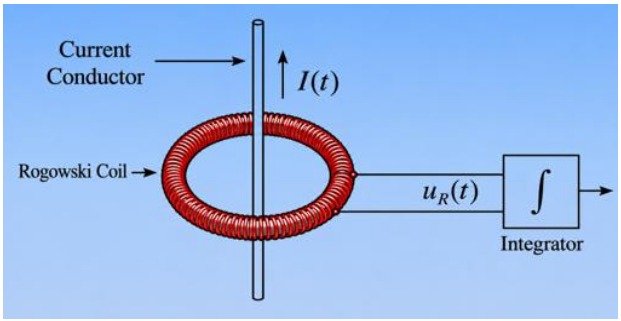


Fig. 1.8 Measurement of the discharge current with a Rogowski coil. The coil encircles the conductor carrying the current $I(t)$ and produces the output voltage $U_R(t)$; the current is recovered by integrating this voltage.

The capacitor bank voltage is measured before the discharge in order to calculate the stored energy of the pulse generator according to Eq. (1.11). The discharge current, the charging voltage, and the stored energy are used for process control, for assessing repeatability and as input for numerical modelling.

1.4.2 Flyer Velocity and Displacement Measurement

The flyer velocity and displacement of the flyer are important quantities in EMPT, and in MPW in particular. The impact velocity and the instant of impact are obtained from them, and these determine whether the collision conditions lie within the weldability window.

1.4.2.1 Optical sensors

Optical techniques are often used to measure the flyer motion, since they are insensitive to the electromagnetic fields of the process. One of them is the shadowing method, applied by Bellmann et al. [17] to tube compression and MPW and by Veenaas et al. [65] to laser shock stretch drawing. A collimated laser beam is guided through the gap between the workpieces (see Fig. 1.15 (a)); as the flyer deforms and moves, it progressively blocks the beam, and the change in the transmitted light is recorded and converted into a voltage signal proportional to the unblocked fraction of the beam. The method gives an estimate of the average deformation velocity of the flyer, but requires optical access to it.

Photonic Doppler Velocimetry (PDV) is an optical technique for non-contact, time-resolved measurement of the velocity of moving surfaces in high-speed dynamic processes (Fig. 1.15 (b)) [17, 66]. It is based on the

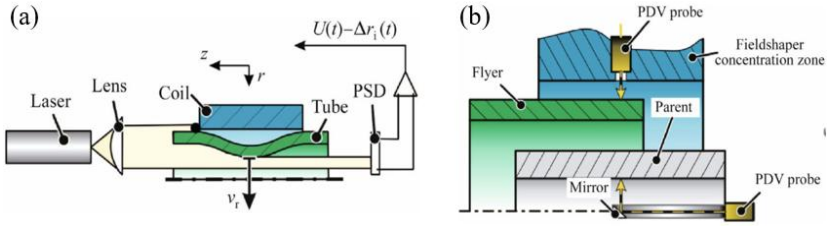


Fig. 1.9 (a) Principle of the measurement of tube compression velocity by optical shadowing: the laser beam is shaped by a lens and the shadow of the tube edge falls on a position-sensitive detector (PSD), whose output voltage $U(t)$ gives the radial displacement $\Delta r_i(t)$ of the tube surface; (b) arrangement for the simultaneous measurement of the flyer and parent motion with two PDV probes, one directed at the parent through a mirror placed inside it and the other viewing the flyer through a borehole in the field shaper. Adopted from [17].

Doppler shift of laser light reflected from the moving surface. The reflected signal interferes with a reference signal, and the resulting beat frequency f_b (Hz), gives the surface velocity v (m/s):

$$v(t) = \frac{\lambda_0}{2} f_b(t), \tag{1.27}$$

$$f_b = f_d - f_0, \tag{1.28}$$

$$\lambda_0 = \frac{c}{f_0}, \tag{1.29}$$

where λ_0 is the laser wavelength (m), f_d is the frequency of reflected light (Hz), f_0 is the frequency of the incident laser light (Hz), c is the speed of light (m/s). Eq. (1.27) holds when the laser beam is directed along the normal to the moving surface and the motion occurs along that direction.

PDV has become one of the most widely used methods for measuring flyer velocity and displacement during high-speed deformation and impact in EMPT. Jäger and Tekkaya [67] used a collimator-style PDV probe for online measurement of the radial displacement of the workpiece in electromagnetic forming. Lueg-Althoff et al. [36], used PDV to validate an analytical model for the impact velocity of tubular workpieces during electromagnetic compression: the radial motion of the flyer tube was described by the balance between the magnetic pressure and the plasticization pressure of the workpiece (see Eq. 1.20), the pressure function was adapted to the measured current waveform with the influence of the field shaper included and the calculated the flyer velocity was compared with the PDV record.

Johnson et al. [68] accelerated a two-layer sheet consisting of a copper driver and a titanium workpiece at a discharge energy of 6.4 kJ over a standoff distance of 2 mm, and measured nearly uniform sheet velocities of up to approximately 300 m/s; the same method was applied to magnetic pulse

flange impact welding, and gave velocity data during bending and distortion of the flyer.

Since the measurement is optical and can be implemented with fibre-optic probes, PDV is less sensitive to electromagnetic interference than electrical sensors placed near the tool coil [17]. The method requires optical access to the moving surface and accurate alignment of the probes, which is difficult in narrow gaps without modifying the EMPT setup.

High-speed imaging is also used for flyer displacement and velocity measurements where optical access to the deformation zone is available. Watanabe and Kumai [69] observed the MPW process in-situ with a high-speed video camera and studied the deformation and collision behaviour of aluminium plates, obtaining an impact velocity of approximately 250 m/s at a standoff distance of 1.0 mm.

1.4.2.2 Magnetic proximity sensors

Magnetic proximity sensors are another class of non-contact sensors used for measuring the position, displacement, and velocity of metallic targets [70]. Their operation is based on detecting changes in the magnetic field or in the electromagnetic response of a target placed near the sensing element.

The excitation field is produced either by a permanent magnet or by an AC-excited inductive coil. In the first case, the sensor typically consists of a permanent magnet and a magnetic field sensing element, which may be an inductive coil, a Hall-effect sensor, or a magnetoresistive sensor based on anisotropic magnetoresistance (AMR), giant magnetoresistance (GMR), or tunnel magnetoresistance (TMR) [71, 72, 73, 74, 75]. The permanent magnet provides a bias field, and the sensing element detects the changes in the field distribution caused by the presence or the motion of the target.

For ferromagnetic targets, the response arises from the magnetisation of the target and the resulting redistribution of the magnetic field. For non-ferromagnetic conductive targets in a static magnetic field, the response arises from the motion of the target: motion induces eddy currents, which generate a secondary magnetic field For ferromagnetic targets, the response arises from the magnetisation of the target and the resulting redistribution of the magnetic field. For non-ferromagnetic conductive targets in a static magnetic field, the response arises from the motion of the target: motion induces eddy currents, which generate a secondary magnetic field, and the sensing element measures the superposition of the field of the permanent magnet and this secondary field.

In sensors based on an AC-excited inductive coil, the field is generated by an alternating current in the coil. A conductive target entering this field carries induced eddy currents, whose secondary magnetic field interacts with the excitation coil and changes its electrical parameters, such as impedance, inductance or output voltage. The distance to the target and its displacement or velocity are determined from these changes [76]. In a related configuration, a magnetic field sensor is placed between the AC excitation coil and the target, so that the sensor detects the perturbation of the field produced by the induced eddy currents directly; this arrangement was reported to give more accurate measurements of target position and motion than conventional inductive proximity sensors [77].

The sensors described above have limitations that matter for the conditions of EMPT. AMR and GMR sensors have a limited linear range and saturate at magnetic flux densities far below those reached in the gap between the tool and the workpiece during a discharge. Hall-effect sensors measure one component of the magnetic flux density vector and therefore require the sensor plane to be aligned with respect to the field, which is difficult in a gap of less than a millimetre. Magnetoresistive sensors are likewise sensitive to the orientation of the field with respect to their sensing axis, which complicates alignment and installation.

The discovery of the colossal magnetoresistance (CMR) phenomenon in manganite films [78] led to the development of CMR B-scalar sensors [21]. Sensors made from nanostructured polycrystalline manganite films [79], exhibit very low magnetic anisotropy and respond to the magnitude of the magnetic flux density independently of the field orientation relative to the sensor plane. This response makes them applicable both to the measurement of high transient magnetic fields and to proximity sensing, where the orientation of the field is not known in advance.

1.4.3 Impact Time and Collision Velocity Detection

In EMPT, and in MPW in particular, the impact time and the collision front velocity describe the dynamic interaction between the flyer and the parent workpiece. The impact time t_{imp} is the instant at which the flyer reaches the parent surface and the collision velocity v_{c} is the velocity at which the collision point propagates along the interface after the first contact. Both are determined experimentally by several approaches, including PDV, high-speed imaging, contact pins/rings, or impact-flash measurements [17].

Bellmann et al. [64] used a high-velocity impact flash which naturally generated during MPW. In the experimental setup, several optical collimators

were positioned around the welding region to detect the time-dependent light emission during the collision. Flash signals were recorded at different circumferential positions. The flash appearance time was used as an optical indicator of the local impact time. In preliminary tests the flash appearance time agreed with the collision time determined by PDV, the mean values differed by approximately 0.5 μs, which the authors attributed to the delay of flash formation and to the optoelectrical conversion. Recording the flash at several circumferential positions allowed not only the impact time, but also the velocity of the collision front v_c to be evaluated.

A contact-based approach was described by Krutikov [80]. The parent workpiece was replaced by a contact sensor consisting of electrically insulated contact rings placed inside the accelerated tube (Fig. 1.16). During electromagnetic compression, the tube touched the rings in sequence at different axial positions, and each ring acted as a switch in an individual RC circuit. When contact occurred, the corresponding capacitor discharged and produced a voltage pulse recorded by an oscilloscope. The sequential closing of the contact circuits allowed the impact time at each axial position to be determined. The collision front velocity was then calculated as $v_c = h/\Delta t$, where v_c is the collision front velocity, h is the axial distance between neighbouring rings; and Δt is the time interval between the closure of neighbouring contacts.

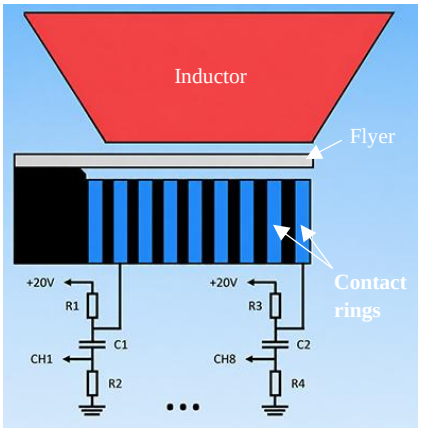


Fig. 1.10 Contact-based method of impact time measurement used in [80]. The parent workpiece is replaced by a sensor carrying electrically insulated contact rings at different axial positions inside the tube; during compression the tube reaches the rings in sequence, each ring closing an individual RC circuit.

Both approaches give the impact time directly, but neither is applicable to an actual welding operation in a closed configuration: the flash method requires optical access to the collision region, and the contact method requires the parent workpiece to be replaced by the sensor, so that no joint is produced.

1.4.4 Magnetic Field Measurement

Direct measurement of the transient magnetic field is more challenging, but it is important because the current pulse in the tool coil generates the magnetic field that produces the magnetic pressure acting on the flyer (see

Eq. 1.5). Magnetic field measurements therefore provide a more direct insight into the transfer of energy from the discharge circuit to the flyer.

Broeckhove et al. [19] used a single-turn inductive probe to measure the transient magnetic field during MPW (Fig. 1.17). The probe consisted of a cylindrical PVC tube with a single turn of copper wire wound around it, and the magnetic field was obtained by integrating the measured voltage. The probe and its wiring have to be carefully shielded to minimize electromagnetic interference and the parasitic electromotive force (EMF) induced in the measurement circuit.



Fig. 1.11 Single-turn inductive magnetic field probe. Adopted from [19].

Merte et al. [20] used two fibre-optic point probes for time-resolved measurement of magnetic field distribution in gap between the coil and the workpiece in electromagnetic forming. Both probes were based on the magneto-optic Faraday effect, in which the magnetic field rotates the polarisation plane of light propagating through the sensing element; in one probe the element was a flint glass fibre, in the other a SiO_2 crystal (Fig. 1.18).

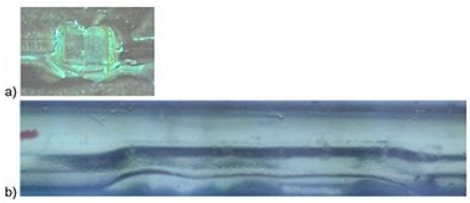


Fig. 1.18 Miniature fibre-optic magnetic field probes based on the Faraday effect: (a) multimode fibre with a glued SiO_2 crystal with polarising surfaces; (b) polarising fibre with a spliced section of flint-glass fibre. Adopted from [20].

The probes were not calibrated for the flux densities reached in the experiment, so the results were reported as sensor output voltage rather than as magnetic flux density. The authors also observed that consecutive measurements produced different signal shapes, which they attributed to the sensitivity of the field distribution to small changes in the setup and to mechanical coupling between the forming system and the optical probe. The work demonstrated that miniature fibre-optic probes can resolve the field in a narrow forming gap in time, but also that the approach requires further work on calibration, mechanical mounting and vibration isolation.

Single-turn inductive probes provide high temporal resolution but require signal to be integrated, whereas Hall sensors give the magnetic flux density directly. Bellmann et al. [17] reported the use of Hall sensors for magnetic

field measurements in MPW and highlighted the necessity of applying specialised methods to eliminate induced voltages in the measurement circuit. Because of the size of Hall sensors and their directional sensitivity — the field has to be perpendicular to the sensor surface — grooves must be machined in the tooling to place them close to the welding zone. Such machining changes the geometry of the working region and therefore the distribution of the magnetic field and of the magnetic pressure.

Mironov et al. [81] proposed microminiature Hall probes with a cross-section of 150 μm × 750 μm for magnetic field measurements in EMPT. The response of these probes is distorted by an inductive pickup contribution proportional to the rate of change of the magnetic field, dB/dt. Compensation requires an additional pickup sensor, and the Hall response must be corrected using the pickup response.

An alternative approach to magnetic-field measurement in MPW systems is the use of sensors based on nanostructured mixed-valence perovskite manganite films [78, 21, 18]. These films have the general composition $R_{1-x}A_xMnO_3$, where R is a trivalent rare-earth element, such as La or Nd, and A is a divalent alkaline-earth element, such as Ca, Sr, or Ba [82, 83]. Their most important property is the colossal magnetoresistance (CMR): a large decrease in electrical resistance when the material is exposed to a magnetic field. The magnetoresistance (MR) is commonly expressed as:

$$MR = \left[\frac{\rho(B)}{\rho(0)} - 1\right] \times 100\%, \tag{1.30}$$

where $\rho(B)$ is the electrical resistivity in the applied magnetic field and $\rho(0)$ is the resistivity in the absence of a magnetic field [84, 78]. Since $\rho(B) < \rho(0)$ in manganites, the magnetoresistance defined in this way is negative, and the discussion below refers to its magnitude.

The electrical and magnetic properties of manganite films depend on temperature and magnetic field, and on the film composition, thickness, and growth conditions [85]. A characteristic dependence of resistivity on temperature is shown in Fig. 1.19. (a). The resistivity exhibits a pronounced maximum at the metal–insulator transition temperature, T_m. The magnitude of the MR is also temperature dependent, reaching its highest value close to T_m and decreasing as the operating temperature increases over the transition point. The performance of a manganite-based magnetic field sensors can therefore be adapted to a given operating temperature by adjusting the properties of the films.

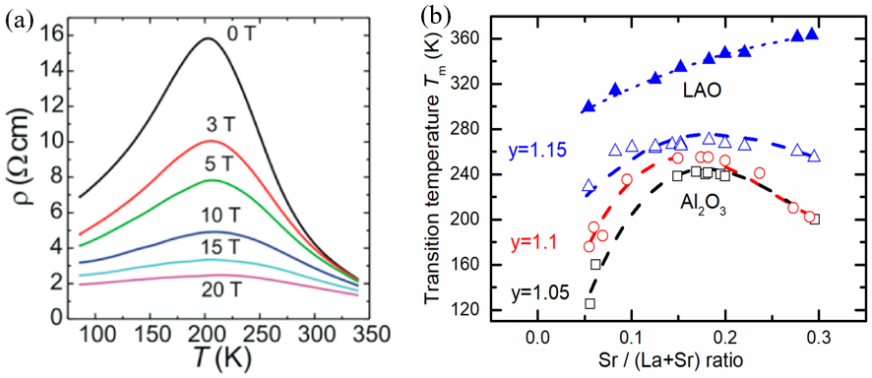


Fig. 1.12 (a) Temperature dependence of the resistivity of a $La_{0.83}Sr_{0.17}MnO_3$ film at different magnetic flux densities. Adopted from [85]. (b) Dependence of the metal–insulator transition temperature T_m on the Sr content for nanostructured LSMO films on Al_2O_3 (open symbols) and epitaxial LSMO films on LAO (filled symbols) with different Mn/(La+Sr) ratios *y*. Adopted from [86].

The required electrical and magnetic characteristics are obtained by changing the concentration of divalent dopants (Sr or Ca), adjusting the Mn concentration, varying the deposition conditions, or selecting an different substrate [85, 86]. The influence of Sr and Mn concentrations on the metal–insulator transition temperature is shown in Fig. 1.19 (b). In particular, for $La_{1-x}Sr_xMn_yO_3$ films, the transition temperature, the magnetoresistance and the magnetic field sensitivity are controlled through the composition ratios x = Sr/(La + Sr) and y = Mn/(La + Sr), which allows films to be adapted to different sensing applications.

The high magnetic-field sensitivity of these films has led to the development of CMR B-scalar sensors, which can operate at room temperature [87]. A photograph and a schematic three-dimensional cross-section of a typical CMR B-scalar sensor, including its sensing element and connecting cable, are shown in Fig. 1.20. These sensors measure the magnitude of the magnetic flux density within a very small sensing volume. They have been successfully employed for magnetic-field measurements in railgun systems [88], non-destructive pulsed-field magnets [21], and, more recently, in MPW and MPF systems [18, 89].

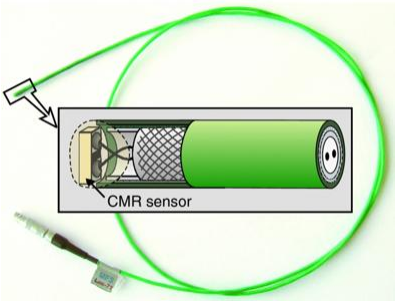


Fig. 1.20 Photograph and schematic three-dimensional cross-section of a CMR B-scalar sensor with its cable. Adopted from [87].

Unlike most of these applications, MPW is carried out at temperatures above room temperature, because the workpiece and the tooling heat up during repeated operation. Sensors intended for MPW therefore require a high magnetic field sensitivity over an elevated temperature range, which is achieved by increasing the Mn concentration in the manganite films. Excess Mn shifts the metal–insulator transition temperature T_m toward higher values [90], thereby increasing the magnetic field sensitivity of the films at temperatures above 20 °C. This shift is attributed to the formation of La vacancies, which modifies the charge balance of the perovskite lattice and increase the relative concentration of Mn^{4+} ions. The resulting increase in the Mn^{4+}/Mn^{3+} ratio strengthens the double-exchange interaction, raises the metal–insulator transition temperature, and reduces the electrical resistivity of the films [90].

Fig. 1.21 shows the influence of Mn excess on the electrical properties of LSMO thin films. Increasing the Mn/(La + Sr) ratio from 1.05 to 1.15 shifts T_m, from 240 K to 270 K and reducing the maximum resistivity, ρ_m, from 0.475 to 0.25 Ω cm. Since the sensor operates by detecting changes in electrical resistance induced by a magnetic field, the magnitude of the MR directly determines its magnetic field sensitivity.

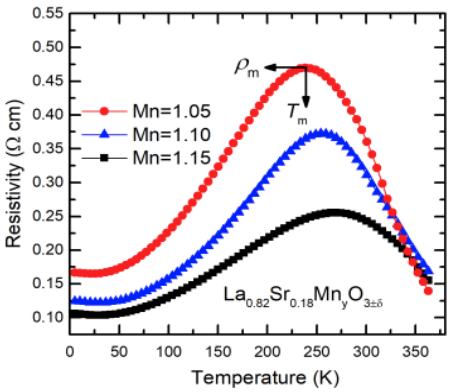


Fig. 1.21 Temperature dependence of the resistivity of LSMO films with different Mn/(La + Sr) ratios *y*. Adopted from [90].

Fig. 1.22 shows the magnetic field dependence of MR for LSMO films with different Mn concentrations measured at 300 K and 363 K [90]. These results demonstrate that increasing the Mn content raises the sensitivity at elevated temperatures. LSMO films with excess Mn were therefore used for the fabrication of the magnetic field sensors employed in the MPW system described in [18].

CMR B-scalar sensors have two further characteristics that distinguish them from conventional magnetic field sensors. The first is their very low magnetic anisotropy [91]. As a result, the sensor response depends only weakly on the orientation of the magnetic field relative to the sensor plane, so the sensor does not have to be aligned with the field direction during installation. The second is the bandwidth of the sensing element, which

extends to several hundred kilohertz and allows rapidly varying magnetic fields to be resolved [87, 92].

In the study reported in [18], CMR B-scalar probe were used to measure the magnetic flux density during MPW. The probes were too large to be placed in the field shaper–flyer gap, and had to be installed instead in a borehole drilled into the field shaper (Fig. 1.23). This requires the field shaper to be modified for sensor installation, whereas a non-invasive measurement technique compatible with existing industrial setups would be preferable. Furthermore, the borehole itself locally distorts the magnetic field, as confirmed by numerical simulations and reported in the same work [18]. For these reasons, the development of miniaturised probe that can be positioned directly within the gap is of significant importance.

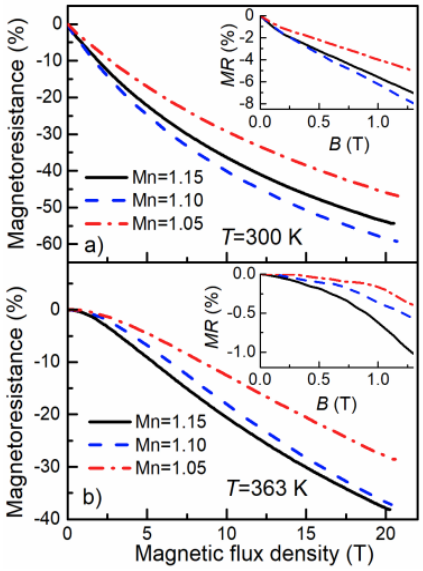


Fig. 1.22 Magnetic flux density dependence of the magnetoresistance of LSMO films with different Mn/(La+Sr) ratios y, measured at (a) 300 K and (b) 363 K. The insets show the low-field region on an enlarged scale. Adopted from [90].

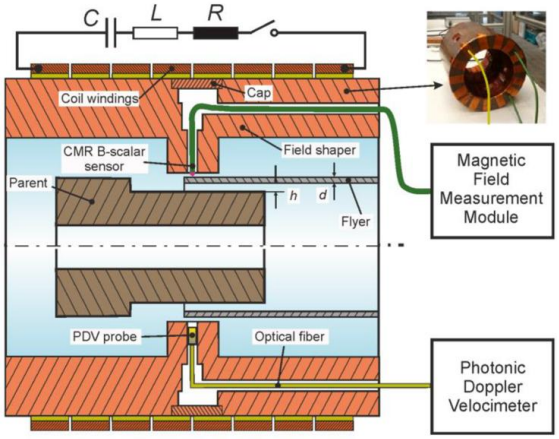


Fig. 1.23 MPW setup with a CMR B-scalar probe and a PDV probe installed in technological boreholes in the field shaper. *C*, *L* and *R* are the capacitance, inductance and resistance of the discharge circuit. The CMR B-scalar probe is inserted through one borehole, closed by a cap, and connected to the magnetic field measurement module; the PDV probe is placed in the opposite borehole. The inset is a photograph of the field shaper with the probe leads. Adopted from [18].

1.5 Post-Process Control in EMPT

Post-process control in EMPT is used to evaluate the result of the forming or welding operation. For MPF, the usual methods are dimensional inspection, visual examination, thickness measurements, and detection of cracks or local defects [93, 94, 95]. For MPW, post-process control additionally involves metallographic analysis of the welded interface, mechanical testing, leak testing, and non-destructive inspection methods such as ultrasonic, radiographic, or eddy current testing [17, 96]. Machine-learning-based inspection and automated classification have also been investigated for post-process quality assessment in EMPT [97].

Mechanical testing is used to evaluate the load-bearing capacity and the failure behaviour of MPW joints. Depending on the joint geometry, it includes tensile, shear, peel and hardness tests [17].

Lueg-Althoff et al. [98] investigated the influence of wall thickness on the quality of magnetic pulse welded aluminium–steel tube-to-tube joints. Narrow strips cut from the welded tubes were tested by an instrumented 90° peel test integrated into a tensile testing machine. The final geometry of selected specimens was recorded with a 3D scanner, and the weld zone was examined by optical microscopy.

Xu et al. [99] assessed the quality of aluminium–steel tube MPW joints by peeling tests, metallographic observation and scanning electron microscopy. The welded region was cut into axial strips, and the peeling test showed that higher impact velocity increased the joint strength. At an impact velocity of about 355 m/s, failure occurred through tearing of the aluminium tube, while aluminium remnants remained attached to the steel surface, which indicates that the strength of the joint exceeded that of the aluminium base material.

For tubular joints, torsion-shear testing is also used: one part of the welded assembly is fixed while the other is rotated, producing shear stresses along the welded interface [60]. Li et al. [100] evaluated the bonding strength of MPW Al/Fe lap joints using tensile-shear tests. The specimens were cut along the welding direction and tested in a universal testing machine. Since the joints fractured in the base aluminium plate rather than along the Al/Fe interface, the authors concluded that the bonding strength of the MPW joint was higher than that of the aluminium base material.

All of these methods are applied after the process has been completed, and most of them — metallography, peel and shear testing — destroy the joint that is being assessed.

1.6 FEM-Based Modelling of EMPT Processes

EMPT processes are transient, occur on a microsecond time scale and involve electromagnetic–mechanical coupling between the tool coil and the workpiece. Analytical models require simplifications of the coil and field shaper geometry, of the magnetic field distribution, of the material behaviour, and of the contact conditions. Finite element method (FEM) modelling is therefore widely used, since it allows the electromagnetic and mechanical problems to be solved in coupled formulations.

Among the available FEM tools, LS-DYNA is frequently applied to the simulation of EMPT processes [101, 8, 31]. In its electromagnetic solver the conducting regions — tool coil, field shaper and workpiece — are discretised by a finite element mesh, while the surrounding insulating region is treated by the boundary element method (BEM). This FEM–BEM formulation avoids generating a volume mesh for the surrounding air domain [11], which reduces the number of elements, the memory required and, in many cases, the computation time.

Mesh generation is an important stage of FEM-based EMPT modelling, because the accuracy of the calculated electromagnetic field depends on the element size [102]. Attention must be paid to the workpiece thickness, the coil–workpiece gap, the contact regions, and areas where high gradients of magnetic field, current density, stress, or strain are expected [103]. Since eddy currents are concentrated near the conductor surface due to the skin effect, the mesh in conducting parts has to be refined in these regions. Körner et al. [104] noted that a mesh resolution of approximately three to five elements per skin depth is commonly recommended. Excessive mesh refinement increases the computational time, so a mesh convergence study is usually required to find a compromise between numerical accuracy and simulation time.

Stankevič et al. [18] used numerical simulations to support the interpretation of magnetic field measurements during MPW with CMR B-scalar sensors. A three-dimensional LS-DYNA simulation was carried out for the welding of a 2 mm thick aluminium flyer tube onto a steel parent part, with the experimentally measured tool coil current used as the electrical input. The model was used to analyse the magnetic field dynamics, the flyer deformation, the radial velocity and the impact with the parent part. The results agreed qualitatively with the measured magnetic field dynamics and reproduced the characteristic change of slope in the magnetic field waveform during the first half-wave (Fig. 1.24).

The field shaper used in the experiments, however, contained radial boreholes for the integration of CMR B-scalar probes. Including these boreholes in the full three-dimensional LS-DYNA model would have required a very fine mesh and a correspondingly long computation, so they were omitted, and the model therefore overestimated the magnetic flux density at the sensor position. To evaluate this effect, additional three-dimensional COMSOL Multiphysics simulations were performed. They showed that the borehole in the field shaper produces a local reduction and a spatial inhomogeneity of the magnetic flux density: field at a point unaffected by the borehole was about three times higher than at the actual sensor position inside it. Scaling factors therefore had to be applied when the curves of Fig. 1.24 were constructed [18]. Drilling a borehole in the field shaper therefore perturbs the quantity being measured by a factor of about three, and the measured and calculated values are not directly comparable. A probe placed in the field shaper–flyer gap itself would remove both the modification of the tooling and the need for such scaling.

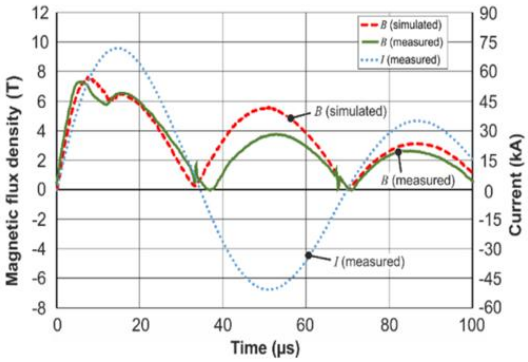


Fig. 1. 24 Magnetic field dynamics during the MPW of an aluminium tube to a steel parent: the scaled LS-DYNA simulation (Red dashed), the measured flux density (green) and the coil current (blue dotted). Adopted from [18].

COMSOL Multiphysics is another FEM package used for EMPT modelling. Amardas and Doshi [105] developed a three-dimensional FEM model of MPW with a single-loop coil. The electromagnetic problem was solved using the Magnetic Fields interface of the AC/DC module and the calculated Lorentz forces were transferred to the Structural Mechanics module as body loads in order to obtain the deformation, and the stresses in the flyer. The model contained more than 300,000 finite elements, and the flyer tube was meshed with 10 elements through its 1.5 mm thickness to improve the accuracy of the elastoplastic deformation calculation. The authors compared the input discharge current with the current calculated in the model and analysed the induced current density in the flyer and parent workpieces, the Lorentz force compressing the outer tube, the resulting stress distribution, and displacement and velocity of the outer tube.

Dhiware et al. [106] investigated electromagnetic pulse crimping of a D9 steel tube onto an SS316L(N) plug by combined numerical and experimental work. A two-dimensional axisymmetric model was built in COMSOL Multiphysics, with the AC/DC module for the electromagnetic part and the Solid Mechanics module for the deformation of the tube. According to the simulation flowchart presented in that work (Fig. 1.25), the electromagnetic problem was solved first in the Magnetic Fields interface, and its results were then transferred as body loads to the Solid Mechanics module. The simulation was used to analyse the current waveform, the magnetic flux density distribution (Fig. 1.26), the tube displacement, the impact velocity and the effective plastic strain. Increasing the discharge voltage increased the peak coil current, the magnetic flux density, the impact velocity (Fig. 1.27).

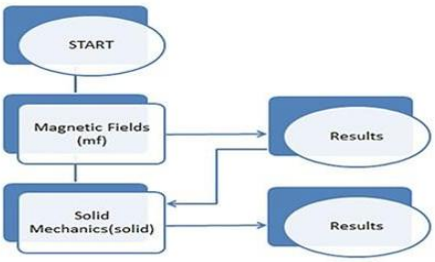


Fig. 1.15 Flowchart of the electromagnetic–mechanical simulation of MPC, in which the electromagnetic problem is solved first and its results are transferred as body loads to the mechanical problem. Adopted from [106].

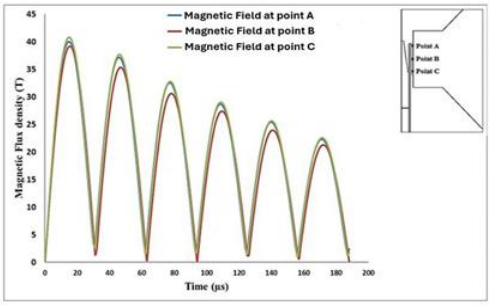


Fig. 1.14 Calculated magnetic flux density in the gap between the flyer tube and the field shaper at a discharge voltage of 15 kV. Adopted from [106].

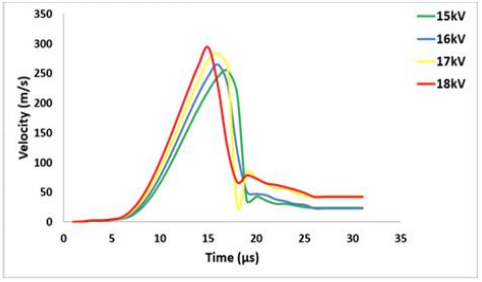


Fig. 1.13 Calculated time dependence of the radial velocity of the tube at different discharge voltages. Adopted from [106].

This model is based on a one-way coupling: the electromagnetic field is calculated first, and the resulting Lorentz forces are passed to the mechanical solver. The effect of the moving flyer on the electromagnetic field is therefore not taken into account, although during MPC and MPW the motion of the flyer changes the gap between the workpiece and the tool and hence the magnetic flux density. This is the same limitation as the one identified by Dond et al. [35] for relations established on

a stationary geometry. Such a model reproduces the general dependence of the flyer deformation and velocity on the discharge voltage, but not the magnetic field dynamics associated with the acceleration and impact of the flyer, and the calculated impact velocity should be interpreted accordingly.

1.7 Conclusions of Chapter 1

MPW is governed by coupling between the discharge circuit, the electromagnetic field and the mechanical response of the workpiece within a time interval of tens of microseconds: the transient magnetic field, the induced currents, the Lorentz forces, the deformation of the flyer and the collision conditions depend on one another and evolve throughout the pulse.

The magnetic field in the working gap determines the magnetic pressure acting on the flyer, provided that the wall thickness of the workpiece exceeds the skin depth by a factor of 1.5 to 2. The discharge current is recorded routinely and gives the peak current, the period and the damping of the circuit, but it characterises the circuit as a whole and not the conditions at the workpiece. The deformation and the acceleration of the flyer occur within the first current half-wave, and the maximum flyer velocity is reached after the current maximum. The instant of impact therefore cannot be determined from the current waveform.

Optical methods – shadowing, PDV and high-speed imaging – give the motion of the flyer, but require optical access to the moving surface, which is difficult in a gap of less than a millimetre. Contact methods give the impact time directly but require the parent workpiece to be replaced by the sensor.

Existing approaches to transient magnetic field measurement are limited in different ways: inductive probes require the output to be integrated and careful shielding; Hall sensors measure one field component, need to be aligned with the field and require grooves to be machined in the tooling; fibre-optic Faraday are sensitive to mechanical vibration; and the CMR B-scalar probes applied to MPW so far were too large for the working gap and had to be placed in a borehole in the field shaper, where the flux density differs from that in the gap by a factor of about three.

Post-process control establishes whether a sound joint was produced, and most of its methods destroy the joint being assessed.

A measurement of the magnetic field in the working gap that requires no modification of the tooling is therefore needed. Such a measurement would give the loading applied to the flyer during the pulse, allow mechanical events to be identified from the field waveform, and provide data for the validation of coupled electromagnetic–mechanical models without scaling factors.

2 METHODOLOGY

2.1 Magnetic Pulse Welding Setup

A custom-made magnetic pulse welding setup was developed for the experiments. It comprises a high-voltage power supply of up to 20 kV, an HVCAP-50UF-20KV capacitor [HVP High Voltage Products GmbH, Germany], a triggered high-voltage spark gap and a custom-made Bitter coil with a field shaper (Fig. 2.1 (a)). The capacitor is discharged through the Bitter coil by a spark gap triggered by reducing the pressure of the sulfur hexafluoride (SF_6) gas. Triggering through a third control electrode was not used, because it generates electromagnetic interference that disturbs the magnetic field measurement.

The experimental workplace with the Bitter coil and the magnetic field meter is shown in Fig. 2.1 (b). The setup operates in a tube compression configuration; Fig. 2.1 (b) shows an aluminium flyer tube and a steel parent rod installed before welding. Mechanical stoppers prevent the workpieces from being ejected from the coil. The magnetic field meter is synchronised with the trigger of the setup through an optical cable.

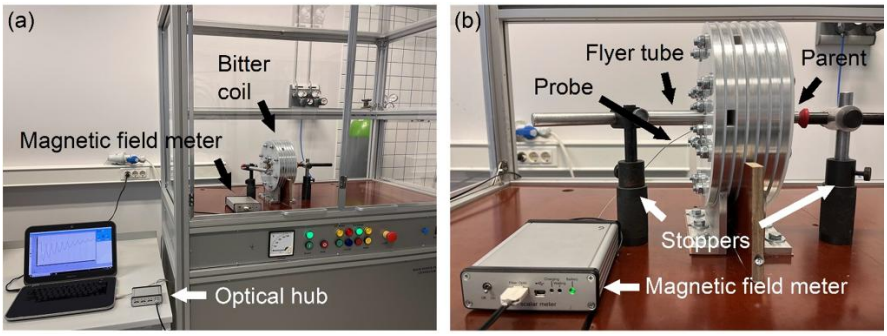


Fig. 2.1 (a) General view of the experimental setup. (b) View of Bitter coil with the installed flyer tube and cylindrical parent, mechanical stoppers, and magnetic field measurement system equipped with a CMR B-scalar probe.

The Bitter coil consists of five aluminium discs, each 8 mm thick, with an outer diameter of 216 mm and an inner diameter of 48 mm. The discs are separated by 2 mm thick polytetrafluoroethylene (PTFE) insulating inserts and are connected to one another by aluminium bridging plates, so that the current follows a helical path and the stack forms a five-turn coil. The copper field shaper inserted into the Bitter coil has an outer diameter of 46 mm and an inner diameter of 20.2 mm, with a 1 mm wide slit. The inner surface of the field shaper has a stepped profile, the innermost cylindrical section being

5 mm long; this section defines the length of the weld. Fig. 2.2 shows a cross-section of the field shaper with the flyer tube and the parent rod inserted before welding. In this work, *h* denotes the standoff distance between the flyer tube and the parent workpiece.

The discharge energy was set through the capacitor charging voltage according to Eq. (1.11). The welding experiments were carried out at discharge energies *E* of 1.6, 2.0 and 2.5 kJ, corresponding to charging voltages of 8.0, 9.0 and 10.0 kV (Table 2.1), and the standoff distance *h* was varied from 0.5 to 2.0 mm by selecting the parent rod diameter.

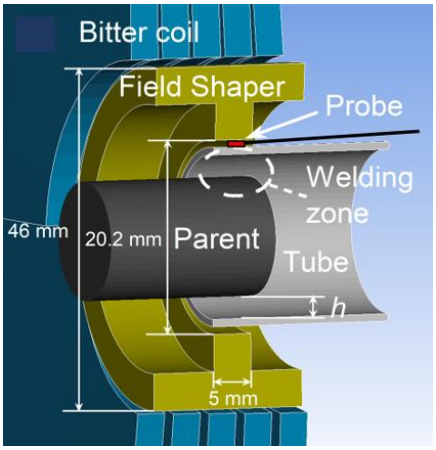


Fig. 2.2 Cross-section of the field shaper with the steel parent cylinder and the aluminium flyer tube inserted, and the CMR B-scalar probe placed in the gap between the field shaper and the flyer tube. *h* is the standoff distance between the flyer tube and the parent.

Before each experiment the flyer tube and the parent rod were positioned coaxially inside the field shaper. The CMR B-scalar probe was inserted from the side into the gap between the field shaper and the flyer tube (Fig. 2.2). This gap is 0.6 mm and is the same in all experiments, since the outer diameter of the flyer tube and the inner diameter of the field shaper were not changed; the standoff distance was varied through the parent rod diameter alone. The probe, the flyer tube and the parent rod were aligned and held in 3D-printed holders (Fig. 2.3), which fix their positions relative to one another and to the field shaper and prevent displacement during welding.



Fig. 2.3 3D printed holders and the variants of probe mounting

Table 2.1 Parameters of the MPW setup and tooling devices

Parameter	Symbol	Value	Units
Capacity	C	50	µF
Discharge energies during experiments	E	1.6, 2.0, 2.5	kJ
Bitter coil, number of windings	N	5	
Bitter coil, outer diameter	$D_{bitter\ out}$	216	mm
Bitter coil, inner diameter	$D_{bitter\ in}$	48	mm
Bitter coil, inductance	L	270	nH
Field shaper, outer diameter	$D_{FS\ out}$	46	mm
Field shaper, inner diameter	$D_{FS\ in}$	20.2	mm
Field shaper, working length	wl	5	mm

2.2 Materials and Workpiece

The welding experiments were carried out with an AA6063 aluminium flyer tube and AISI 304 stainless-steel parent cylinders with diameters D_p = 14, 15, 16, and 17 mm (Fig. 2.4). The flyer tube had an outer diameter D_f = 19 mm and a wall thickness s_f = 0.5 mm. The initial radial gap between the flyer and the parent cylinder, that is, the standoff distance h, follows from the parent diameter and was 0.5, 1.0, 1.5, and 2.0 mm respectively. The gap between the field shaper and the flyer tube, g = 0.6 mm, is the same in all experiments. The length of the welded overlap, l_{ovl} = 5 mm, is set by the innermost step of the field shaper (Table 2.2).

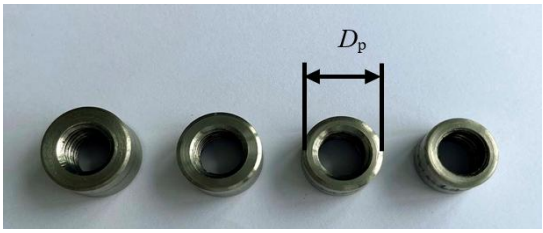


Fig. 2.4 The four stainless-steel parent cylinders used in the experiments, of diameter D_p = 17, 16, 15 and 14 mm (from left to right), corresponding to standoff distances h = 0.5, 1.0, 1.5 and 2.0 mm.

Before welding, the stainless-steel parent cylinder was screwed onto a threaded bolt (Fig. 2.5 (a)), which fixed its position and ensured coaxial alignment with the aluminium flyer tube. Fig. 2.5 (b) shows the assembly after the discharge, with the flyer tube, the parent cylinder and the bolt. The bolt served as a reusable holder: after each experiment it was removed from the welded assembly and a parent cylinder of a different diameter was screwed onto it, and the experiment was repeated at the selected discharge energy and standoff distance.

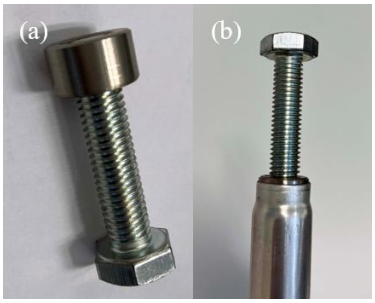


Fig. 2.5 (a) Stainless-steel parent cylinder with the threaded bolt screwed into it, used to grip the specimen in the tensile testing machine; (b) workpiece assembly after welding.

No surface preparation of the flyer tube or the parent cylinder was carried out before welding. The samples were neither polished nor chemically treated, no degreasing was applied, and the workpieces were used in the as-received state.

Table 2.2 Geometrical parameters of the MPW workpiece

Parameter	Symbol	Value	Units
Flyer tube outer diameter	D_f	19	mm
Flyer tube wall thickness	s_f	0.5	mm
Parent cylinder diameter	D_p	14, 15, 16, 17	mm
Standoff distance	h	0.5, 1.0, 1.5, 2.0	mm
Overlap length	l_{ovl}	5	mm
Gap between field shaper and flyer tube	g	0.6	mm

A separate series of experiments was carried out to study the dynamic response of the proximity sensor. In these experiments the target was a rotating segmented disc, made either of ferromagnetic S235JR steel (15% IACS) or of a non-ferromagnetic aluminium alloy (63% IACS). The discs were 5 mm thick and were cut into symmetrical segments spanning $\theta \approx 84^{\circ}$, the distance from the axis of rotation to the outer edge being $R = 57$ mm (Fig. 2.6). The rotation frequency frot was varied from 10 to 80 Hz (Table 2.3).

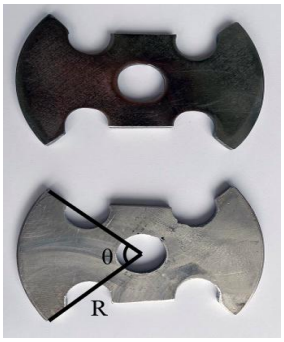


Fig. 2.6 Segmented rotating disks: (top) steel disk; (bottom) duralumin disk.

A commercial N35-grade neodymium permanent magnet, a solid cylinder 15 mm in diameter and 10 mm high, provided the DC bias magnetic field.

This grade was chosen because it gives a high magnetic flux density in a compact geometry.

Table 2.3 Parameters of the disks at the proximity sensing experiments

Parameter	Symbol	Value	Units
Rotating frequency	f_{rot}	10 - 80	Hz
Disc thickness	s_d	5	mm
Disc segment angle	θ	84	°
Disc radius	R	57	mm

2.3 Experimental Setup for Proximity Sensing

The proximity measurements were made with a magnetic proximity sensor consisting of an N35 neodymium permanent magnet and a CMR B-scalar sensor. The magnet creates a bias magnetic field, and the CMR B-scalar sensor measures the magnitude of that field. When a metallic object approaches the sensor or moves past it, the distribution of the magnetic field near the sensor changes, and this change appears in the sensor response.

To study the dynamic response of the sensor, a segmented disc was mounted on the shaft of an electric motor, perpendicular to its axis, and the sensor was positioned near the edge of the disc (Fig. 2.7 (a)). The CMR B-scalar sensor was placed at a radius $r = 50$ mm from the axis of rotation, and the gap between the surface of the disc and the surface of the permanent magnet was $d = 9$ mm (Fig. 2.7 (b)). The rotation frequency was varied from 10 to 80 Hz through the supply voltage of the motor.

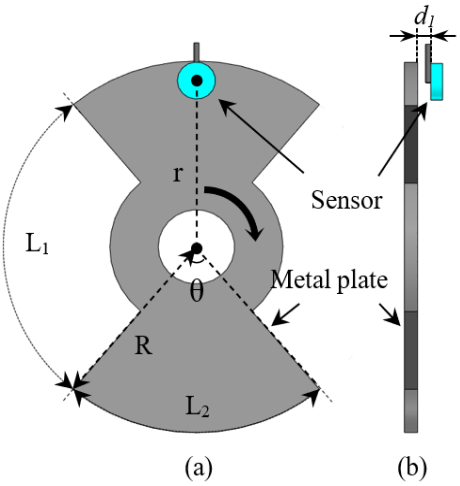


Fig. 2.7 Setup for the study of the dynamic response of the CMR-based magnetic proximity probe with the permanent magnet: (a) front view; (b) side view.

As the disc segments passed the sensor, the magnetic field at the sensor position changed periodically. For the aluminium disc this change is produced by the eddy currents induced in the moving conductor. For the steel disc the response is additionally affected by the redistribution of magnetic flux caused by the ferromagnetic properties of the material.

Rotational motion was chosen because it produces periodic motion of a metallic object past the sensor under reproducible conditions, which allows the response of the sensor to a ferromagnetic and to a non-ferromagnetic conductor to be compared under otherwise identical conditions.

2.4 Electrical Measurements

The discharge current was measured with a custom-made Rogowski coil (Fig. 2.8) connected to a Tektronix DPO3052 oscilloscope through a 20 dB attenuator, which reduces the amplitude of the coil output and prevents overloading of the oscilloscope input during high-current discharges. Since the output voltage of the Rogowski coil is proportional to the time derivative of the current, the recorded voltage was integrated numerically and the discharge current was obtained as: $I(t) = k \int u(t)\, dt$.



Fig. 2.8 Custom-made Rogowski coil for MPW setup.

The coefficient $k = 8.1 \times 10^8$ A/(V·s) was determined by calibration against a reference current source of known amplitude and refers to the response recorded at the oscilloscope input, that is, after the 20 dB attenuator. The response was taken to be linear over the range up to 95 kA.

The capacitor charging voltage was set and monitored with a TECHNIX SR20KV-3KW high-voltage power supply. The highest charging voltage used was 10 kV, corresponding by Eq. (1.11) to a discharge energy of 2.5 kJ. Under these conditions the peak discharge current I_{peak} in the Bitter coil, measured with the Rogowski coil, was 95 kA, and the oscillation period was 32 μs (Table 2.4).

Table 2.4 Discharge parameters of the MPW setup

Voltage, kV	Energy, kJ	I_{peak}, kA
8	1.6	76
9	2.0	85
10	2.5	95

2.5 CMR B-scalar sensor

Two types of CMR B-scalar sensor structure were used. Both were based on $La_{0.8}Sr_{0.2}Mn_{1.15}O_3$ films deposited by pulsed-injection metal–organic chemical vapour deposition (PI-MOCVD) on polycrystalline Al_2O_3 substrates. The excess of manganese in this composition shifts the metal–insulator transition temperature upwards and keeps the magnetoresistive sensitivity high at temperatures above 20 °C (see subsection 1.4.4). The two structures differ in the geometry of the active area and therefore in their electrical resistance.

The structure used for the magnetic proximity sensor, together with the N35 permanent magnet, was a two-terminal element. Its active area was rectangular, 50 μm long along the current direction and 500 μm wide.

The structure used for the transient magnetic field measurements during MPW was made on a 0.35 μm thick film with a smaller active area, 20 μm long along the current direction and 400 μm wide. Reducing the active area lowers the resistance of the element to ~ 200 Ω, which improves the impedance matching and the integrity of the response on the microsecond time scale of the MPW discharge.

2.6 Magnetic Field Measurement Probes and System

The transient magnetic field during MPW was measured with thin custom-made CMR B-scalar probes placed directly in the gap between the field shaper and the aluminium flyer tube, so that the magnetic flux density $B(t)$ was recorded in the region where the magnetic pressure acts on the flyer. Two probe designs were used, shown in Fig. 2.9.

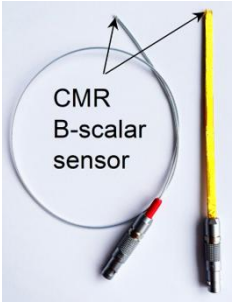


Fig. 2.9 Two custom-made probe designs.

The resistance of the film decreases as the magnetic flux density increases, and the recorded voltage is converted into $B(t)$ using a calibration curve measured individually for each sensor.

The probe response was recorded with the magnetic field meter shown in Fig. 2.10 (a, b) [107]. The novel electrical design of this meter suppressed EMFs induced in the wires of magnetic field probe, in combination with electromagnetic shielding, reduces the influence of interference and ensures that the recorded response contains only the components caused by the CMR B-scalar sensor reacting to the magnetic field variations.

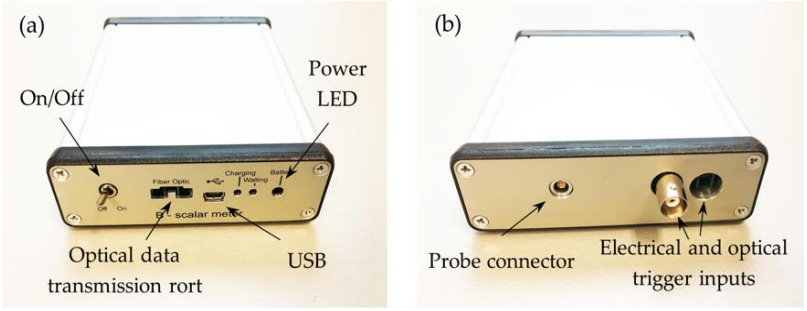


Fig. 2.10 Measurement unit of the magnetic field meter: (a) front (b) back side.

The meter records pulses with amplitudes up to 20 T and durations about 16 μs. The response is digitised with a 16-bit ADC at up to 25 MS/s, corresponding to a sampling interval of 80 ns. The digitised data are transmitted to a computer through an optical cable, and a four-channel optical hub (Fig. 2.1 (a)) provides the data transfer and the galvanic isolation between the meters and the computer. The conversion of the recorded voltage into magnetic flux density in tesla was carried out on the computer using the calibration curve of the corresponding probe.

For the proximity measurements, a hand-held magnetic field meter with a CMR B-scalar probe was used [91]. It consists of a hand-held electronic unit and a pluggable probe containing a CMR B-scalar sensor, a permanent magnet and a temperature sensor (Fig. 2.11); the temperature reading is used to correct the magnetic-field response for temperature variations. The instrument displays the recorded waveform on a graphical colour touch screen and stores it in internal memory, so that no external oscilloscope is required. In the proximity experiments the response of the probe to the passing disc segments was recorded in this internal memory.



Fig. 2.11 Hand-held magnetic field meter with a pluggable probe containing a CMR B-scalar sensor, a Pt1000 temperature sensor and a cylindrical permanent magnet.

2.7 Numerical Modelling in COMSOL Multiphysics

The transient magnetic field in the gap between the field shaper and the flyer, and the deformation of the flyer tube produced by it, were calculated in COMSOL Multiphysics. The model is two-dimensional and axisymmetric and includes the tool coil, the field shaper, the flyer tube, the parent rod and the surrounding air (Fig. 2.12 (a)). Because the model is axisymmetric, it does not represent the axial slit of the field shaper and therefore describes the magnetic field under the assumption of azimuthal symmetry. The geometry and the material properties were taken from the experimental conditions (Tables 2.1 and 2.2).

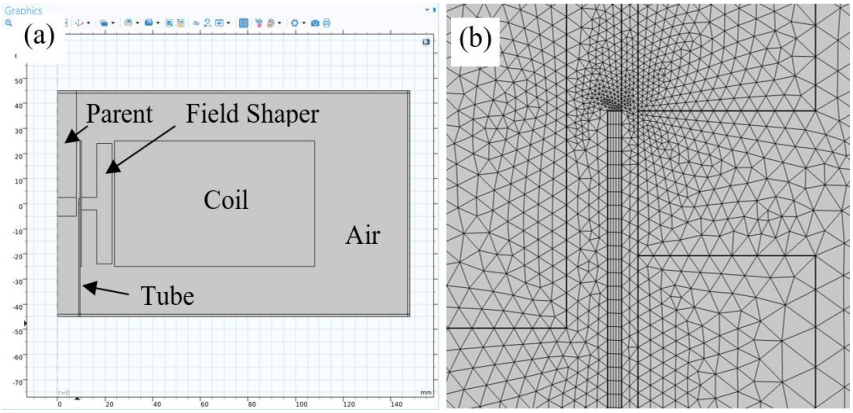


Fig. 2.12 (a) Two-dimensional axisymmetric model comprising the tool coil, the field shaper, the flyer tube, the parent rod and the surrounding air; (b) finite element mesh of the computational domain near the welding zone.

The electromagnetic problem was solved in the Magnetic Fields interface using the magnetic vector potential formulation in the quasi-static approximation, with the air domain surrounded by an infinite element domain representing the unbounded exterior region. The experimentally measured current waveform was imposed as the excitation of the tool coil. The current is therefore an input to the model and not a quantity by which it is validated; the calculated magnetic flux density in the gap were compared with the measurements. Temperature effects were not included in the model, as is usual when the purpose of the calculation is to obtain the collision parameters [108].

The Magnetic Fields and Solid Mechanics interfaces were coupled through the Lorentz force, applied as a body load on the flyer tube. The mechanical behaviour of the aluminium tube was described by the experimentally obtained stress–strain curve shown in Fig. 2.13, which was used as the material input. The contact between the flyer tube and the parent rod was

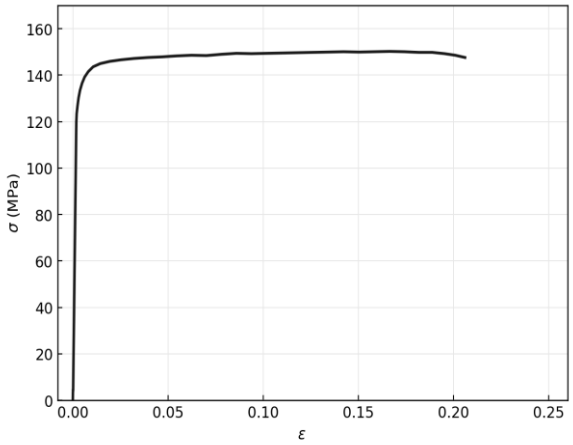


Fig. 2.13 Engineering stress–strain curve of the AA6063 tube material.

represented by a contact formulation with adhesion. This prevents the surfaces from separating after the impact and allows the calculation to continue beyond contact; it is a numerical representation of the joint and does not reproduce the mechanism of bond formation.

The motion of the flyer was followed with the Moving Mesh interface. The air domain between the field shaper and the flyer was defined as deforming domains, with the mesh displacement on the boundaries of the flyer prescribed by the displacement computed in the Solid Mechanics interface and smoothing inside the domains. The tool coil, the field shaper and the parent rod were treated as fixed domains.

The computational domain was discretised with local refinement in both air gaps, within the wall of the flyer tube and near the contact region, where high electromagnetic and mechanical gradients are expected. In the gap between the field shaper and the flyer the maximum element size was set to 0.6 mm, equal to the width of the gap, and the mesh was refined further by the automatic mesh generator in the gap and at the end face of the flyer tube, where the geometry produces a local field concentration (Fig. 2.12 (b)).

At the discharge frequency of the setup the skin depth in the aluminium flyer is approximately 0.5 mm, that is, comparable with the wall thickness of 0.5 mm, so the induced current density varies appreciably across the wall and cannot be treated as confined to the outer surface. The number of element layers through the wall was determined by repeating the calculation with an increasing number of layers. Beyond five layers, the calculated radial velocity of the flyer remained unchanged; therefore, five layers were used. This corresponds to five elements per skin depth and is consistent with mesh

resolutions commonly used to resolve skin-depth effects in electromagnetic simulations of MPW [109, 104].

The transient problem was solved over the period from 0 to 32 μs, with the solution stored every 0.1 μs, which gives 160 stored points over the first current half-wave, where the deformation and the impact of the flyer occur. The solver was free to subdivide this interval, and the internal time step was controlled by the default relative tolerance of 0.01. The time resolution of the stored solution is therefore 0.1 μs, which is comparable with the timing uncertainty of the magnetic field measurements.

2.8 Tensile Testing and Joint Characterisation

The tensile tests were carried out on a TIRA 2300 universal testing machine (TIRA GmbH, Germany) with a load capacity of 100 kN, at room temperature (Fig. 2.14). The tests on the AA6063 tube specimens were performed in accordance with EN 10002. The welded joints were tested on the same machine using the arrangement described below.

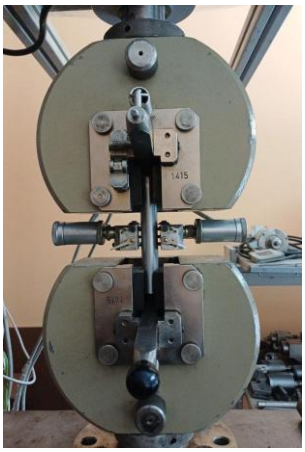


Fig. 2.14 Tensile testing of the aluminium tube using a TIRA 2300 testing machine equipped with a contact extensometer.

The axial elongation of the AA6063 tube specimens used to determine the stress–strain response was recorded with an MFX-500-B extensometer with a resolution of 0.001 mm; these tests were performed at a strain rate within the range specified by the standard, of the order of 10^{-3} s^{-1}. For the welded joints the extensometer could not be attached across the joint, so only the load and the crosshead displacement were recorded.

To determine the stress–strain response of the flyer material, AA6063 tubes were loaded in tension to fracture. The engineering stress was calculated from the measured force and the initial cross-sectional area of the tube, 29.1 mm^2, and the engineering strain from the extensometer reading and the initial gauge length of 50 mm.

The curve was obtained under quasi-static loading, whereas the strain rates during MPW are of the order of 10^4 s^{-1} [110], so strain-rate hardening is not represented in the material model. The influence of this simplification on the

calculated flyer motion is limited, because the stress produced by the magnetic pressure exceeds the flow stress of the tube by about an order of magnitude.

The welded joints were tested on the same machine. The threaded bolt screwed into the stainless-steel parent cylinder (see Fig. 2.5) was held in one grip of the machine and the aluminium flyer tube in the other, so that the load was applied along the axis of the joint. Each specimen was loaded monotonically until separation, and the force–displacement response was recorded; the maximum load $F_{\max}$ (kN) was used to characterise the joint. Twelve welded specimens were tested, one for each combination of the three discharge energies and the four standoff distances (Tables 2.1 and 2.2). Since each combination is represented by a single specimen, the results are used to identify trends rather than to establish statistically significant differences.

After testing, the separated surfaces were examined by optical microscopy. Aluminium remaining on the surface of the parent cylinder was taken to indicate the bonded regions, and its axial extent, measured from the same images, was taken as the effective weld length. This is a measured quantity and is not necessarily equal to the nominal overlap length $l_{\mathrm{ovl}} = 5$ mm set by the field shaper (Section 2.2).

2.9 Conclusions of Chapter 2

A magnetic pulse welding setup was built around a five-turn Bitter coil with a copper field shaper and a 50 μF capacitor. The experiments were carried out at discharge energies of 1.6, 2.0 and 2.5 kJ and standoff distances from 0.5 to 2.0 mm, with peak discharge currents from 75 to 95 kA. Thin CMR B-scalar probes based on $La_{0.8}Sr_{0.2}Mn_{1.15}O_3$ films were placed directly in the 0.6 mm gap between the field shaper and the flyer tube, so that the magnetic field is recorded where the magnetic pressure acts and no modification of the field shaper is required. The parasitic EMF induced in the probe wiring is suppressed by bipolar excitation, and the response is digitised with 16-bit resolution at up to 25 MS/s, that is, with a sampling interval of 80 ns, for pulses of up to 20 T and durations as short as 16 μs.

A coupled electromagnetic–mechanical model of the process was built in COMSOL Multiphysics. The mesh follows the moving flyer, so that the gap between the field shaper and the flyer changes during the pulse instead of being held fixed. The wall of the flyer is resolved by five element layers, which is necessary because the skin depth, about 0.5 mm, is comparable with the wall thickness. Two assumptions limit the model: it is axisymmetric and therefore does not represent the axial slit of the field shaper, and the material data were obtained under quasi-static loading, whereas the strain rate during welding is of the order of $10^4\ s^{-1}$.

The welded joints were characterised by tensile testing and by optical microscopy of the fracture surfaces, with twelve specimens covering the three discharge energies and the four standoff distances, one specimen per combination. The results obtained with these methods are presented in Chapter 3.

3 RESULTS AND DISCUSSION

3.1 Short Pulsed Magnetic Field Measurements

3.1.1 Magnetic Field Meter with EMF Compensation

EMPT processes are accompanied by short, high-amplitude magnetic field pulses, with magnetic flux density reaching several tens of tesla and pulse durations from about ten to a few hundred microseconds. Measurement of such fields requires specialised probes and magnetic field meters that are able to operate under fast transient conditions and strong electromagnetic interference. Commercial magnetic field measurement systems are not suitable for this task, because they are not designed for direct measurements of high-amplitude microsecond magnetic field pulses in narrow and geometrically constrained working gaps under the electromagnetically noisy conditions of EMPT equipment.

A critical problem in measuring short-pulsed magnetic fields in EMPT setups is the parasitic electromotive force (EMF) induced in the transmission lines and sensor contacts by the rapidly changing magnetic field. Since the field changes within a few microseconds, any conductive loop formed by the sensor contacts and wires is penetrated by a time-varying magnetic flux, which by Faraday's law produces an induced voltage:

$$U_{EMF}(t) = -\frac{d\Phi(t)}{dt}, \tag{3.1.1}$$

where U_{EMF} is the induced electromotive force (V), and Φ, is the magnetic flux through the parasitic loop (Wb). The measured voltage U_{mes} is therefore not determined only by the magnetoresistive response of the CMR sensor U_{CMR} alone, but also contains an inductive component U_{EMF}, which is proportional to the rate of change of the flux through the parasitic loop:

$$U_{mes}(t) = U_{CMR}(t) + U_{EMF}(t), \tag{3.1.2}$$

Several approaches have been proposed to reduce or compensate for this inductive component. One approach is to minimise the effective loop area of the sensor wiring by using bifilar or twisted-pair connections [89]. In this configuration, the voltages induced in neighbouring wire segments have opposite polarities and partly cancel each other. Such wiring reduces the parasitic EMF, but does not compensate it completely in microsecond high-amplitude measurements.

Another approach uses an additional compensation loop, acting as a B-dot sensor placed close to the CMR B-scalar sensor. In this case, the loop has a geometry similar to that of the sensor current leads and mainly records the

voltage $U_{\text{B-dot}}$ induced by the time-varying magnetic flux. The useful CMR response is obtained by subtracting the compensation-loop response from the measured response:

$$U_{CMR}(t) = U_{mes}(t) - A \cdot U_{B-dot}(t), \tag{3.1.3}$$

where *A* is an empirical weighting coefficient. This method has been used to extend the frequency range of CMR B-scalar sensors and to reduce the influence of induced loop-effect voltages [92]. However, it requires an additional compensation loop with its own connection wires, careful matching of the loop geometry, and calibration of the coefficient *A*. Where the magnetic field has a strong spatial gradient, a small displacement between the CMR sensor and the compensation loop introduces a compensation error.

A method for measuring short magnetic field pulses with durations in the range of 20−100 μs was proposed in [89]. The sensor is excited with a bipolar square-wave voltage. The CMR response changes sign when the polarity of the sensor excitation voltage is reversed, whereas the EMF induced in the connecting wires remains nearly unchanged during two adjacent positive and negative half-periods, so that processing the voltages measured during a positive and the following negative half-period cancels the induced component:

$$U(B) = \frac{[+U(B) + U_{EMF}] - [-U(B) + U_{EMF}]}{2}, \tag{3.1.4}$$

where $U(B)$ is the useful voltage response of the CMR sensor; $+U(B)$ and $-U(B)$ are the sensor voltage components corresponding to positive and negative excitation half-periods (Fig. 3.1.1). The EMF terms cancel and the resistive response of the sensor remains. For a given excitation current this response is proportional to the sensor resistance, which is converted into the magnetic flux density B using the calibration curve of the sensor.

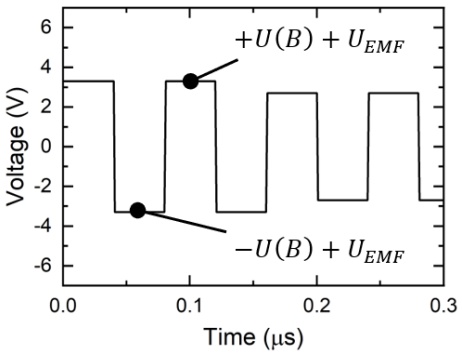


Fig. 3.1.1 Sensor voltages recorded during two adjacent half-periods of the bipolar excitation, at positive and negative polarity. The magnetoresistive response reverses sign with the excitation polarity while the induced parasitic electromotive force does not.

Since one value of B is obtained from a pair of adjacent half-periods, the frequency of the bipolar excitation determines the time resolution of the reconstructed waveform. In the developed meter the CMR sensor is excited at frequencies up to 12.5 MHz, at which one value of B is obtained every 80 ns. When square-wave pulses of such frequency are transmitted to the sensor through the connecting lines, their shape is distorted by the distributed capacitance and inductance of the line, by the impedance mismatch between generator, cable and sensor, and by the resulting reflections. The half-periods applied to the sensor become rounded and may be asymmetric or accompanied by oscillations, which reduces the accuracy of the EMF compensation.

The electrical resistance of the sensor is therefore an important parameter of the measuring system, and a low-resistance CMR sensor was required, capable of measuring magnetic fields of several tens of tesla while operating with a bipolar excitation voltage at frequencies of up to 12.5 MHz. Such a combination of requirements is not offered by commercially available magnetic field sensors. Therefore, specially prepared low-resistance $La_{0.8}Sr_{0.2}Mn_yO_3$-based CMR structures were used in this work.

The developed microsecond high-amplitude magnetic field meter (Fig. 3.1.2) consists of a magnetic field probe with a CMR B-scalar sensor, a bipolar pulse-voltage generator, a signal amplifier, an analog-to-digital converter, a microcontroller, and USB and fibre-optic interfaces for communication with a personal computer (Fig. 2.10).

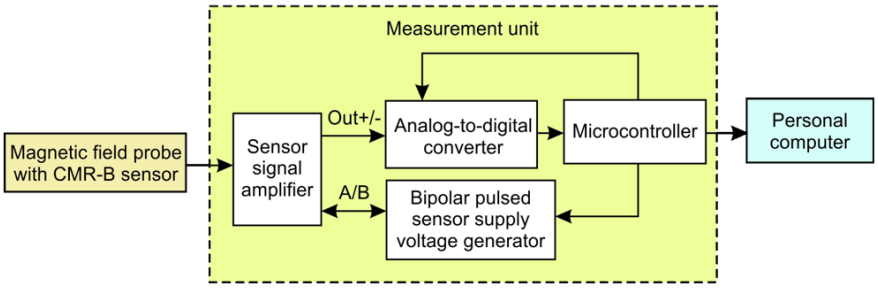


Fig. 3.1.2. Block diagram of the magnetic field meter with suppression of the parasitic electromotive force: the CMR B-scalar probe, the bipolar pulse generator, the amplifier, the analog-to-digital converter and the microcontroller.

During the measurements, the meter recorded the response of the CMR sensor. The response was transferred to a computer through the fibre-optic interface, which provided galvanic isolation between the measuring electronics and the computer. The magnetic flux density waveform $B(t)$ was reconstructed in post-processing using the calibration curve of the corresponding sensor [107].

The shape of the bipolar excitation voltage across the sensor was investigated for the developed magnetic field meter. The measurements were performed at the frequencies of 1.25 MHz and 6.43 MHz. The resulting waveforms are shown in Fig. 3.1.3 (a, b).

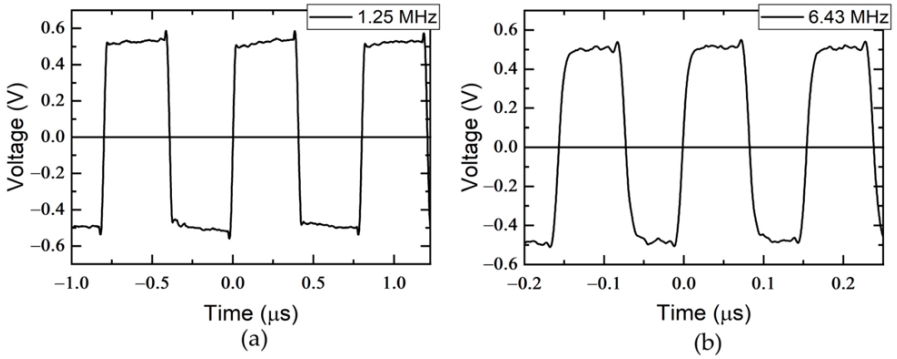


Fig. 3.1.3 Transients of bipolar pulsed excitation voltage across the sensor at voltage frequencies (a) 1.25 MHz and (b) 6.43 MHz.

As the frequency increases, the rounding of the rising and falling edges becomes more pronounced; at 6.43 MHz the rise and fall times were 14 ns and 16 ns respectively. The distortion is attributed to transmission-line effects, that is, to the parasitic inductance and capacitance of the line and to the impedance mismatch between the pulse generator, the connecting lines and the sensor. These contributions to the distortion were reduced in the present work. The parasitic inductance of the probe leads was lowered by twisting them bifilarly, which reduces the area of the loop enclosed by the connections. The time constant associated with the parasitic capacitance of the line was shortened by lowering the resistance of the CMR element, since this time constant is set by the product of that resistance and the line capacitance. The low-resistance CMR structures developed for this purpose are described in Section 3.2.

3.1.2 Experimental Validation of the Magnetic Field Meter in Pulsed Magnetic Field

The developed magnetic field meter with the CMR sensor was tested on the MPW equipment described in Section 2.1. During the test, the sensor was positioned at the Bitter coil with a field shaper, as shown in Fig. 3.1.4 (a). The capacitor was charged to the required voltage and then discharged into the Bitter coil through a triggered spark gap. The magnetic field generated in the coil changed the resistance of the CMR sensor, and the resulting voltage change was recorded and processed by the measurement system. Fig. 3.1.4 (b) shows the voltage response obtained after processing for the developed

bipolar- excitation measurement system. For comparison, Fig. 3.1.4 (c) shows the voltage across the sensor when it was supplied with a constant current; these measurements were performed using an earlier generation of measurement system, described in [87].

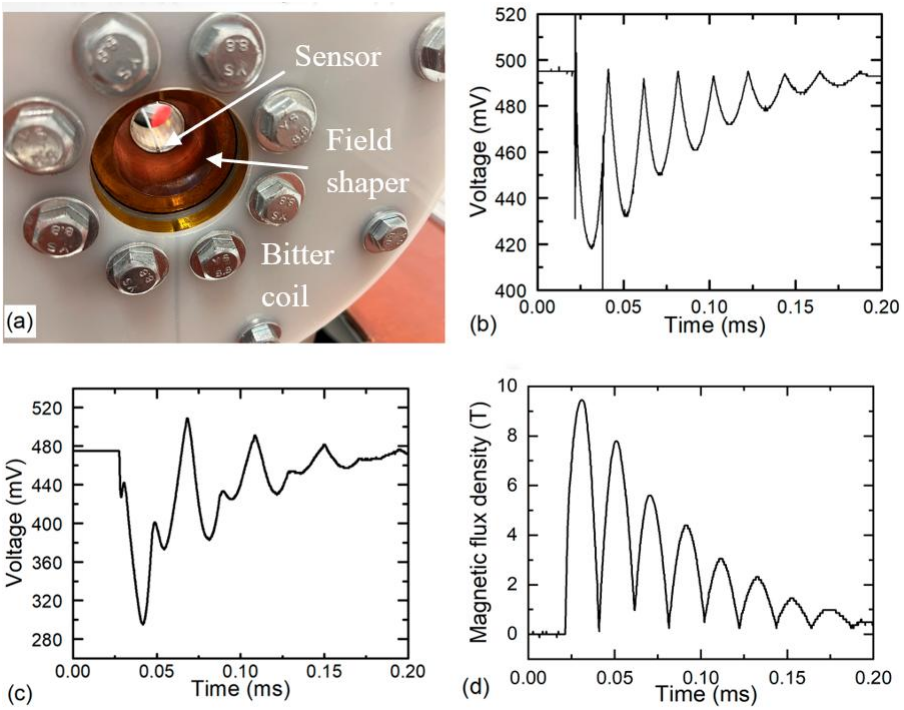


Fig. 3.1.4 Testing of the magnetic field meter on the MPW setup: (a) the CMR B-scalar probe positioned in the field shaper installed in the Bitter coil; (b) voltage response obtained with the bipolar sensor excitation after subtraction of the two polarities according to Eq. (3.1.4); (c) voltage across the sensor recorded with a constant-current supply, measured with the earlier generation of the measurement system [87]; (d) magnetic flux density at the inner surface of the field shaper, reconstructed from the recorded sensor response using the sensor calibration curve at a discharge energy of 1.6 kJ.

When the sensor is supplied with a constant current, the output response contains both the voltage change caused by the magnetic-field-induced change in sensor resistance and the parasitic voltage induced in the probe leads. With a bipolar excitation, the induced component is cancelled during processing, so that the remaining response corresponds to the change caused by the magnetic field.

Compensation of the parasitic voltage by bipolar excitation is effective only when that voltage remains nearly constant over two adjacent half-periods of the excitation, that is, when it varies slowly compared with the excitation period. In these measurements (see Fig. 3.1.4 (b)) the voltage across the sensor

is additionally disturbed by a short, high-frequency transient produced by the spark gap. This transient does not satisfy the above condition and is therefore not removed by the bipolar excitation; reducing it requires improved shielding of the probe wiring.

An example of a magnetic flux density measurement is shown in Fig. 3.1.4 (d), recorded with the new version of the meter at a charging voltage of 8 kV, which corresponds to a discharge energy of 1.6 kJ. The system recorded the positive and negative voltages across the sensor; the microprocessor processed them according to Eq. (3.1.4) and converted the result into resistance, which was then converted into magnetic flux density using the appropriate calibration curve from the calibration table. The resistance measured before the pulse was used to determine the temperature of the sensor and hence to select that curve. Since the CMR B-scalar sensor measures the magnitude of the magnetic flux density, the recorded waveform is unipolar. The maximum flux density at the inner surface of field shaper, with no workpiece inserted, reaches approximately 9.4 T.

3.1.3 Conclusions of Section 3.1

A magnetic field measurement module was developed for high-amplitude, short-duration magnetic fields in MPW. It combines a CMR B-scalar probe, a bipolar pulse generator, a signal amplifier, a 16-bit digitiser and a fibre-optic link to the computer, and reconstructs the magnetic flux density from the recorded sensor response using the calibration curve.

The frequency of the bipolar excitation sets the time resolution of the reconstructed waveform, since one value of B is obtained per excitation period: 80 ns at 12.5 MHz. Tested on the MPW setup, the measurement module recorded a magnetic flux density of 9.4 T at the inner surface of field shaper at a charging voltage of 8 kV, with markedly less interference than the earlier constant-current version of the instrument.

3.2 Magnetic Field Probes Designs

3.2.1 Low Resistivity CMR B-Scalar Sensor

A series of $La_{1-x}Sr_xMn_yO_3$ films with a thickness of 350 nm were deposited on a polycrystalline Al_2O_3 substrate using the pulsed-injection metal-organic chemical vapor deposition (PI-MOCVD) [107]. Since for polycrystalline films, the insulator–metal transition temperature is achieved at a Sr content of approximately $x \approx 0.2$ (see Fig. 1.19) the composition $La_{0.8}Sr_{0.2}Mn_yO_3$ with different Mn excess y were investigated.

The temperature dependence of the resistivity ρ was investigated using a closed-loop helium gas cryocooler over the temperature range of 77–310 K. The magnetoresistance (MR), defined by Eq. (1.30), was measured over the range 80–350 K in pulsed magnetic fields with a duration of 1 ms and amplitudes of up to 20 T. The magnetic field pulses were generated by a non-destructive pulsed magnet, in which a capacitor was discharged through a multi-turn magnetic field coil [111].

Fig. 3.2.1 (a) shows the temperature dependences of resistivity for the films with $y = 1.1$ and $y = 1.15$. The film with $y = 1.15$ has a resistivity maximum ρm = 0.245 Ω·cm at an insulator–metal transition temperature $T_m = 270$ K, whereas for $y = 1.1$ the transition shifts to $T_m = 240$ K and the resistivity maximum rises to $\rho_m = 0.28$ Ω·cm.

The dependence of MR on magnetic flux density B for LSMO films with different Mn contents at different temperatures is shown in Fig. 3.2.1 (b, c). At 270 K, films with $y = 1.1$ show the highest MR magnitude compared to those with $y = 1.15$. However, at higher temperatures up to 350 K, the trend is reversed and the films with $y = 1.15$ show slightly higher MR values.

To investigate the origin of the observed changes in the electrical and magnetic properties of the films, their crystal structure was analyzed by transmission electron microscopy (TEM). Fig. 3.2.1 (d, e) show low-magnification cross-sectional TEM images of films with different compositions. The images reveal a columnar microstructure, with crystallite columns extending through the entire film thickness and oriented perpendicular to the substrate. However, no significant structural differences, such as changes in column width or grain boundary area, were observed between films with different Mn excess. Therefore, the observed differences in the temperature dependence of the resistivity and magnetoresistance are attributed mainly to changes in the Mn concentration, which affect the Mn^{4+}/Mn^{3+} ratio [112].

Based on these results, and considering that the sensors are intended to operate at room temperature and above, LSMO films with a Mn content of $y = 1.15$ were selected for the fabrication of magnetic field probes. These films exhibit lower resistivity and a weaker temperature dependence of magnetoresistance, which makes them more suitable for stable sensor operation under the selected conditions.

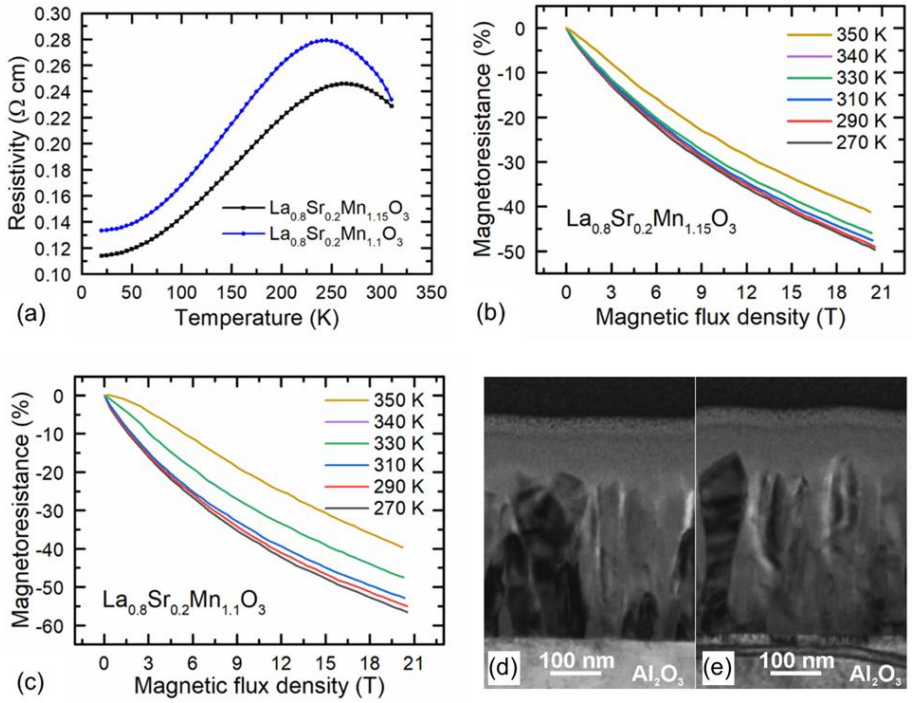


Fig. 3.2.1 (a) Temperature dependences of resistivity for LSMO films with different Mn contents. Magnetoresistance dependences on magnetic flux density for films with Mn excess $y = 1.15$ (b) and $y = 1.10$ (c) at different ambient temperatures. Cross-sectional bright-field TEM images of the films with $y = 1.10$ (d) and $y = 1.15$ (e).

3.2.2 CMR B-Scalar Magnetic Field Probes for MPW Investigation

For probe fabrication the selected LSMO films were patterned by photolithography and chemical etching, and the electrical contacts were formed by thermal evaporation of Cr and Ag layers in two stages. First, a 20 nm thick Cr layer was deposited to provide adhesion between the electrodes and the film. Then, a 0.5 μm thick Ag layer was deposited and annealed for 1 h at 450 °C in an Ar atmosphere. The distance d between the electrodes was selected in the range of 10–20 μm, depending on the resistivity of the films, to obtain a sample resistance of approximately 250 Ω. To allow the connecting wires to be soldered, a further Ag layer about 2 μm thick was

deposited and annealed under the same conditions. Finally, the substrates with the patterned films were then cut into sensors measuring 1 × 0.5 mm^2. The sensor structure and dimensions are shown in Fig. 3.2.2 (a, b, c).

Three probe designs were developed based on CMR B-scalar sensor: a flexible wired probe (Fig. 3.2.3 (a)), a probe in rigid housing (Fig. 3.2.3 (b)) and flexible printed circuit board (PCB) probe (Fig. 3.2.3 (c)).

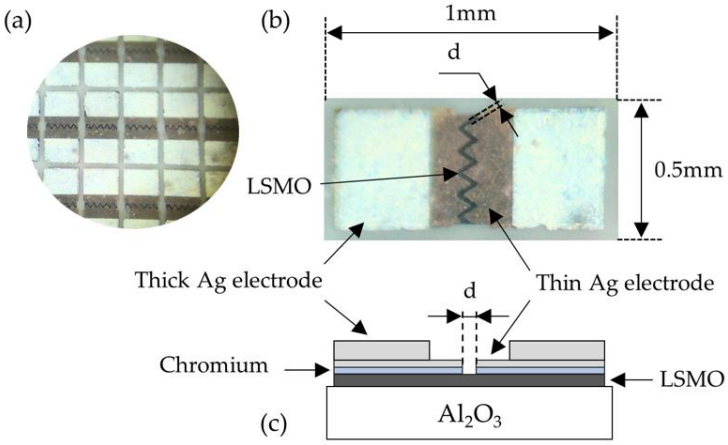


Fig. 3.2.2 Optical micrograph of the LSMO sensing elements on the Al_2O_3 substrate after patterning by photolithography and wet etching. (b) Optical micrograph of a single sensing element. (c) Schematic cross-section of the sensing element.

The fabrication of the flexible wired probe (Fig. 3.2.3 (a)) begins with the preparation of bifilarly twisted copper wires of 50 μm diameter with a varnish insulating coating. The bifilar twisting reduces the effective loop area of the sensor circuit and therefore the parasitic inductive voltage picked up in a rapidly varying magnetic field. The twisted wires were soldered to the sensor contacts at a temperature below 270 °C to avoid damage to the sensor. The active area of the sensor was then covered with hot-melt adhesive, which protects the film from the atmosphere and mechanically reinforces the soldered joints. The twisted-wire cable was shielded against high-frequency electromagnetic noise by a braided sleeve, and the shielded cable and the sensor were enclosed in a PTFE cover providing additional protection against high voltage. The minimum outer diameter of the flexible wired probe is approximately 1 mm.

The probe in a rigid housing uses the same sensor connection, with the sensor and the connecting wires enclosed in a hard plastic tube with a handle (Fig. 3.2.3 (b)). Its minimum outer diameter is approximately 3 mm.

In the third design, the sensor was soldered to a flexible PCB with copper conductive traces (Fig. 3.2.3 (c)). The crossed conductive traces on the

flexible PCB form a bifilar-like connection to the sensor, reducing the parasitic voltage induced during pulsed magnetic field measurements. Aluminium foil shielding and polyimide film insulation were then applied to provide electromagnetic shielding and electrical insulation. This design gives flat probes with a minimum thickness of approximately 0.6 mm, and it is the design used for the measurements in the field shaper–flyer gap without the need for drilling technological holes, machining channels or otherwise modifying the base components of the welding tool (Fig. 3.2.4 (a, b)).

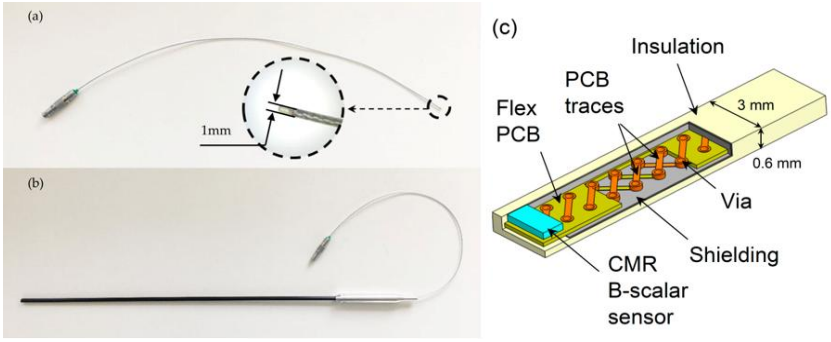


Fig. 3.2.3 Three configurations of the CMR B-scalar probe, all based on the same $La_{0.8}Sr_{0.2}Mn_{1.15}O_3$ sensing element: (a) wire-based flexible probe, 250 mm long, wire diameter 1 mm; (b) rigid probe in a plastic housing of 3 mm diameter; (c) cross-section of flexible printed-circuit-board (PCB) probe, 3 mm wide and 0.6 mm thick

All probes are connected to the magnetic field meter through a LEMO connector. This connector provides a reliable detachable connection, ensures proper contact of the signal and shielding lines, and allows probes to be exchanged rapidly during the experiments.

An internal guide, produced by stereolithography 3D printing (Fig. 3.2.4 (a, b)), was used to position the probe reproducibly with respect to the field shaper and the flyer tube, and also to align the flyer tube inside the field shaper. Reproducible positioning is necessary because a small change in the position of the probe, or vibration during welding, alters the measured magnetic flux density in the narrow working gap.

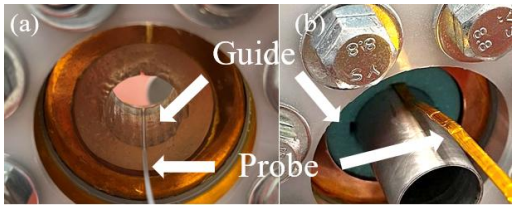


Fig. 3.2.4 Examples of sensor placement methods: (a) flexible wired probe fixed in a 3D-printed guide (b) flexible PCB probe fixed in a 3D-printed guide with an inserted flyer tube.

Each sensor was calibrated after fabrication over the temperature range of 273–333 K in magnetic fields up to 20 T. The calibration was performed using a specially designed long-pulse high-magnetic-field generator, which produces a semi-sinusoidal magnetic field pulse with a duration of approximately 1 ms and an amplitude of up to 20 T [111]. The reference field was obtained from a calibrated B-dot sensor with numerical integration of its output. The long pulse duration was chosen to reduce the parasitic electromotive force induced in the sensor wires, which is proportional to the time derivative of the magnetic field: the calibration is thus carried out under conditions in which this contribution is small, whereas during the MPW measurements, where it is large, it is removed by the bipolar excitation described in Section 3.1. The calibration procedure is described in more detail in [87]. The calibration gave the dependence of the sensor resistance on magnetic flux density at different temperatures, stored as calibration tables in the memory of the measuring device; during measurements the microprocessor uses these tables to convert the recorded voltage change across the sensor into magnetic flux density. All probes were calibrated in pulsed magnetic fields up to 20 T, which defines the upper limit of the measurement range of the system. The fields recorded in the present MPW experiments, up to 16.5 T, lie within this range.

3.2.3 Conclusions of Section 3.2

$La_{0.8}Sr_{0.2}Mn_yO_3$ films 350 nm thick with different manganese excess were compared. The film with $y = 1.15$ has an insulator–metal transition at 270 K with a resistivity maximum of 0.245 Ω·cm, against 240 K and 0.28 Ω·cm for $y = 1.1$. Transmission electron microscopy showed no difference in column width or grain boundary density between the two compositions, so the change is attributed to the manganese content through the Mn^{4+}/Mn^{3+} ratio. Films with $y = 1.15$ were therefore selected for the probes, which operate at room temperature and above.

Sensors of 1×0.5 mm² with an active area of 400×10 µm² and a resistance of about 250 Ω were fabricated from these films by photolithography, etching and evaporated Cr–Ag contacts. This resistance is what allows the sensor to be excited by a bipolar square-wave voltage at megahertz frequencies, since the time constant of the connecting line is set by the product of the sensor resistance and the line capacitance.

Three probe designs were built around this sensor, with minimum outer dimensions of 1 mm for the flexible wired probe, 3 mm for the probe in a rigid housing and 0.6 mm for the flat probe on a flexible PCB. Bifilar wiring and bifilar-like PCB traces, together with braided or foil shielding, reduce the inductive voltage picked up by the sensor circuit; the short high-frequency interference produced by the spark gap is reduced by shielding, as discussed in Section 3.1.

Each sensor was calibrated over the range 273–333 K in fields up to 20 T using half-sinusoidal pulses of about 1 ms duration, for which the induced parasitic EMF is small. The resulting resistance–flux density dependences are stored as calibration tables in the meter and used to convert the recorded sensor response into magnetic flux density.

The flat 0.6 mm probe can be placed in the gap between the field shaper and the flyer tube without drilling holes or machining channels in the tooling.

3.3 Investigation of Magnetic Field Dynamics in the Gap Between the Flyer and Field Shaper During MPW Process

3.3.1 Current Measurement

The discharge current is the source of the magnetic field in the gap between the field shaper and the flyer tube, but the relation between them is set by the geometry of the field shaper and of the workpiece rather than by the coil alone, which is why the field in the gap is measured directly in this work. As discussed in Section 1.1, the current waveform in an EMPT circuit is determined by the equivalent capacitance, resistance, and inductance of the discharge circuit. When a conductive workpiece is placed inside the field shaper, the system has to be treated as a coupled primary–secondary circuit. The conductive workpiece acts as a short-circuited secondary coupled to the tool coil and field shaper and the eddy currents induced in it change the effective resistance and inductance of the coupled system and, consequently, affect the amplitude, oscillation period, and damping of the discharge current.

Fig. 3.3.1 (a) shows the discharge current waveforms at 1.6 kJ for two experimental configurations: an empty field shaper and a field shaper with a solid aluminium rod 19 mm in diameter inserted in it. In both cases, the current flowing through the tool coil exhibits a damped oscillatory waveform, in agreement with the current waveform described by Eq. (1.12). When the aluminium rod is inserted, the peak current reaches approximately 76 kA, whereas without the rod it reaches 73 kA. Compared to the empty field shaper configuration, the oscillation period decreases from 34 µs to about 32 µs, and the damping becomes more pronounced. The observed reduction in the oscillation period can be attributed to a decrease in the effective inductance of the coupled coil–field shaper–rod system, while the stronger damping

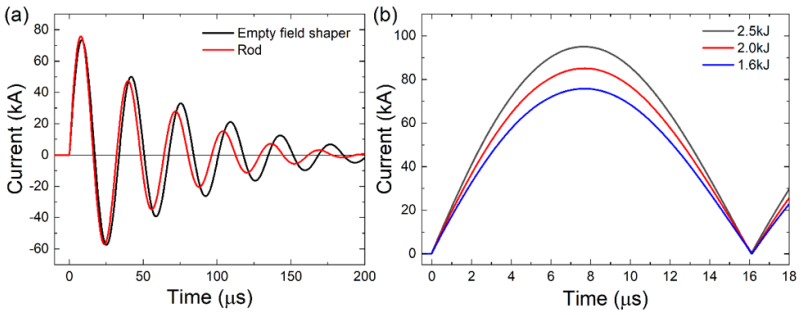


Fig. 3.3.1 Discharge current measured with a Rogowski coil. (a) Current at a discharge energy of 1.6 kJ for the field shaper without a workpiece and with a non-deformable solid aluminium rod inserted into it. (b) First half-wave of the current with the same rod inserted, at discharge energies of 1.6, 2.0 and 2.5 kJ.

indicates an increase in the effective resistance due to energy dissipation associated with eddy currents induced in the conductive rod.

Fig. 3.3.1 (b) shows the first half-period of the discharge current for different discharge energies with the rod inserted. The peak current increases with increasing discharge energy: approximately 76 kA at 1.6 kJ, 85 kA at 2.0 kJ, and 95 kA at 2.5 kJ. Higher stored energy produces a higher discharge current. This trend is expected, since the energy stored in the capacitor is proportional to the square of the charging voltage, as described by Eq. (1.11).

The experimentally obtained current waveforms were subsequently used as input data in the COMSOL Multiphysics model, ensuring consistency between the experimental and numerical analyses (see subsection 3.3.4).

3.3.2 Magnetic Field Measurement

A series of preliminary magnetic field measurements was carried out before the MPW experiments. In all of them the probe was placed directly against the inner wall of the field shaper and the discharge energy was 1.6 kJ. The purpose was to characterise the magnetic field dynamics for different tool configurations.

Fig. 3.3.2 (a) shows the magnetic field waveforms for two configurations: an empty field shaper (red curve) and a field shaper with an aluminium rod inserted (black curve). Cross-sections of both configurations are shown in Fig. 3.3.2 (b, c). The measured magnetic flux density is a damped oscillation.

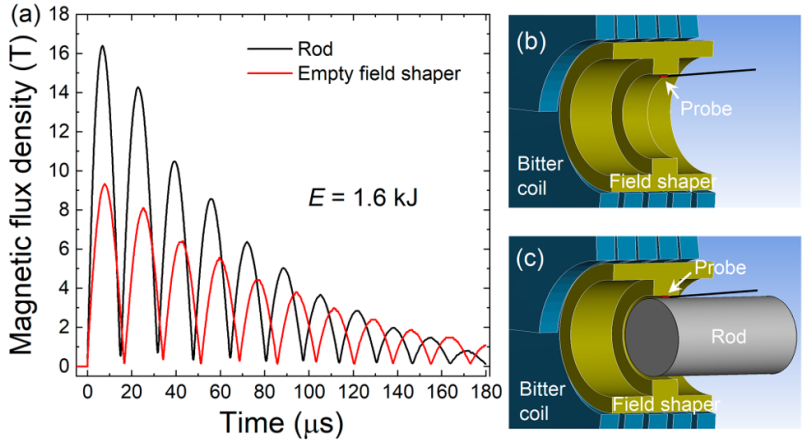


Fig. 3.3.2 (a) Magnetic flux density versus time measured by the CMR B-scalar probe inside the field shaper without a workpiece (red curve) and with an aluminium rod inserted (black curve). (b, c) Schematic cross-sections of the experimental configuration showing the probe position: (b) without a workpiece; (c) with the rod, the probe placed in the 0.6 mm gap between the field shaper and the rod surface. The rod diameter is 19 mm and the discharge energy 1.6 kJ.

Its decay is described by an exponential time constant τ = 110 μs for the empty field shaper and τ = 80 μs with an aluminium rod 19 mm in diameter inserted. The amplitude of the magnetic flux density rises from 9.4 T for the empty field shaper to approximately 16.5 T with the rod, and the oscillation period decreases.

The increase of the amplitude follows from the eddy currents induced in the rod. The current induced on the outer surface of the rod flows in the direction opposite to the current on the inner surface of the field shaper, and the magnetic fields produced by these two antiparallel current sheets are directed the same way in the space between them, so that they add at the probe position.

The changes of period and damping follow from the same coupling. The rod acts as a short-circuited secondary circuit coupled to the tool coil and the field shaper, as described by Eqs. (1.15) and (1.18). The coupling reduces the effective inductance of the primary circuit, which shortens the oscillation period, and increases its effective resistance, which accounts for the shorter decay time constant. A corresponding decrease in the oscillation period is seen in the measured discharge current, Fig. 3.3.1 (a).

Fig. 3.3.3 (a) shows the first half-period of the magnetic flux density measured with an aluminium tube of 19 mm outer diameter inserted into the field shaper and allowed to deform freely during the discharge (blue dashed curve), together with the waveform measured with a solid aluminium rod of the same diameter (black solid curve). The two curves coincide during the

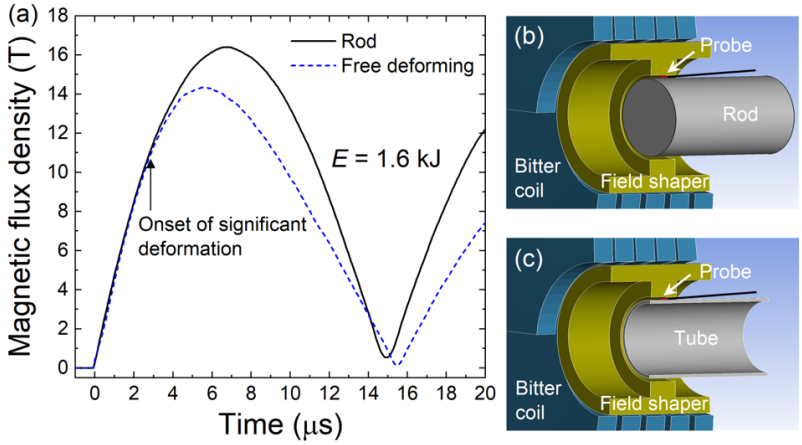


Fig. 3.3.3 (a) Magnetic flux density versus time during the first half-wave, measured in the gap between the field shaper and the workpiece, for an aluminium tube (blue dashed curve) and for a solid aluminium rod of the same outer diameter (black curve). Schematic cross-sections of the two configurations: (b) solid rod, (c) tube. The outer diameter of both the rod and the tube is 19 mm, the tube wall thickness is 0.5 mm, and the discharge energy is 1.6 kJ.

initial rise. From 2.4 µs onwards the field measured between the field shaper and the tube becomes lower and reaches its maximum earlier than in the case of the rod, the waveform departs from the sinusoidal shape observed with the rod, and the first half-period lasts longer.

This behaviour follows from the onset and the subsequent development of the deformation of the tube. As the coil current rises, the magnetic field in the gap and the magnetic pressure it produces rise with it, Eq. (1.7). While this pressure is below the value required to deform the tube, the magnetic field evolves as it does for the solid rod of the same outer diameter.

Once the magnetic pressure is sufficient to start the deformation, indicated by the black arrow in Fig. 3.3.3 (a), the tube begins to move radially inwards, which widens the gap between the field shaper and the outer surface of the tube. The field at the probe position, produced by the superposition described above, therefore decreases, and the magnetic flux density reaches its maximum while the coil current is still rising. The deformation is predominantly plastic, since the tube retains a reduced diameter after the pulse. The widening gap also weakens the coupling between the tool and the workpiece, which raises the effective inductance of the circuit and lengthens the oscillation period relative to the rod, in which no deformation occurs.

These preliminary measurements show that the solid rod can be used as a reference configuration. The rod does not deform during the discharge, so its waveform reflects only the electromagnetic response of the tool coil–field shaper–insert system. The departure of the waveform measured with the freely deforming tube from the waveform measured with the rod, Fig. 3.3.3 (a), therefore identifies the onset of the deformation of the tube.

In the next experiment the magnetic field was measured with a stainless-steel parent cylinder inserted into the aluminium tube, Fig. 3.3.4 (a, red curve), with an enlarged view of the first half-period in Fig. 3.3.4 (b). The parent cylinder was 17 mm in diameter, which gives a standoff distance $h_1 = 0.5$ mm between the inner wall of the tube and the surface of the parent, Fig. 3.3.4 (c). The discharge energy was 1.6 kJ. The waveform measured with the solid aluminium rod is included for comparison in Fig. 3.3.4 (a and b, black curve).

The first peak of the magnetic field measured between the field shaper and the tube (red curve in Fig. 3.3.4 (a, b)) exhibits an asymmetric shape, with a distinct bend observed between 7 and 8 µs, as indicated by the red arrow in Fig. 3.3.4 (b). The appearance of this bend can be attributed to the collision of the flyer tube with the steel parent cylinder. After this transition the second and subsequent peaks of the damped waveform are smooth half-waves of decreasing amplitude with no further features, which shows that the

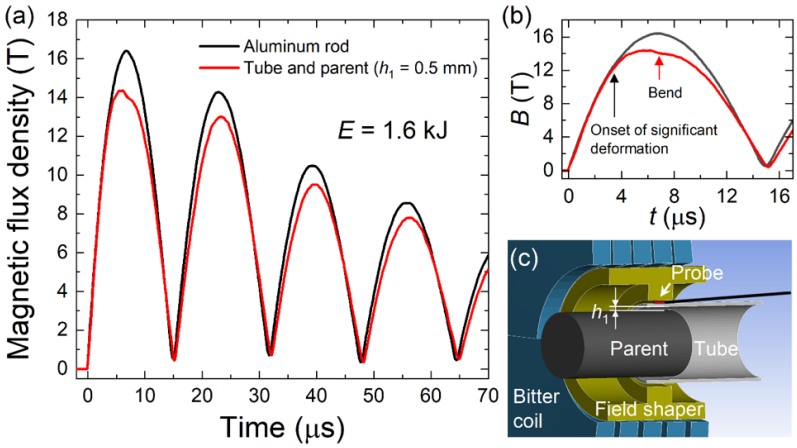


Fig. 3.3.4 Magnetic flux density measured in the gap between the field shaper and the workpiece: for a non-deformable aluminium rod (black) and for an aluminium tube that deforms during the process (red). (b) Magnified view of the first peak; the red curve departs from the black one at $t \approx 2.4$ μs, which is attributed to the onset of plastic deformation of the tube. (c) Schematic cross-section of the field shaper, probe and workpieces before the discharge, showing the probe gap of 0.6 mm and the standoff distance $h_1$of 0.5 mm. The discharge energy is 1.6 kJ.

deformation of the flyer and its impact on the parent occur within the first half-period of the magnetic pulse.

A comparison between the tube and solid aluminium rod experiments shows that the amplitude of the second magnetic-field peak is lower in the tube case. For the solid aluminium rod, the second peak reaches 14.3 T, whereas for the aluminium tube after collision with the parent cylinder it reaches 13 T. This decrease can be explained by the change in the final geometry after impact. During deformation, the flyer tube moves toward the parent cylinder, increasing the distance between the outer tube surface and the CMR B-scalar probe by approximately the initial standoff distance h_1. As a result, the local resultant magnetic flux density at the probe position decreases. From the second peak onwards, the measured magnetic field corresponds to the post-impact geometry of the joined tube–parent assembly.

To verify this, the tube–parent system was subjected to two successive magnetic field pulses at identical charging conditions, each corresponding to 1.6 kJ. The first capacitor discharge caused deformation of the flyer tube and its collision with the steel parent. The second discharge was applied to the already joined tube–parent assembly, in which the tube was firmly compressed against the parent. Fig. 3.3.5 (a) presents the experimental results: the red curve corresponds to the magnetic field dynamics during the first discharge, while the black dashed curve represents the field dynamics during the second discharge when subjected the already joined tube–parent assembly.

From the second peak onwards, the two magnetic field curves are in phase, exhibiting identical amplitude and period. Within the first peak (Fig. 3.3.5 (b)), matching between the curves is observed only after the bend. This indicates that the bend marks the end of impact (7 μs), after which the joined assembly reaches a stationary geometry configuration as shown in Fig. 3.3.5 (c).

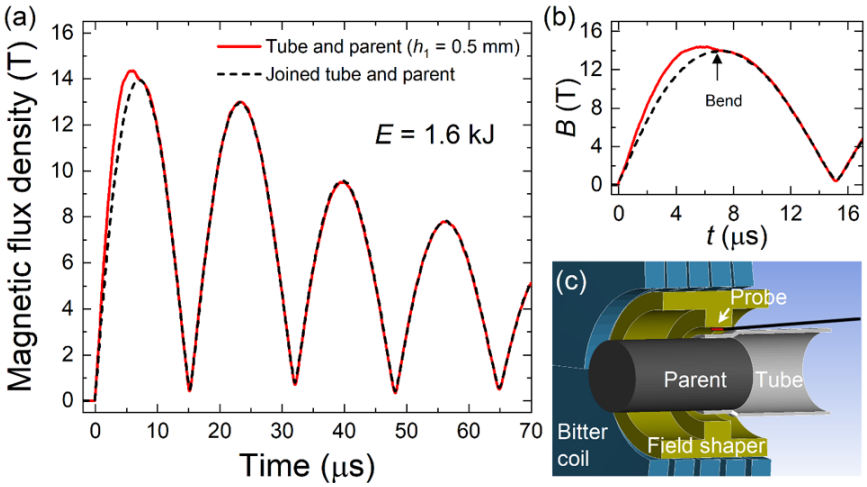


Fig. 3.3.5 (a) Magnetic flux density measured in the gap between the field shaper and the workpiece during magnetic pulse welding (red) and during a repeated discharge on the already welded assembly, in which the tube is permanently joined to the parent part (black dashed). (b) Magnified view of the first peak: the two curves differ while the tube is still moving and coincide after the bend, indicating that the tube has reached its final position against the parent part. (c) Schematic cross-section of the field shaper, probe and workpieces after welding. The discharge energy is 1.6 kJ.

In the subsequent series of experiments, the standoff distance h between the flyer tube and the parent was varied. The outer diameter of the tube remained constant 19 mm, while the diameter of the parent cylinder varied from 17 to 14 mm. Thus, the standoff distance between the inner surface of the tube and the parent ranged from 0.5 to 2 mm, respectively. The magnetic field dynamics was measured under identical discharge energy of 1.6 kJ. Experimental results for parent diameters of 17 mm (standoff distance h_1 = 0.5 mm, red curve) and 16 mm (standoff distance h_2 = 1 mm, blue curve) are shown in Fig. 3.3.6 (a). An enlarged view of the first half-period is presented in Fig. 3.3.6 (b).

Fig. 3.3.6 (b) shows that the first peaks of the red and blue dashed curves coincide during the initial rise of the magnetic field. The maximum magnetic field amplitude (14.4 T) and the time (6 μs) at which it occurs are identical in both experiments. As was mentioned above, for standoff distance h_1, a distinct

bend appears at 8 μs (see Fig. 3.3.6 (b), red arrow), whereas for h_2 at this time the magnetic field decreases smoothly, and pronounced bend occurs at 9.8 μs (see Fig. 3.3.6 (b), blue arrow). In the second case, the bend in the magnetic field waveform and the corresponding collision of the tube and the parent occurs later. Moreover, the magnetic field after the collision is lower than in the first case due to smaller total diameter of joined tube–parent assembly (see Fig. 3.3.6 (a)).

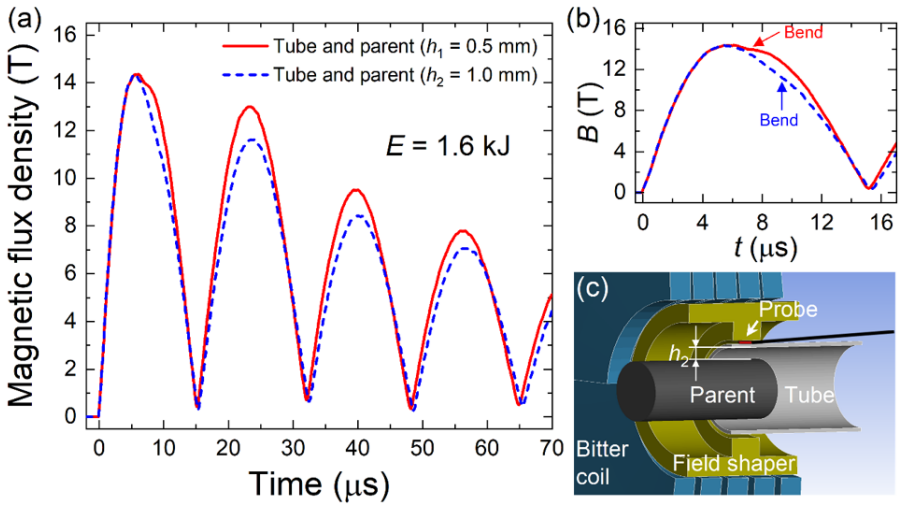


Fig. 3.3.6 (a) Magnetic flux density measured in the gap between the field shaper and the tube for two standoff distances, h_1 = 0.5 mm (red) and h_2 = 1 mm (blue dashed). (b) Magnified view of the first peak: the curves coincide while the outer geometry is still identical and separate at the kinks marked by the arrows, which correspond to the collision of the tube with the parent part for h_1 (red arrow) and for h_2 (blue arrow). (c) Schematic cross-section of the field shaper, probe and workpieces before the discharge, with both standoff distances indicated. The discharge energy is 1.6 kJ.

The first peak of magnetic flux density dynamics measured during experiments with parents of different diameters and corresponding standoff distances h_1, h_2, h_3, h_4 are presented in Fig. 3.3.7 (a). The initial magnetic flux density dynamics in first peaks remain identical due to the same capacitor discharge energy. The longer time required for the flyer tube to collide with the parent is associated with the larger initial standoff distance between them, and the bend in the curve (see Fig. 3.3.7 (a), black, red, and blue arrows corresponding to the respective curves) occurs at later times.

The experimental results obtained at different capacitor discharge energies for a standoff distance of 0.5 mm are shown in Fig. 3.3.7 (b). An increase in discharge energy results in an earlier collision of the tube with the parent (see Fig. 3.3.7 (b), black, red, and blue arrows corresponding to the respective curves). It can be seen that the amplitude of the first magnetic flux

density peak increases with increasing discharge energy. The maximum magnetic flux density rises from 14.4 T at 1.6 kJ to 15.8 T at 2.0 kJ and 16.5 T at 2.5 kJ. Furthermore, the characteristic bend associated with collision occurs earlier as the discharge energy increases. At higher discharge energies the higher magnetic flux density produces a higher magnetic pressure, which accelerates the flyer tube more strongly, so that it reaches the parent sooner. The characteristic collision times, related to both standoff distance and discharge energy, are summarized in Table 3.3.1 (see subsection 3.3.3).

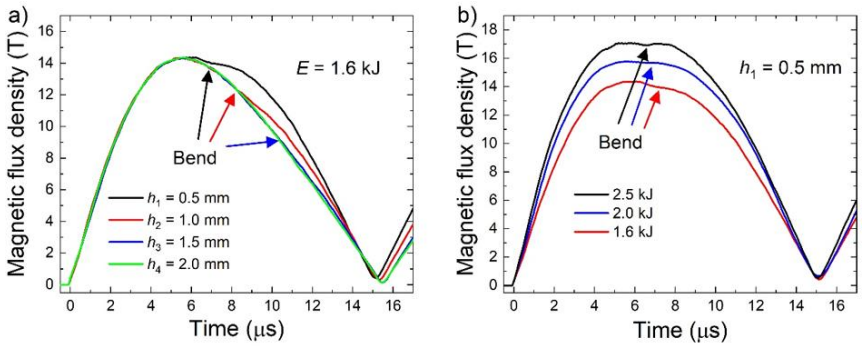


Fig. 3.3.7 First peak of the damped magnetic flux density oscillation measured in the gap between the field shaper and the deforming aluminium tube. (a) Curves for standoff distances h = 0.5, 1.0, 1.5 and 2.0 mm at a discharge energy of 1.6 kJ. (b) Curves for a standoff distance h_1 = 0.5 mm at discharge energies of 1.6 kJ (red), 2.0 kJ (blue) and 2.5 kJ (black).

3.3.3 Analysis of Experimental Results

All results obtained from magnetic field measurements in the gap between the field shaper and the flyer tube provide insight into the interaction of the flyer with parent during MPW. These results enable identification of the deformation onset and the collision time. To enhance identification of the deformation onset and the collision time, the time derivative of the magnetic flux density, dB/dt, was determined.

To ensure consistency and improve the interpretability of the measurements, the magnetic flux density data obtained from each experiment are plotted on Fig. 3.3.8 (thick lines). The derivative curves of these magnetic field are also presented in this figure (Fig. 3.3.8, thin lines). Characteristic points corresponding to deformation and collision stages were identified in the derivative curve.

Point A**,** at 2.4 μs, is the instant at which the derivative measured for the deforming flyer tube (Fig. 3.3.8, red thin line) begins to deviate from that

measured for the solid aluminium rod (black thin line). It marks the onset of flyer tube deformation under the magnetic pressure. The onset occurs at the same instant for both standoff distances h_1 = 0.5 mm and h_2 = 1 mm, since the flyer tube geometry and the discharge energy were the same in both experiments and the parent has no influence before the flyer reaches it.

Point B at 5.4 μs, identified from the derivative of the magnetic flux density, marks the instant at which the magnetic field curves for standoff distances of h_1 = 0.5 mm and h_2 = 1 mm begin to exhibit different rates of change of magnetic field (see Fig. 3.3.8, red and blue dashed curves, respectively). This transition point marking the onset of collision of flyer with the parent when standoff distance h_1.

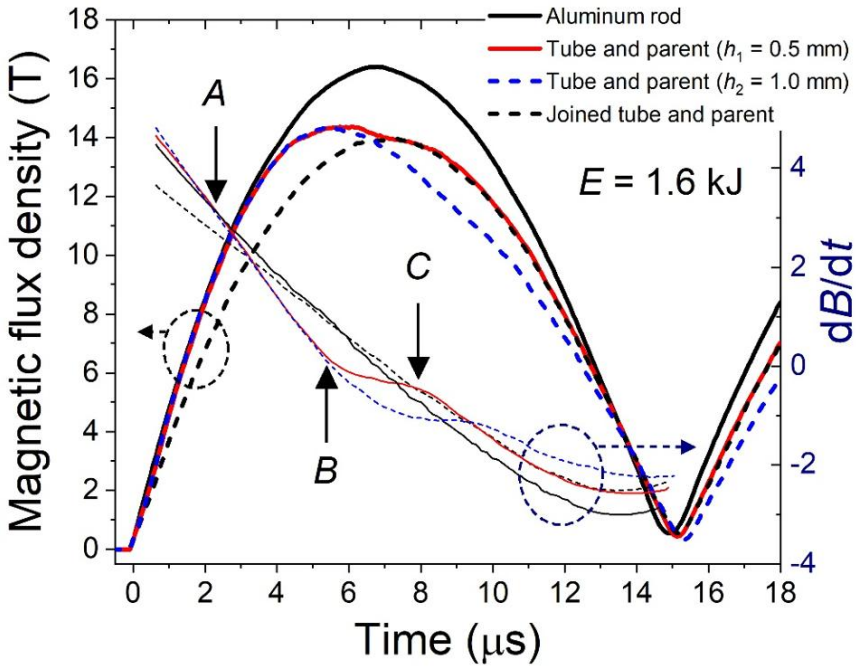


Fig. 3.3.8 Magnetic flux density $B(t)$ (thick lines, left axis) measured in the gap between the field shaper and the workpiece, and its numerically calculated time derivative dB/dt (thin lines, right axis), shown for the first peak of the damped oscillation under four conditions: a non-deformable aluminium rod inserted into the field shaper (black); welding of an aluminium tube to a stationary steel parent of 17 mm diameter, corresponding to a standoff distance h_1 = 0.5 mm (red); a repeated discharge on the assembly already welded to this parent (black dashed); and welding to a stationary steel parent of 16 mm diameter, h_2 = 1.0 mm (blue dashed). Points A, B and C on the red curve mark the features attributed to the onset of plastic deformation of the tube (A), and to the beginning (B) and the end (C) of its collision with the stationary parent. The discharge energy is 1.6 kJ.

For h_1 = 0.5 mm, the flyer tube reaches the parent and initiates collision, leading to a rapid change in magnetic flux density dynamics. As a result, the rate of change of the magnetic field (dB/dt) decreases, indicating deceleration of the flyer tube.

In contrast, for h_2 = 1.0 mm, the tube has not yet reached the parent at this time and continues its inward radial acceleration under magnetic pressure. Consequently, the magnetic field dynamics remain governed by the ongoing deformation process, without the abrupt changes associated with collision.

Point C, at 8 μs, marks the end of the collision between the flyer tube and the parent with a diameter of 17 mm (h_1 = 0.5 mm). Beyond point C, the curve coincides with the one measured on the already joined the tube and parent when h_1 = 0.5 mm (see Fig. 3.3.8, black dashed curves), indicating that the flyer tube and the parent behave as a single welded assembly with non-deformable geometry. The interval between points B and C defines the duration of the collision of the flyer tube with the parent. The collision is not instantaneous: the radial deformation of the flyer and its oblique collision with the parent proceed together, and the collision point travels along the joint.

For a parent cylinder of 16 mm diameter (h_2 = 1 mm) both points shift to later times, 7 μs and 9.8 μs. The onset and end times determined in this way for all standoff distances and discharge energies are given in Table 3.3.1. For the largest standoff distance, h_4 = 2.0 mm, the onset could not be determined, since the collision then occurs on the steeply falling part of the first peak, where the amplitude of the feature relative to the underlying waveform is too small to locate its beginning. The impact times calculated with the numerical model are included in Table 3.3.1 for comparison and are discussed in subsection 3.3.4.

Table 3.3.1 Times of the beginning T_{ONSET} and the end T_{END} of the tube–rod collision, determined from the features of the measured *B(t)* and *dB/dt* curves, and the impact time T_{IMP} obtained from the COMSOL Multiphysics simulation. The column δ gives the relative discrepancy between the simulated and the measured values of the time: $\delta = (T_{IMP} - T_{ONSET}) / T_{ONSET} \times 100$ %. Negative δ meaning that the simulated impact occurs earlier than the measured one.

	1.6 kJ				2.0 kJ				2.5 kJ			
	Experiment		Model		Experiment		Model		Experiment		Model	
h, mm	T_{ONSET}, μs	T_{END}, μs	T_{IMP}, μs	δ, %	T_{ONSET}, μs	T_{END}, μs	T_{IMP}, μs	δ, %	T_{ONSET}, μs	T_{END}, μs	T_{IMP}, μs	δ, %
0.5	**5.4**	8	**5.6**	3.7	**5.1**	7.6	**5.2**	2.0	**4.9**	7.4	**4.9**	0
1.0	**7**	9.8	**7**	0	**6.5**	9.4	**6.5**	0	**6.0**	8.9	**6.2**	3
1.5	**8.7**	11.3	**8.3**	-4.6	**8.0**	10.8	**7.6**	-5.0	**7.1**	10.3	**7.1**	0
2.0		12.6	**9.3**			11.3	**8.5**			10.8	**7.6**	

3.3.4 Coupled Electromagnetic–Mechanical Modelling of MPW Process

The numerical model described in Section 2.7 was used to calculate the deformation and the collision of the flyer tube under different welding conditions, in particular the evolution of the magnetic flux density in the gap between the field shaper and the aluminium flyer tube and the resulting radial velocity of the tube. The calculations were carried out for the three discharge energies used in the experiments: 1.6, 2.0 and 2.5 kJ.

The geometry of the numerical model reproduces the experimental configuration, in which the diameter of aluminium tube was 19 mm, its wall thickness 0.5 mm, the diameter of parent was varied (14, 15, 16, and 17 mm), resulting in corresponding changes in the standoff distance *h* (Fig. 3.3.9 (a)). The magnetic flux density was evaluated at the probe location in the air gap between the wall of flyer tube and the field shaper (see Fig. 3.3.9 (a), probe location). The radial velocity was evaluated at the point on the outer surface of the flyer tube closest to the probe position (see Fig. 3.3.9 (a), velocity measurement point).

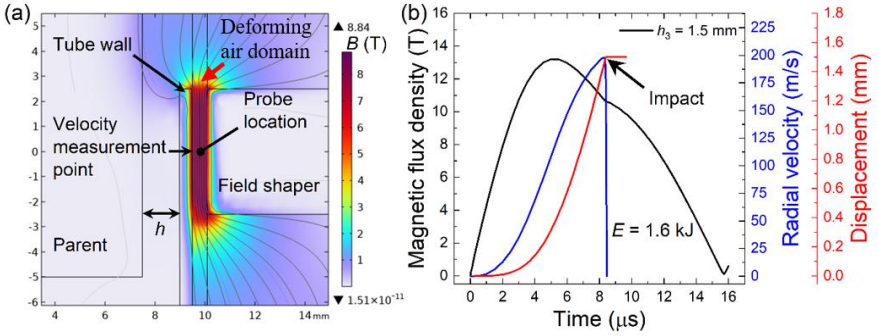


Fig. 3.3.9 (a) Geometry of the 2D COMSOL Multiphysics model of the MPW process, comprising the field shaper, the aluminium flyer tube and the stationary steel parent. The air gap between the field shaper and the flyer is modelled as a deforming domain (Moving Mesh), so that the electromagnetic and mechanical problems are two-way coupled. The point at which the magnetic flux density is evaluated lies at the mid-plane of the air gap and corresponds to the probe position in the experiment; the radial velocity and displacement are evaluated at a point on the outer surface of the flyer tube. (b) Calculated magnetic flux density versus time at the probe position (black curve, left axis), and radial velocity (blue curve) and radial displacement (red curve) of the flyer surface versus time, both on the right-hand axes. The discharge energy is 1.6 kJ and the standoff distance h_3 = 1.5 mm.

The black curve in Fig. 3.3.9 (b) is the first half-period of the calculated magnetic flux density in the gap during the tube deformation when standoff distance of h_3 = 1.5 mm and discharge energy of 1.6 kJ. As in the experimental measurements obtained by using the CMR B-scalar probe, the first half-wave

of the magnetic field exhibits a distinct bend which in the calculation occurs at 8.3 μs.

To establish its origin, a nodal point on the outer surface of the flyer tube was selected, and the temporal evolution of the radial velocity and *x*-axis displacement at this location was analyzed. As shown in Fig. 3.3.9 (b, blue curve), during the initial stage, the radial velocity increases slowly because of the relatively low magnetic pressure (proportional to B^2), while the tube response remains predominantly elastic. After several microseconds, as the magnetic pressure increases and exceeds the elastic limit, the radial velocity rises more rapidly, which corresponding to the onset of plastic deformation. The magnetic flux density reaches its maximum of 13.2 T at 5.2 μs, which is about 8% below the measured peak value of 14.4 T at the same discharge energy, and then decreases, but the flyer continues to accelerate and reaches a maximum radial velocity of 198 m/s at 8.3 μs, at which instant it drops to zero on impact with the parent cylinder (black arrow in Fig. 3.3.9 (b)). The bend in the calculated magnetic flux density curve coincides with time instant of impact.

Thus, the characteristic time to impact and maximum velocity reached before impact of the flyer tube were determined for different standoff distances and discharge energies. Fig. 3.3.10 (a) shows the calculated radial velocity of the flyer tube for different standoff distances *h* and for free deformation without the collision (see Fig. 3.3.10 (a), orange dashed curve) at the discharge energy of 1.6 kJ. At the same discharge energy, increasing the standoff distance leads to an increase in time to impact. For a standoff distance of 2 mm, the radial velocity of the flyer tube at the moment of impact

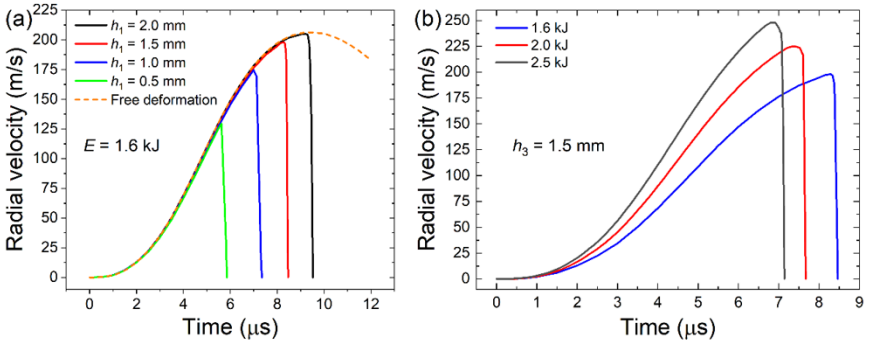


Fig. 3.3.10 Radial velocity of the flyer tube versus time, calculated with COMSOL Multiphysics at the evaluation point on the outer tube surface defined in Fig. 3.3.9. (a) Curves for standoff distances h = 0.5, 1.0, 1.5 and 2.0 mm at a discharge energy of 1.6 kJ. (b) Curves for a fixed standoff distance h_3 = 1.5 mm at discharge energies of 1.6, 2.0 and 2.5 kJ. Each curve ends at the calculated instant of impact, so its final value is the impact velocity.

(204 m/s) is close to the maximum attainable velocity (206 m/s) observed for free deformation under the same simulation conditions.

Fig. 3.3.10 (b) shows the radial tube velocity for a fixed standoff distance of h_3 = 1.5 mm at three discharge energies. A higher discharge energy gives a higher impact velocity, while the time required for the flyer tube to reach the parent decreases. Table 3.3.2 summarises the maximum impact velocities obtained from the simulations for different standoff distances and discharge energies.

The calculated instants of impact are compared with the experimental results in Table 3.3.1 (subsection 3.3.3). The model yields a single instant of impact, and this instant agrees with the experimentally determined onset of the transition rather than with its end: at 1.6 kJ the calculated values are 5.6, 7.0 and 8.3 μs against the measured onsets of 5.4, 7.0 and 8.7 μs for h_1 to h_3, that is, within 0.4 μs. This correspondence follows from the formulation of the model: since the model is axisymmetric, the flyer meets the parent simultaneously over the whole overlap and the impact is a single event, whereas in the experiment the collision is oblique, the collision point travels along the joint, and the transition has a finite duration. The comparison therefore supports the identification of point B with the first contact between the flyer and the parent, and of the interval between points B and C with the duration of the local collision.

Table 3.3.2 Radial velocity of the flyer tube at the instant of impact with the stationary steel parent, calculated with COMSOL Multiphysics at the evaluation point defined in Fig. 3.3.9.

	1.6 kJ	2 kJ	2.5 kJ
h_1 = 0.5 mm	129 m/s	141 m/s	147 m/s
h_2 = 1.0 mm	174 m/s	196 m/s	226 m/s
h_3 = 1.5 mm	198 m/s	225 m/s	248 m/s
h_4 = 2.0 mm	204 m/s	240 m/s	267 m/s

3.3.5 Tensile Testing of the Welded Joints

Tensile tests were carried out on a TIRA 2300 testing machine to determine the strength of the magnetic pulse welded joints between the aluminium flyer tubes and the stainless-steel parent cylinders. Each specimen was loaded monotonically until separation, which gives the maximum tensile load sustained by the joint. Fig. 3.3.11 (a) shows the load–displacement curves for four specimens with parent diameters of 17, 16, 15 and 14 mm (h = 0.5, 1, 1.5, 2 mm), welded at a discharge energy of 2.0 kJ.

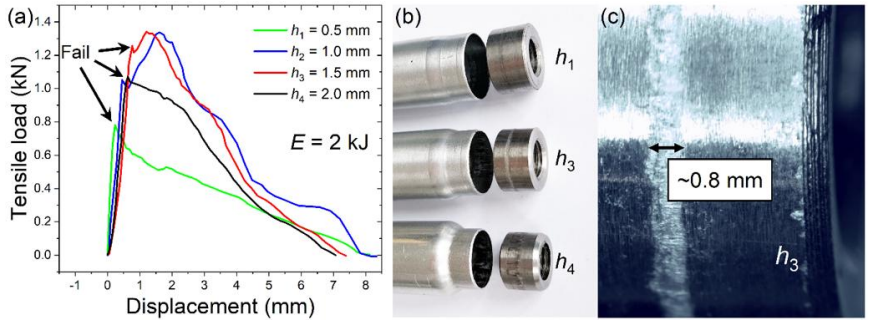


Fig. 3.3.11 (a) Tensile load versus crosshead displacement for four specimens welded at a discharge energy of 2.0 kJ with standoff distances h_1, h_2, h_3, and h_4. (b) Aluminium flyer tube and stationary steel parent after tensile testing, showing the typical appearance of the separated surfaces for h_1, h_3, and h_4. Residual aluminium remains on the steel surface, indicating that separation occurred within the aluminium rather than along the aluminium–steel interface. (c) Surface of the steel parent after separation for the specimen welded at 2.0 kJ with h_3 = 1.5 mm, showing a distinct weld seam and a bonded zone of 0.8 mm width.

As the load is applied the specimen deforms first elastically and then plastically, and the load rises with displacement up to a pronounced peak (arrows in Fig. 3.3.11 (a)) which marks the onset of failure of the joint. Beyond this point the aluminium tube separates from the steel parent and the load drops sharply. Some curves then decrease continuously, while others show a slight temporary rise, attributed to friction between the contacting surfaces, before decreasing further.

At a given discharge energy the maximum load depends on the standoff distance. At 2.0 kJ it is 0.781 kN for h_1 = 0.5 mm and 1.257 kN for h_3 = 1.5 mm, which corresponds to the higher calculated radial velocity of the flyer before the collision (Table 3.3.2, Section 3.3.4). The specimen welded at h_4 = 2.0 mm, however, fails at a lower load of 1.071 kN, although the calculated velocity before the collision is the highest of the series.

Images of the specimens after separation are shown in Fig. 3.3.11 (b) for three parent diameters welded at 2.0 kJ. The failure mode changes with the standoff distance. For h_1 = 0.5 mm the specimen fails by detachment of the two partners in the joining zone, that is, by adhesive failure: only thin discontinuous traces of aluminium remain on the surface of the steel parent, which indicates weak bonding and is consistent with the low calculated velocity before the collision. At h_3 = 1.5 mm the failure occurs within the aluminium, that is, cohesive failure: the weld is wider (Fig. 3.3.11 (c)) and a larger amount of aluminium remains on the parent surface, consistent with the higher tensile load. The failure mode is used as a criterion of weld quality in MPW, cohesive failure indicating a joint stronger than the weaker of the two

partners, which here is the aluminium, being both the weaker and the thinner of the two [108].

For h_4 = 2.0 mm the wall of the aluminium tube did not remain smooth during the compression: it buckled into longitudinal folds running along the tube axis, so that the cross-section became multi-lobed, and these folds left imprints on the surface of the steel parent (Fig. 3.3.11 (b), sample h_4). The imprints are marks of the folded tube wall, the flyer meets the parent only along the inward lobes, so that the contact is discontinuous around the circumference and the conditions required for bonding are satisfied over a smaller part of the joint. This accounts for the lower load required to separate the joint despite the highest calculated velocity before the collision. The calculated velocity is therefore not the only factor governing the strength of the joint. The collision angle is determined by the shape of the deformed flyer at the instant of contact, and a larger standoff distance allows the tube wall to bend further before it reaches the parent, so that both the impact velocity and the collision angle increase. These local collision parameters cannot be set separately and are controlled together through the discharge energy, the initial gap and the position of the workpiece [108]. Yu et al. [113] and Raoelison et al. [60] showed that excessively large collision angles promote the formation of micro-cracks and apertures in the welding zone.

The maximum loads measured for all discharge energies and standoff distances are given in Table 3.3.3. The highest load, 1.618 kN, was obtained at h_3 = 1.5 mm and 2.5 kJ, and at every discharge energy the maximum occurs at h_3 = 1.5 mm.

The specimen welded under these conditions was examined by optical microscopy after the tensile test. The surface of the steel parent carries a continuous layer of adhered aluminium 1.1 mm wide (Fig. 3.3.12). The width of the adhered layer therefore provides a second indication of the quality of the joint. It also shows that only part of the available overlap is bonded: the layer is 1.1 mm wide against the 5 mm length of the inner step of the field shaper that defines the welding zone.

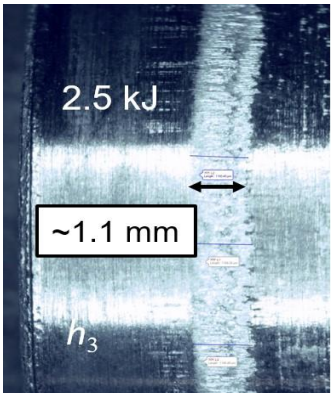


Fig. 3.3.12 Optical micrograph of the surface of the steel parent cylinder after the tensile test, for a joint welded at a h_3 = 1.5 mm and 2.5 kJ.

This may be explained by the bonding conditions required for successful joint formation. Although larger standoff distances increase the velocity prior to collision, they may

simultaneously generate less favourable collision conditions. In particular, the collision angle can deviate from the optimal range required for efficient jetting and subsequent metallurgical bonding. Furthermore, the greater radial displacement of the flyer tube results in more pronounced plastic deformation and geometric distortion, which may adversely influence local contact conditions and the stability of the bonded interface.

Table 3.3.3 Maximum tensile load sustained by the joints between the aluminium flyer tube and the stationary steel rod, measured in axial tensile tests at standoff distances h = 0.5, 1.0, 1.5 and 2.0 mm and discharge energies of 1.6, 2.0 and 2.5 kJ.

	1.6 kJ	2 kJ	2.5 kJ
h_1 = 0.5 mm	0.787 kN	0.781 kN	0.731 kN
h_2 = 1.0 mm	0.908 kN	1.052 kN	1.064 kN
h_3 = 1.5 mm	1.164 kN	1.257 kN	1.618 kN
h_4 = 2.0 mm	0.924 kN	1.071 kN	1.208 kN

The width of the adhered aluminium layer therefore provides a further criterion for assessing the weld, complementary to the failure mode. Taken together, the measurements indicate an optimum standoff distance, which for the present configuration is 1.5 mm at all three discharge energies investigated.

3.3.6 Conclusions of Section 3.3

The non-invasive investigation of the magnetic field dynamics in the gap between the field shaper and the flyer tube showed that the transient magnetic field carries information about the mechanical state of the flyer during MPW. The measured magnetic flux density waveforms provide information about the interaction between the magnetic field and the mechanical response of the flyer tube.

The discharge current measurements confirmed that the insertion of a conductive workpiece changes the electrical parameters of the coil–field shaper–workpiece system, the oscillation period decreasing and the first current maximum increasing, which is consistent with a reduction of the total inductance caused by the eddy currents induced in the workpiece.

The magnetic field measurements revealed that the presence of a conductive workpiece strongly affects the magnetic field distribution in the gap. The peak flux density increased from 9.4 to 16.5 T, that is, by a factor of 1.8, when an aluminium rod was inserted into the field shaper, the field of the eddy currents induced in the rod adding to that of the field shaper in the gap between them. When an aluminium tube was used, the measured magnetic field dynamics differed from the rigid-rod case, because the deformation of the tube changed the gap geometry and the electromagnetic conditions during the pulse itself.

Analysis of the magnetic flux density waveform and of its derivative enabled the identification of characteristic stages of the welding process: the onset of deformation of the flyer, and the beginning and the end of collision with the parent. The collision is observed not as a single instant but as a transition of finite duration, which is consistent with the oblique and progressive character of the impact between two cylindrical surfaces and with the finite size of the sensing area of the probe.

The numerical model built in COMSOL Multiphysics was constrained by the experimental data in two distinct ways, which should be distinguished. The measured discharge current was imposed as the source term of the model, so that the calculated and the measured quantities refer to the same discharge energy. The magnetic flux density in the gap is a computed output of the model, and its comparison with the sensor measurement is therefore an independent verification.

Reproducing the measured waveform required the gap between the flyer and the field shaper to be treated as a deforming domain. A Moving Mesh formulation was introduced, in which the mesh of the gap follows the radial displacement of the flyer surface computed in the mechanical part of the

model, so that the electromagnetic problem is solved at each instant on the current, deformed geometry. Only with this formulation is the coupling between the two physics complete in both directions: the magnetic pressure accelerates the flyer, and the resulting change of the gap geometry acts back on the distribution of the magnetic field in the gap. With the Moving Mesh formulation, the calculated waveform reproduces the bend observed experimentally at the moment at which the flyer reaches the parent.

The comparison with the experiment was made on two quantities. The first is the flux density waveform itself: the model reproduces the characteristic changes of the waveform observed experimentally and the instants at which they occur, the calculated peak value being about 8% below the measured one. The second is the instant of impact of the flyer on the parent, determined experimentally from the transition in the measured waveform and independently from the displacement of the flyer in the model; the two sets of values agree to within ±0.4 μs over the range of standoff distances and discharge energies investigated (Table 3.3.1). Agreement on two independent quantities is what permits the model to be used for a third that is not accessible to direct measurement in the present configuration, namely the radial velocity of the flyer immediately before impact (Table 3.3.2).

Tensile testing of the welded joints showed that the load-bearing capacity of the joint is not determined by the calculated impact velocity alone. The highest load, 1.618 kN, was obtained at a standoff distance of 1.5 mm, and at each of the three discharge energies the maximum occurs at this standoff distance, although the calculated velocity before impact is highest at a standoff distance of 2.0 mm. A sufficient impact velocity is therefore a necessary but not a sufficient condition for a strong joint: at the largest standoff distance the flyer deforms excessively before contact, its wall buckles into longitudinal folds, and the contact with the parent becomes discontinuous around the circumference.

Taken together, the results show that direct measurement of the magnetic field dynamics in the narrow gap between the field shaper and the flyer, combined with a fully coupled electromagnetic–mechanical model in which the gap is treated as a deforming domain, allows the coupled phenomena occurring during magnetic pulse welding to be followed in time and related to the quality of the resulting joint.

3.4 Magnetic Proximity Sensing in the MPW Setup Using a CMR B-Scalar Sensor

The measurements presented in Section 3.3 showed that the magnetic flux density in the gap between the field shaper and the flyer tube depends on the width of that gap, and that the change of the gap width during the pulse is reflected in the measured waveform. The same dependence can be used in the reverse direction: if the relation between the flux density and the gap width is known, a measurement of the flux density determines the position of the flyer surface. This section examines the use of a CMR B-scalar probe as a distance-dependent diagnostic of the flyer tube position in the welded assembly.

Two approaches are considered. In the first, a static bias magnetic field is produced near the sensor by a permanent magnet, and the presence of a conductive target alters the field at the sensor position; this arrangement constitutes a self-contained proximity probe, independent of the MPW discharge, and is used here to establish that a CMR B-scalar sensor is capable of proximity sensing at all. In the second, the pulsed magnetic field generated in the MPW setup itself serves as the excitation, and the probe placed at the surface of the field shaper acts as the detector, so that the position of the flyer is obtained from the same measurement that records the dynamics of the process.

3.4.1 Principle and Configuration of CMR-Based Proximity Probe

The operation of a magnetic proximity probe is based on the interaction between a nearby metallic target and an excitation magnetic field, which may be produced either by a permanent magnet or by an AC-excited coil.

To investigate the first approach, a CMR-based magnetic proximity probe (MPP) was developed for studying the dynamics of conductive objects moving in a static magnetic field. The MPP consisted of a two-terminal CMR B-scalar sensor and commercial N35-grade neodymium permanent magnets. The sensing element was fabricated from $La_{0.8}Sr_{0.2}Mn_{1.15}O_3$ thin film deposited on a polycrystalline Al_2O_3 substrate. The active area of the sensor was rectangular, 50 μm long and 500 μm wide.This probe is distinct from the one used for the measurements inside the field shaper, whose active area is 20×400 μm² (Section 2.6); the smaller area was required there to reduce the sensor resistance and to fit the probe into a gap of 0.6 mm, whereas the present measurements are made in an open configuration and do not impose these constraints.

The magnetoresistive characteristic of the CMR B-scalar sensor are presented in Fig. 3.4.1. Due to the negative CMR effect, the resistance of the sensor decreases with increasing magnetic flux density. The decrease is nonlinear, so that the sensitivity is not constant over the entire magnetic field range. The sensitivity S is defined as:

$$S(B) = \frac{1}{R(0)}\left|\frac{dR(B)}{dB}\right|, \tag{3.4.1}$$

where $R(B)$ and $R(0)$ are the resistance of the sensor at applied magnetic flux density, B and at zero magnetic field, respectively.

The sensitivity $S(B)$ depends on both the temperature and the magnetic flux density, and the proximity probe exploits this dependence. Since R(B) is an even function of B for a scalar sensor, the sensitivity vanishes at zero field, rises with increasing field to a maximum and decreases thereafter. By placing the sensor in a static bias field produced by a permanent magnet, an operating point of finite sensitivity can therefore be selected, which would not be available in the unbiased state. At room temperature the sensor used in this work exhibited a sensitivity maximum at approximately 700 mT. The operating point was chosen below this maximum, at a field where the sensitivity is 31% of its maximum value (Fig. 3.4.1).

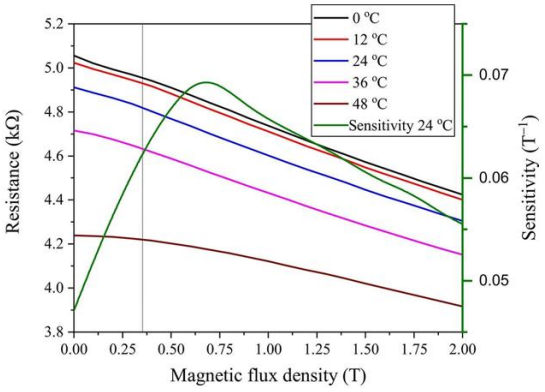


Fig. 3.4.1 Resistance of the CMR B-scalar sensing element as a function of magnetic flux density, measured at 0, 12, 24, 36 and 48 °C (left axis), and the corresponding sensitivity S calculated for the curve measured at 24 °C (right axis). The vertical line marks the bias field B_0 = 353 mT produced by the permanent magnet at the sensor position in the absence of the target, which defines the operating point of the proximity sensor.

The commercial cylindrical N35-grade neodymium permanent magnet was used as static magnetic field sources. The magnet was a solid magnetic cylinder (SMC) with an outer diameter of 15 mm and a height of 10 mm (Fig. 3.4.2 (a)).

The magnet was a solid cylinder of 15 mm outer diameter and 10 mm height (Fig. 3.4.2 (a)). The CMR B-scalar sensor was placed on the symmetry axis of the magnet at a distance of 2 mm from its surface, where the flux density was $B_0 = 353$ mT. A schematic diagram of the probe is shown in Fig. 3.4.2 (a); a photograph of the probe connected to the magnetic field meter is shown in Fig. 3.4.2 (b), the inset showing the front side of the probe.

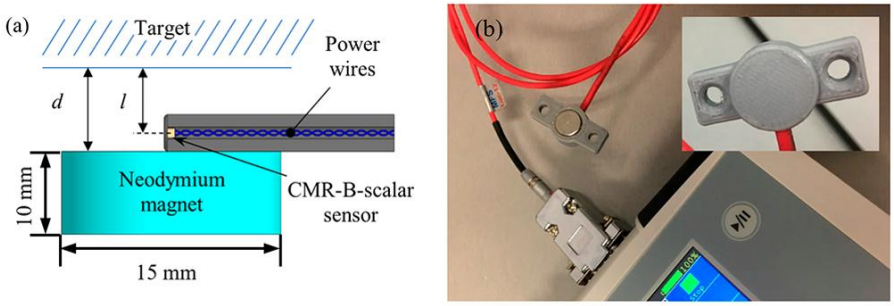


Fig. 3.4.2 Magnetic proximity probe based on a CMR B-scalar sensing element and a permanent magnet: (a) schematic cross-section of the probe with a solid cylindrical permanent magnet, where *l* is the distance from the sensing element to the target and *d* is the distance from the magnet to the target; (b) photograph of the probe connected to the magnetic field meter. The inset shows the front side of the fabricated probe.

The magnetic field magnitude was measured using the handheld magnetic field meter [91] developed at the State Research Institute Center for Physical Sciences and Technology (Lithuania) (see Fig. 2.11). This instrument is distinct from the fast measurement module described in Section 3.1 and is used here because the proximity measurements do not require microsecond time resolution. It measures flux densities from 1 mT to 10 T over a frequency range from DC to 100 kHz. The probe carries two sensing elements: the CMR B-scalar sensor and a resistive Pt1000 temperature sensor. The Pt1000 sensor monitors the probe temperature during the measurement, so that the temperature-dependent calibration can be applied correctly when the sensor response is converted into flux density. The probe was calibrated in magnetic fields from 0 to 10 T over the temperature range from 0 °C to 60 °C.

The second approach uses the same measurement configuration as in Section 3.3, the CMR B-scalar sensor being placed near the surface of the field shaper as shown in the cross-sectional view of Fig. 2.2, with photographs of the probe arrangement in Fig. 2.3. In this configuration no separate excitation source is required, the pulsed field of the field shaper serving as the excitation. During the first half-wave of the discharge the flyer tube is in motion and the recorded waveform reflects its deformation and impact, as analysed in Section 3.3. During the subsequent, more strongly damped half-waves the flyer has come to rest against the parent, so that the gap between the field

shaper and the outer surface of the welded assembly is fixed, and the flux density recorded in this interval is determined by the final position of the flyer surface. A single measurement thus yields both the dynamics of the process and the final geometry of the assembly, without a separate proximity probe or an additional measurement stage.

3.4.2 CMR-based MPP Measurements

The developed CMR-based MPP was investigated in order to establish whether a CMR B-scalar sensor can be used for proximity sensing of metallic objects. Static measurements were performed with a ferromagnetic (FM) steel plate placed at different distances from the sensing element. Dynamic measurements were carried out with rotating disks of two materials: steel, which is both ferromagnetic and conducting, and duralumin, which is conducting but not ferromagnetic. The experimental procedure is described in Section 2.3.

3.4.2.1 Proximity Measurement to a Stationary Ferromagnetic Plate

The response of the CMR-based MPP as a function of distance l to the steel plate was investigated with the magnet axis oriented perpendicular to the plate surface and directed toward the center of the plate. The plate had a relative magnetic permeability of $\mu_r = 4000$ and a remanent magnetic flux density of $B_r \approx 10$ μT.

Fig. 3.4.3 (a) shows the magnetic flux density change ΔB as a function of the distance l (see l is defined in Fig. 3.4.2 (a)) between the CMR B-scalar sensors and the FM plate (red dots). The value of sensor response ΔB increased as the FM plate was moved closer to the sensor.

The proposed MPP design has a minimum distance limit Δl between the sensor and the target plate. This limit is 4.5 mm, which includes the thickness of the CMR B-scalar probe housing and the plastic mount that holds the magnet and the sensor together.

The sensor response dependence $\Delta B(l)$ was described by the empirical expression:

$$\Delta B(l) = B(l) - B_0 = \frac{B_m}{(1 + C[l - \Delta l])^n}, \qquad (3.4.2)$$

where $B(l)$, T, is the magnetic flux density at a distance l, mm, from the target plate, B_0, T, is the magnetic flux density at the position of the CMR B-scalar sensor in the absence of the steel plate. The B_m is the fitting parameter corresponding to the maximum magnetic flux density change at the closest

possible sensor–target distance Δl. C and n are empirical constants, that depend on the magnet dimensions and the magnetic properties of the target material. The coefficients are listed in Table 3.4.1.

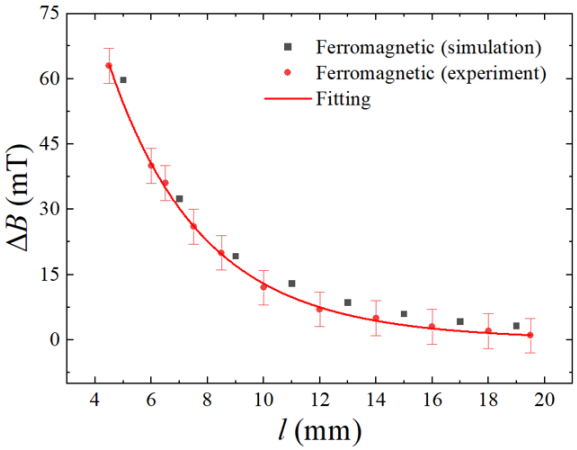


Fig. 3.4.3 Change of the magnetic flux density at the sensor, ΔB versus the distance l between the sensing element and the steel target. Red dots: measured values; black squares: values calculated with COMSOL Multiphysics. The continuous curve is a fit to the measured data and serves as the calibration relation of the proximity probe.

Table 3.4.1 Fitting coefficients of the $\Delta B(l)$ dependence according to Eq. (3.4.2).

Coefficient	Bm (mT)	C (mm-1)	n	Δl (mm)*
Steel (SMC)	*63*	0.015	20	4.5

* This parameter was selected based on experimental constraints and kept fixed during the fitting procedure.

3.4.2.2 Proximity Measurement of Rotating Ferromagnetic and Non-Ferromagnetic Disks

The response of the CMR-based MPP to the rotating steel disk is presented in Fig. 3.4.4 (a, b, c). As in the experiment with the stationary plate, the probe exhibited a positive change in the magnetic field, ΔB, as the rotating disk approached the MPP. (Fig. 3.4.4 (a)). At a rotation frequency of 30 Hz, the response pulse contained two peaks with similar amplitude at the beginning and the end of the pulse. During the time period between these peaks, the response exhibits a small symmetrical increase and decrease. An increase in disk rotating frequencies up to 40 Hz and 50 Hz led to a shortening of the response pulse duration and a change of response dynamic symmetry in the time period between the rise and fall of this pulse. The maximal value of response did not depend on plate rotation frequency.

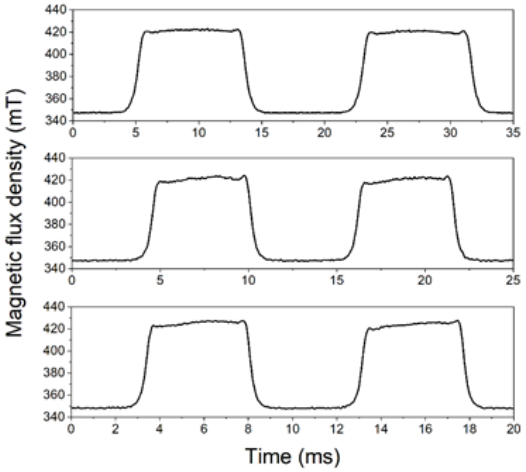


Fig. 3.4.4 Response of MPP to the ferromagnetic plate at different rotating frequencies. (a) 30 Hz, (b) 40 Hz, (c) 50 Hz.

When a cylindrical permanent magnet with its symmetry axis perpendicular to the surface of a ferromagnetic plate is brought close to the plate, the field of the magnet induces a magnetisation in the plate. The field of this magnetisation is oriented in the same direction as the field of the magnet, so that the resultant flux density at the sensor position increases.

The response to the duralumin disk, used as a moving non-ferromagnetic target, differs in three respects (Fig. 3.4.5 (a)). First, the change of flux density is negative. Second, as the rotation frequency increases the pulse becomes shorter and its magnitude increases. Third, at 30 Hz the pulse has a fast rise followed by a slow decay, and this asymmetry becomes less pronounced as the rotation frequency increases.

The different frequency dependence vs amplitude observed for steel and aluminium targets can be explained by the different response formation mechanisms. For the FM steel target, the response is governed mainly by the quasi-static redistribution of the magnetic field caused by the high magnetic permeability of the material. Therefore, the maximum response amplitude is determined primarily by the closest target–sensor distance and remains nearly independent of the rotation frequency. In contrast, the non-ferromagnetic aluminium target does not significantly distort the static magnetic field by magnetisation. Its response is mainly associated with eddy currents induced during motion through the magnetic field.

The sign of the response therefore identifies the nature of the target: a positive change of flux density corresponds to a ferromagnetic target and a negative change to a non-ferromagnetic conducting one. This distinction is obtained from a single scalar measurement, without any information on the

direction of the field, since the response of the CMR B-scalar sensor depends on the magnitude of the flux density alone and not on its direction relative to the sensor.

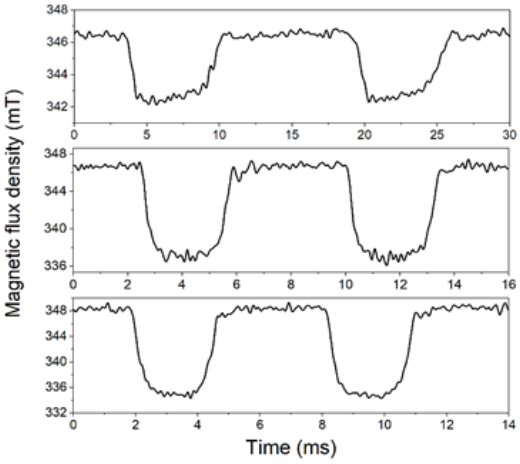


Fig. 3.4.5 Response of CMR-based MPP to the duralumin plate at different rotating frequencies. (a) 30 Hz, (b) 65 Hz, (c) 80 Hz.

3.4.3 Modelling of CMR-based MPPs

The magnet–target system was modelled in order to account quantitatively for the measured $\Delta B(l)$ dependence. The static magnetic field was calculated by the finite element method using the magnetic vector potential formulation in COMSOL Multiphysics, in a two-dimensional axisymmetric geometry. The magnet was represented as a cylinder 15 mm in diameter and 10 mm high with a remanent flux density of 1.2 T, this value having been obtained by matching a simulation of the magnet alone to field measurements made around it, and being consistent with the value expected for an N35-grade neodymium magnet. The ferromagnetic target was represented as a cylinder 120 mm in diameter and 5 mm thick, the diameter being chosen as a compromise between the size of the solution domain and the suppression of edge effects, with a relative permeability $\mu_r = 4 \times 10^3$ obtained from independent magnetisation measurements. The field distribution was calculated for a series of magnet–target distances and sampled at the position of the sensor. The calculated values are shown as squares in Fig. 3.4.3.

The calculated field distribution is shown in Fig. 3.4.6. The ferromagnetic target increases the flux density both inside itself and in the gap between itself and the magnet, which is the origin of the positive response observed experimentally.

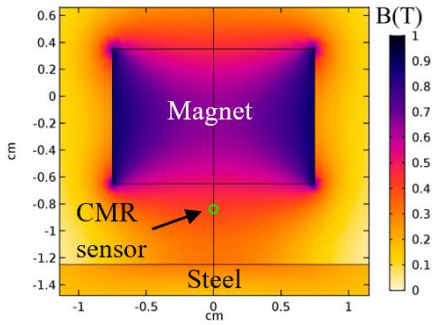


Fig. 3.4.6 Distribution of the magnetic flux density magnitude in the vicinity of the CMR-based magnetic proximity sensor with a steel target.

The behaviour of the probe near the edge of the target is important for applications in which the target does not extend over the whole sensing region. Fig. 3.4.7 shows the calculated magnitude of the flux density and its axial component as functions of the radial distance from the edge of the target, at an axial distance l = 1 mm. Away from the axis the field disturbance produced by the target acquires a substantial radial component, which a sensor responding to a single field component does not detect. At a radial distance of 2 mm the change in the magnitude of the flux density is about 25% larger than the change in its axial component alone, so that a probe based on a B-scalar sensor yields a correspondingly larger response in this region.

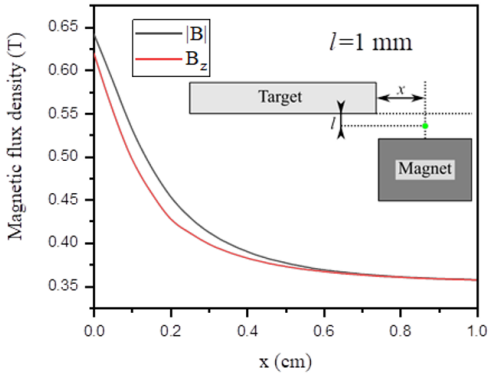


Fig. 3.4.7 Magnitude |B| and axial component B_z of the magnetic flux density calculated with COMSOL Multiphysics for the magnetic proximity probe shown in the inset, at a probe–target distance l = 1 mm. The horizontal axis is the radial coordinate x measured from the magnet axis.

The response to the rotating steel plate at 30 Hz is governed mainly by the geometry of the plate. Fig. 3.4.8 shows the results of a three-dimensional static calculation of the flux density at the sensor position, each point corresponding to a separate static solution with the plate rotated by an angle α about its axis, the magnet being placed 50 mm from the axis of rotation. The static calculation reproduces the main features of the waveform measured at 30 Hz (Fig. 3.4.4 (a)) under the assumption that the plate passes the sensor at constant velocity. This is valid if the experimentally obtained time ratio t_1/t_2 (here t_1 and t_2 are time durations during which the metal part and the air gap of the plate passes the CMR B-scalar sensor) is the same as the length ratio of these parts L_1/L_2 (see Fig. 2.7). In our case, the $L_1/L_2 \approx 1.143$ and t_1/t_2, according to Fig. 3.4.4 (a), at 30 Hz are ≈ 1.147. The ratio t_1/t_2 is closer to L_1/L_2 value, meanwhile this parameter is smaller showing that the metal part moves with lower average velocity than when the sensor if over the gap.

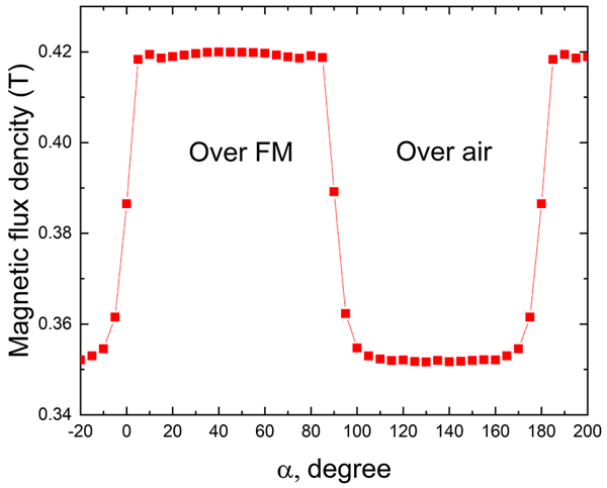


Fig. 3.4.8 Magnetostatic simulations of magnetic flux distribution over one half revolution, calculated with COMSOL Multiphysics.

The decrease in t_1/t_2 was observed for MPP at higher plate rotation frequencies. This can be explained by the interaction between the FM material and the permanent magnet. At the beginning, when the magnet approaches a steel plate, the positive acceleration is generated on this plate; however, later when magnet's center moves along L_2 distance the attraction force directed perpendicular to the plate surface and produces a radial torque. As a result, the drag force acting on the FM plate as seen by the motor increases, which in turn increases the t_2 time and decreases t_1/t_2 value. This phenomenon can be minimized by increasing the power of the electrical motor, distance between plate and the magnet or using magnet with lower magnetic field. As it was

noted in Subsection 3.4.2.2, an increase of the plate rotation frequency also changes the symmetry of response waveform.

The response to the rotating duralumin disk is caused by the currents induced in the non-ferromagnetic conductor by its motion relative to the magnet. These currents generate a secondary field opposing the change of flux, which reduces the resultant flux density at the sensor position and accounts for the negative sign of ΔB. An increase in the rotation frequency raises the rate of change of flux at the disk boundary, so that the induced currents and the magnitude of the response increase, while the interaction time, and with it the pulse duration, decreases.

3.4.4 Application of the Proximity Sensing Principle to MPW

As shown in Section 3.3, the magnetic flux density during the first half-wave is affected by the deformation of the flyer tube, and this part of the waveform identifies the onset of deformation and the instant of impact. After the impact the flyer and the parent are joined, and no further radial motion is resolved in the waveform. During the second and subsequent damped half-waves the measured field is therefore the superposition of the primary field produced by the coil and concentrated by the field shaper, and the secondary field of the eddy currents induced in the stationary flyer–parent assembly. Since this resultant field near the sensor depends on the width of the gap between the field shaper and the outer surface of the assembly, the amplitudes of the post-impact peaks carry information on the final position of the flyer surface. The second peak is the largest of these and therefore gives the best signal-to-noise ratio; its amplitude was used as the proximity indicator.

The quantity measured is the final distance d between the field shaper and the outer surface of the flyer tube, the same quantity as in the measurements with the permanent-magnet probe described in Subsections 3.4.1, the pulsed field of the field shaper now serving as the excitation in place of the magnet. The initial gap between the field shaper and the flyer is 0.6 mm, and if the wall thickness of the tube is unchanged by the compression the outer surface of the flyer moves inwards by the standoff distance h, so that $d = 0.6 + h$, (mm).

The four standoff distances investigated therefore correspond to $d_1 = 1.1$, $d_2 = 1.6$, $d_3 = 2.1$ and $d_4 = 2.6$ mm. Radial compression in fact thickens the wall slightly, so that the outer surface moves inwards by somewhat less than h and these values are upper bounds.

The second half-wave of the measured waveform was analysed for the four distances. Fig. 3.4.9 (a) shows the second half-waves measured at a discharge

energy of 2.5 kJ for d_1 to d_4. The amplitude increases as d decreases, from 12.1 T at d_4 = 2.6 mm to 15.7 T at d_1 = 1.1 mm.

Fig. 3.4.9 (b, symbols) shows the maximum amplitude of the second peak versus the final distance d for the three discharge energies 1.6, 2.0 and 2.5 kJ. The amplitude increases with decreasing d at every discharge energy, which is consistent with the dependence of the post-impact field on the final position of the flyer surface.

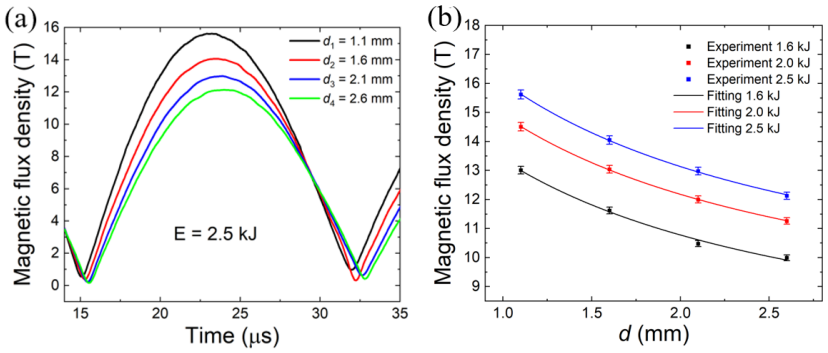


Fig. 3.4.9 (a) Second half-wave of the magnetic flux density measured at a discharge energy of 2.5 kJ for final field shaper–tube distances d_1 = 1.1, d_2 = 1.6, d_3 = 2.1 and d_4 = 2.6 mm. (b) Maximum amplitude of the second magnetic field peak as a function of the final field shaper–tube distance d for discharge energies of 1.6, 2.0 and 2.5 kJ. Symbols are the measured values, and the curves are fits according to Eq. (3.4.3) with the coefficients given in Table 3.4.2.

The measured dependence was approximated by Eq. (3.4.2), the expression used in Subsection 3.4.2.1 for the permanent-magnet proximity probe, with the distance to the target replaced by the final field shaper–flyer distance d:

$$\Delta B_2(d) = B_2(d) - B_0 = \frac{B_m}{(1 + C \cdot d)^n}, \qquad (3.4.3)$$

Here $B_2(d)$ is the measured amplitude of the second half-wave, B_0 is the amplitude that the same measurement would give with the workpiece surface removed to a large distance, B_m is the amplitude change when d = 0, and C and n are empirical constants.

In a preliminary fit in which all parameters were free, the exponent and the coefficient were obtained as $n \approx 1$ and $C \approx 1$ mm^{-1}, with no systematic variation between the three discharge energies. They were therefore fixed at n = 1 and C = 1 mm^{-1}, leaving two free parameters, B_0 and B_m, for the four measured points of each curve. The fitted values are given in Table 3.4.2 and the corresponding curves are shown in Fig. 3.4.9 (b, fitting).

Table 3.4.2 Fitting coefficients of the $\Delta B_2(d)$ dependence according to Eq. (3.4.3).

Discharge energy, kJ	B_0, T	B_m, T	RMS deviation, T
1.6	5.58	15.59	0.079
2.0	6.71	16.39	0.012
2.5	7.30	17.51	0.026

Both parameters, B_0 and B_m, increase with the discharge energy. The root-mean-square deviations of the measured points from the fitted curves, given in the last column of Table 3.4.2, lie between 0.012 and 0.079 T, which amounts to 0.05 T for all measured points taken together. The largest single deviation being 0.13 T.

The uncertainty of the measured amplitudes is governed by the anisotropy of the magnetoresistance of the manganite film and appears as a difference between the field values obtained when the field is parallel and when it is perpendicular to the film plane. For CMR B-scalar sensors of the type used in this work this contribution was characterised in [91], where the average measurement error was reported as ±6.25% at B = 0.1 T, ±3.5% at B = 0.5 T and ±2% at B = 1 T, while for fields above 1.5 T it does not exceed ±1.5%. All the amplitudes analysed here lie between 10 and 16 T, and the uncertainty of the measured amplitude was therefore taken as $\sigma_B = 0.015 \cdot B_2$, that is, 1.5% of the amplitude of the second half-wave B_2. This is the upper bound of the reported error in this field range.

The corresponding uncertainty in the determined distance follows from the slope of the calibration curve. Differentiating Eq. (3.4.3) with n = 1 and C = 1 gives:

$$\frac{\mathrm{d}B_2}{\mathrm{d}d} = \frac{-B_m}{(1+d)^2}, \tag{3.4.4}$$

So that, the uncertainty of the final flyer position, σ_d:

$$\sigma_d = \frac{\sigma_B}{\left|{}^{\mathrm{d}B_2}/_{\mathrm{d}d}\right|}, \tag{3.4.5}$$

Because the magnitude of the slope decreases with increasing d, the uncertainty in the determined position grows towards the far end of the investigated range. The calculated values are listed in Table 3.4.3.

The uncertainty ranges from 0.055 mm at d_1 = 1.1 mm to 0.125 mm at d_4 = 2.6 mm at a discharge energy of 1.6 kJ, from 0.059 to 0.134 mm at 2.0 kJ and from 0.059 to 0.135 mm at 2.5 kJ. It depends only weakly on the discharge energy but increases markedly with the field shaper–flyer distance.

Table 3.4.3 Uncertainty σ_d of the flyer position determined from the amplitude of the second field half-wave B_2. The values in brackets are σ_d/d in per cent.

d, mm	*1.6 kJ*	*2.0 kJ*	*2.5 kJ*
1.1	0.055 (5.0%)	0.059 (5.3%)	0.059 (5.4%)
1.6	0.076 (4.7%)	0.081 (5.0%)	0.081 (5.1%)
2.1	0.097 (4.7%)	0.106 (5.0%)	0.107 (5.1%)
2.6	0.125 (4.8%)	0.134 (5.1%)	0.135 (5.2%)

Expressed relative to the determined distance, the uncertainty is almost independent of both the distance and the discharge energy: σ_d/d lies between 4.7 and 5.4 % for all twelve points of Table 3.4.3 and remains below 5.5 % across the whole range from 1.1 to 2.6 mm.

These results show that a CMR B-scalar sensor placed near the field shaper provides proximity information within the same measurement that records the dynamics of the process. The amplitude of the second field peak can be used as a direct indicator of the final position of the welded tube surface relative to the fixed field shaper–sensor assembly, so that the deformation history and the final geometry of the welded joint are obtained from a single discharge, without a separate probe or an additional measurement.

3.4.5 Conclusions of Section 3.4

This section examined the use of CMR B-scalar sensors for magnetic proximity sensing of metallic objects and for determining the final position of the flyer tube in magnetic pulse welding. Two approaches were investigated. In the first, a permanent magnet produced a static bias field in which the sensor detected the perturbation caused by the presence and the motion of a conductive target. In the second, the transient field generated by the MPW setup itself served as the excitation, so that the sensor used for the measurement of the field dynamics also yielded information on the final geometry of the welded assembly.

The developed CMR-based magnetic proximity probes demonstrated a distance-dependent response to ferromagnetic targets. The change in magnetic flux density caused by a steel plate increased with decreasing probe–target distance and was described by an empirical relationship.

Measurements with rotating targets showed that the sign of the response identifies the nature of the target. For the ferromagnetic steel target the response was positive and its maximum amplitude was set by the smallest target–probe distance and was independent of the rotation frequency. For the non-ferromagnetic duralumin target the response was negative and its

amplitude increased with the rotation frequency, the currents induced by the motion of the target opposing the change of flux.

Applying the same principle to the MPW process showed that a separate displacement or position sensor is not required. The waveform recorded during a single discharge contains information both on the deformation and impact of the flyer during the first half-wave and on the final position of the welded assembly during the subsequent damped oscillations. At a discharge energy of 2.5 kJ the amplitude of the second field peak increased from 12.13 T at a final field shaper–tube distance d_4 = 2.6 mm to 15.62 T at d_1 = 1.1 mm, and the same monotonic behaviour was observed at 1.6 and 2.0 kJ.

The measured dependence was described by the empirical relation of Eq. (3.4.2) with a fixed n = 1 and C = 1 mm^{-1}. From the slope of this relation and the ±1.5% uncertainty of the magnetic flux density measurement, the final position of the flyer surface is determined with an uncertainty ranging from 0.055 mm at d_1 = 1.1 mm to 0.135 mm at d_4 = 2.6 mm, depending only weakly on the discharge energy. The amplitude of the second half-wave can therefore be used as a quantitative indicator of the final position of the flyer surface relative to the fixed field shaper–sensor assembly.

The results of this section demonstrate that CMR B-scalar magnetic-field measurements provide a multifunctional diagnostic approach for MPW. The developed method enables simultaneous investigation of transient electromagnetic processes, flyer deformation and impact dynamics, and evaluation of the final welded configuration using a single non-invasive measurement system. This approach expands the application of magnetic-field measurements from field characterisation towards process monitoring and quality assessment in high-speed electromagnetic forming and welding technologies.

GENERAL CONCLUSIONS

1. Compact CMR B-scalar probes based on $La_{0.8}Sr_{0.2}Mn_{1.15}O_3$ thin films were developed and experimentally characterised for the measurement of rapidly varying magnetic fields in high-power pulsed systems. The probes were fabricated in thin-wire and flexible printed-circuit-board configurations and calibrated in magnetic fields up to 20 T. Their compact dimensions and scalar response enable non-invasive measurements in confined regions, including field shaper–flyer gaps as narrow as 0.6 mm, where conventional magnetic-field probes are difficult to apply.
2. A dedicated measurement module was developed for the reliable acquisition of transient magnetic-field waveforms from CMR B-scalar sensors. Bipolar excitation of the probe and differential signal processing suppress parasitic electromotive forces, enabling measurement of magnetic-field pulses of about 16 μs duration and field amplitudes up to 20 T.
3. The developed CMR B-scalar measurement method enables identification of the characteristic stages of magnetic pulse welding from the magnetic-field waveform. Analysis of the field and of its time derivative allows the onset of flyer deformation and the flyer–parent impact to be identified within the first half-wave of the capacitor discharge.
4. A coupled electromagnetic–mechanical COMSOL Multiphysics model was developed for the simulation of flyer deformation and motion during magnetic pulse welding. A deforming air-gap domain between the field shaper and the flyer, with a mesh size no larger than the initial field shaper–flyer gap, was introduced to account for the continuously changing geometry during flyer motion and for its effect on the magnetic field. The model reproduces the experimentally observed flyer deformation, magnetic flux density dynamics and flyer–parent impact: the simulated impact time agrees with the measured onset of the collision to within 5 %, while the simulated peak magnetic flux density is about 8% below the measured one. The model also computes the time-dependent radial velocity of the flyer.
5. CMR B-scalar sensors provide a non-invasive means of following the magnetic pulse welding process: flyer deformation, flyer–parent impact and the final radial position of the flyer are all inferred from the measured magnetic-field waveform. Owing to the proximity-sensing mechanism, the final radial position of the flyer relative to the field shaper is

determined from the second and subsequent half-waves, within the same capacitor discharge used to characterise the deformation and impact dynamics. The uncertainty of the position determination varies from 0.06 to 0.14 mm, not exceeding 5.5 % of the determined distance, over the range of field shaper–flyer distances from 1.1 to 2.6 mm.

6. The developed magnetic-field measurement module, together with analysis of the measured field dynamics, the simulated flyer impact velocity and tensile testing of the welded joints, makes it possible to relate the welding parameters and the flyer deformation to the quality of the resulting joint. Tensile testing showed that the joint strength is not governed by the flyer impact velocity alone: it also depends on the local collision conditions and on the continuity of the bonded region.

SANTRAUKA

ĮVADAS

Didėjantis lengvų, energiją efektyviai naudojančių ir aukštos kokybės inžinerinių konstrukcijų poreikis paskatino plačiau taikyti hibridines konstrukcijas, pagamintas iš skirtingų metalų. Tokios konstrukcijos leidžia apjungti skirtingų medžiagų privalumus: padidinti mechaninį stiprumą, sumažinti konstrukcijos masę, pagerinti atsparumą korozijai ir užtikrinti geresnį elektrinį laidumą bei šilumines savybes. Todėl pažangios technologijos, leidžiančios patikimai sujungti skirtingas medžiagas, tampa vis svarbesnės automobilių, aviacijos, elektrotechnikos ir gamybos pramonėje.

Elektromagnetinių impulsų technologija (EMIT) yra didelio greičio gamybos technologija, taikoma laidžioms medžiagoms formuoti, suvirinti, užspausti ir pjauti. Skirtingai nuo įprastinių mechaninių ar lydymu pagrįstų technologijų, EMIT naudoja impulsinius magnetinius laukus, kurie sukuriami didelės srovės kondensatorių iškrovos metu, o jų kuriamos jėgos greitai deformuoja ruošinį. Magnetinio impulsinio suvirinimo (MIS) atveju taip suformuojamas kietafazis sujungimas be reikšmingo šiluminio poveikio, priešingai nei lydomojo suvirinimo atveju, kai skirtingos medžiagos turi būti išlydomos nepaisant jų skirtingų lydymosi temperatūrų.

Nepaisant EMIT technologijos pažangos, pereinamieji elektromagnetiniai procesai, lemiantys magnetinį impulsinį formavimą ir suvirinimą, vis dar ištirti nepakankamai. Šiuos procesus sudaro glaudžiai susiję elektriniai, elektromagnetiniai ir mechaniniai reiškiniai, įvykstantys per keliasdešimt mikrosekundžių. Deformacijos metu kintanti ruošinio geometrija nuolat keičia elektromagnetinę sistemos sąveiką ir taip veikia srovę, magnetinio lauko pasiskirstymą, magnetinį slėgį ir deformacijos eigą.

Baigtinių elementų metodu pagrįstas modeliavimas tapo pagrindiniu šių susietųjų reiškinių analizės įrankiu, tačiau patikimiems modeliams būtinas eksperimentinis patikrinimas. Tradiciškai EMIT procesų tyrimai daugiausia rėmėsi iškrovos srovės matavimais ir optiniais ruošinio judėjimo diagnostikos metodais. Nors šie metodai teikia vertingos informacijos, jie tiesiogiai neapibūdina impulsinio magnetinio lauko, kuris yra pagrindinis ruošinį veikiančių elektromagnetinių jėgų šaltinis.

Tiesioginis magnetinio lauko matavimas darbiniame tarpe teikia išsamesnę informaciją apie elektromagnetinės energijos perdavimą proceso metu. Tačiau tokie matavimai išlieka sudėtingi dėl didelių magnetinio lauko amplitudžių, mikrosekundinės impulsų trukmės, stiprių elektromagnetinių trikdžių ir ribotos erdvės tarp magnetinio lauko koncentratoriaus ir deformuojamo

ruošinio. Esamus matavimo metodus riboja jutiklių matmenys, kryptinis jautrumas, elektromagnetiniai trikdžiai arba būtinybė modifikuoti technologinę įrangą.

Šioje disertacijoje išvardytos problemos sprendžiamos atliekant pereinamųjų elektromagnetinių procesų eksperimentinius tyrimus magnetinio impulsinio formavimo ir suvirinimo metu. Pagrindinis dėmesys skiriamas tiesioginiams magnetinio lauko kitimo laike matavimams darbiniame tarpe naudojant miniatiūrinius CMR B-skaliariniais jutiklius ir šių matavimų rezultatų susiejimui su ruošinio deformacija, iškrovos srove bei baigtinių elementų modeliavimo rezultatais. Sukurtas susietasis elektromagnetinis–mechaninis modelis, kuriame oro tarpas tarp magnetinio lauko koncentratoriaus ir judančio ruošinio aprašomas deformuojamu tinkleliu, o modelis patikrintas lyginant jo rezultatus su išmatuotu magnetinio lauko kitimu laike ir išmatuotu smūgio momentu. Gauti rezultatai teikia naujų eksperimentinių žinių apie elektromagnetinę ir mechaninę sąveiką magnetinio impulsinio suvirinimo metu bei parodo tiesioginių magnetinio lauko matavimų reikšmę tikrinant susietuosius skaitinius modelius bei analizuojant pereinamuosius elektromagnetinius procesus.

Darbo rezultatai prisideda prie geresnio elektromagnetinių impulsų technologijų supratimo ir suteikia galimybę analizuojant eksperimentiniais bei skaitiniais metodais, optimizuoti magnetinio impulsinio formavimo ir suvirinimo procesus.

Tikslas

Pagrindinis darbo tikslas – ištirti pereinamuosius elektromagnetinius ir mechaninius reiškinius, vykstančius magnetinio impulsinio suvirinimo metu, sukuriant tiesioginių magnetinio lauko matavimų metodiką bei apjungti eksperimentinius tyrimus su susietu skaitmeniniu modeliu.

Tyrimo uždaviniai

1. Sukurti didelės amplitudės pereinamųjų magnetinių laukų matavimo metodą, skirtą elektromagnetinių impulsų technologijoms, kuris užtikrintų jutiklio laiduose indukuotos parazitinės elektrovaros jėgos eliminavimą ir jutiklio matmenis, tinkamus matavimams 0,6 mm pločio tarpe tarp magnetinio lauko koncentratoriaus ir judančio ruošinio.
2. Išmatuoti magnetinio lauko dinamiką tarpe tarp magnetinio lauko koncentratoriaus ir judančio ruošinio magnetinio impulsinio suvirinimo

metu, esant skirtingiems pradiniams atstumams tarp ruošinių bei skirtingoms iškrovos energijoms.

3. Sukurti susietąjį elektromagnetinį–mechaninį, dvimatį, ašiai simetrinį baigtinių elementų magnetinio impulsinio suvirinimo modelį, kuriame tarpas tarp magnetinio lauko koncentratoriaus ir judančio ruošinio aprašomas kaip deformuojama sritis, todėl ruošinio deformacija veikia magnetinio lauko pasiskirstymą tarpe bei patikrinti šį modelį lyginant jo rezultatus su išmatuotu magnetinio lauko kitimu laike ir išmatuotu smūgio momentu.
4. Iš išmatuoto magnetinio lauko kitimo laike ir jo išvestinės pagal laiką nustatyti būdingas proceso stadijas – judančio ruošinio deformacijos pradžią, jo judėjimą ir susidūrimą su nejudančiu ruošiniu – bei šių stadijų momentus.
5. Susieti išmatuotą magnetinio lauko dinamiką bei apskaičiuotą judančio ruošinio greitį prieš smūgį su gautos jungties stiprumu.
6. Nustatyti, ar po smūgio užregistruotas magnetinis laukas suteikia informacijos apie galutinę judančio ruošinio paviršiaus padėtį bei ar tas pats matavimas leidžia įvertinti proceso dinamiką ir galutinę suvirintos jungties geometriją.

Mokslinis naujumas

1. Sukurtas neinvazinis eksperimentinis metodas, skirtas tiesiogiai matuoti pereinamuosius magnetinius procesus magnetinio impulsinio suvirinimo sistemos darbinėje srityje. Metodas leidžia atlikti magnetinio lauko matavimus realiomis suvirinimo sąlygomis, nemodifikuojant technologinės įrangos.
2. Sukurtas susietasis elektromagnetinis–mechaninis, dvimatis, ašiai simetrinis baigtinių elementų modelis su deformuojamu oro tarpo tinkleliu, kuris seka judančio ruošinio deformaciją magnetinio impulsinio suvirinimo metu. Toks aprašymas leidžia modelyje įvertinti dinamiškai kintantį tarpą tarp magnetinio lauko koncentratoriaus ir vamzdinio ruošinio bei leidžia atkurti eksperimentiškai stebimą magnetinio lauko kitimą laike.
3. Eksperimentiškai parodyta, kad išmatuoto magnetinio lauko kitimas laike atspindi judančio ruošinio deformacijos ir jo susidūrimo su nejudančiu ruošiniu dinamiką, todėl magnetinio lauko matavimai tinka kaip naujas magnetinio impulsinio suvirinimo proceso tyrimo metodas.
4. Parodyta galimybė CMR B-skaliarinį jutiklį naudoti kaip magnetinį artumo jutiklį taikant du žadinimo būdus: nuolatinį magnetą ir suvirinimo

ritės sukuriamą impulsinį magnetinį lauką. Tai leidžia per vieną magnetinio impulsinio suvirinimo ciklą nustatyti galutinę judančio ruošinio padėtį.

Praktinė vertė

1. Valstybiniame mokslinių tyrimų institute Fizinių ir technologijos mokslų centre (FTMC) sukurta ir paleista eksperimentinė magnetinio impulsinio suvirinimo įranga. Ji leidžia tirti magnetinio impulsinio suvirinimo procesus esant didelėms impulsinėms srovėms, tuo pat metu suteikiant galimybę išbandyti magnetinio lauko matavimo sistemas bei jų jutiklius.
2. CMR B-skaliarinio jutiklio pagrindu sukurti jutikliai su plonais laidais ir ant lanksčios spausdintinės plokštės. Tokius jutiklius galima įtaisyti siaurose ir sunkiai pasiekiamose magnetinio impulsinio suvirinimo sistemos srityse, tarp jų ir 0,6 mm pločio tarpe tarp magnetinio lauko koncentratoriaus ir judančio ruošinio. Kartu su šiame darbe sukurtu matavimo moduliu jie leidžia registruoti apie 16 μs trukmės ir iki 20 T amplitudės magnetinio lauko impulsus esant elektromagnetinių impulsų technologijoms kuriamiems elektromagnetiniams triukšmams.
3. Sukurtas susietasis elektromagnetinis–mechaninis baigtinių elementų modelis, kuriame tarpas tarp magnetinio lauko koncentratoriaus ir judančio ruošinio aprašomas kaip deformuojama sritis; modelis patikrintas lyginant jo rezultatus su išmatuotu magnetinio lauko kitimu laike ir išmatuotu smūgio momentu. Modelis leidžia apskaičiuoti judančio ruošinio greitį prieš smūgį esant nustatytai iškrovos energijai ir pradiniam atstumui tarp ruošinių, todėl gali būti taikomas šiems parametrams parinkti projektuojant suvirinimo operaciją.
4. Parodyta, kad vienos iškrovos metu tarpe užregistruotas magnetinis laukas leidžia nustatyti ir proceso mechaninių įvykių momentus, ir galutinę judančio ruošinio paviršiaus padėtį po suvirinimo, todėl papildomo poslinkio ar padėties jutiklio nereikia. Toks matavimas pritaikomas pasikartojančioms suvirinimo operacijoms stebėti esamoje įrangoje, nes jutiklis užima tik tarpą, kuris joje yra ir taip.
5. FTMC sukurta CMR B-skaliarinių jutiklių technologija pritaikyta dviejose naujose srityse – elektromagnetiniame impulsiniame suvirinime ir metalinių objektų magnetiniame artumo jutime.

Ginamieji teiginiai

1. Kompaktiški CMR B-skaliariniai jutikliai, sukurti iš plonųjų $La_{0.8}Sr_{0.2}Mn_{1.15}O_3$ sluoksnių ir patalpinti ant lanksčios spausdintinės plokštės, leidžia neinvaziškai matuoti magnetinį lauką siauruose (iki 0,6 mm pločio) tarpuose tarp koncentratoriaus ir formuojamos detalės. Matavimo modulyje panaudota bipoliarinių stačiakampių impulsų generavimo metodika eliminuoja jutiklio laiduose indukuotą parazitinę elektrovaros jėgą ir tai leidžia matuoti kintamus magnetinius laukus iki 20 T, kurių impulsų trukmė siekia 16 μs.
2. Magnetinės indukcijos dinamikos matavimas tarp koncentratoriaus ir formuojamos detalės, naudojant sukurtą matavimo sistemą ir duomenų analizę, suteikia informaciją apie magnetinio impulsinio suvirinimo procesą, detalės deformacijos pradžios momentą ir tolesnę deformacijos dinamiką, deformuojamosios ir pagrindinės detalės susidūrimo momentą bei galutinę formuojamos detalės padėtį pačio proceso metu.
3. Į susietą elektromagnetinį-mechaninį COMSOL Multiphysics modelį įtraukus deformuojamo oro tarpo sritį tarp koncentratoriaus ir deformuojamos detalės, kurio tinklelio elementų dydis neviršija tarpo tarp šių elementų, galima modeliuoti geometrijos kitimą, kurį sukelia deformuojamos detalės judėjimas, taip pat dėl to atsirandančius magnetinės indukcijos kitimus laike kaip ir pačios detalės radialinį greitį. Sumodeliuotas judančios ir pagrindinės detalės susidūrimo momentas ir magnetinio srauto tankio maksimumas su eksperimentiškai išmatuotomis vertėmis sutampa atitinkamai 5 % ir 8 % tikslumu.
4. Dėl atstumu pagrįsto matavimo principo po judančios ir nejudančios detalių susidūrimo išmatuota magnetinio srauto tankio dinamika priklauso nuo galutinės judančiosios detalės radialinės padėties koncentratoriaus atžvilgiu. Šią padėtį galima nustatyti iš antrojo ir vėlesnių magnetinio lauko dinamikos pusperiodžių, esant tam pačiam kondensatoriaus iškrovimo ciklui, iš kurio pirmojo pusperiodžio metu gaunama informacija apie judančios detalės deformaciją ir smūgio dinamiką. Visame atstumo tarp koncentratoriaus ir judančios detalės kitimo intervale, padėties nustatymo neapibrėžtis neviršija 5,5 %. Todėl magnetinio lauko dinamikos matavimai kartu su sumodeliuotu judančios detalės smūgio greičiu ir tempimo bandymų rezultatais suteikia galimybę nustatyti sąryšį tarp suvirinimo proceso parametrų ir gaunamos jungties kokybės.

1. LITERATŪROS APŽVALGA

Pirmajame disertacijos skyriuje pateikta su darbo tikslu ir uždaviniais susijusios mokslinės literatūros apžvalga. Apžvelgti elektromagnetinių impulsų technologijos fizikiniai principai, pagrindinės taikymo sritys, eksperimentiniai diagnostikos metodai ir skaitinio modeliavimo galimybės, ypatingą dėmesį skiriant trumpų stiprių magnetinių laukų matavimui ir jo reikšmei magnetinio impulsinio suvirinimo procesų tyrimuose.

Literatūros analizė parodė, kad EMIT procesus lemia glaudžiai susiję elektriniai, elektromagnetiniai ir mechaniniai reiškiniai. Nors analitiniai modeliai leidžia aprašyti bendrą proceso eigą, jie dažniausiai neįvertina deformacijos metu kintančios ritės ir ruošinio geometrijos, todėl siekiant geriau suprasti šiuos procesus būtini tiesioginiai pereinamųjų elektromagnetinių reiškinių eksperimentiniai tyrimai. Taip pat nustatyta, kad ritės ir magnetinio lauko koncentratoriaus geometrija daro didelę įtaką magnetinio lauko pasiskirstymui ir magnetinio slėgio dydžiui, o dėl susidarančių magnetinio lauko netolygumų gali būti paveiktas proceso stabilumas ir suvirintos jungties kokybė.

Apžvelgus pagrindinius EMIT taikymus – elektromagnetinį formavimą, suvirinimą, užspaudimą ir pjovimą – daugiausia dėmesio skirta magnetiniam impulsiniam suvirinimui. Nustatyta, kad suvirintos jungties kokybę lemia judančio ruošinio smūgio greitis ir susidūrimo kampas, kurie tiesiogiai priklauso nuo pereinamųjų elektromagnetinių procesų ir ruošinio judėjimo dinamikos.

Išanalizavus eksperimentinius EMIT tyrimo metodus nustatyta, kad srovės matavimai teikia tik bendrą sistemos atsaką, o optiniai greičio matavimo metodai reikalauja tiesioginės optinės prieigos prie deformacijos zonos. Tiesioginiai magnetinio lauko matavimai leidžia gauti išsamesnę informaciją apie elektromagnetinės energijos perdavimą, tačiau jų taikymą riboja jutiklių matmenys, elektromagnetiniai trikdžiai ir sudėtingos įtaisymo sąlygos. Literatūroje nagrinėti indukciniai jutikliai, Holo jutikliai, optiniai skaiduliniai jutikliai ir CMR B-skaliariniai jutikliai. Palyginimas parodė, kad perspektyviausi yra CMR B-skaliariniai jutikliai, nes jų atsakas nepriklauso nuo magnetinio lauko krypties, jie pasižymi greita reakcija ir tinka stipriems magnetiniams laukams matuoti. Vis dėlto ankstesniuose darbuose jų taikymas dažniausiai buvo susijęs su technologinės įrangos modifikavimu, todėl išlieka poreikis kurti miniatiūrinius jutiklius, tinkamus matavimams siauruose darbiniuose tarpuose nekeičiant įrangos konstrukcijos.

Literatūros analizė taip pat parodė, kad EMIT procesams modeliuoti plačiai taikomas susietasis elektromagnetinis ir mechaninis modeliavimas,

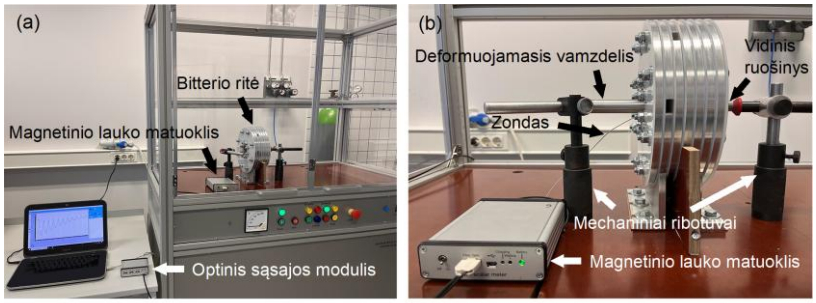
pagrįstas baigtinių elementų metodu, naudojant LS-DYNA ir COMSOL Multiphysics programinę įrangą. Tikslus modeliavimas reikalauja įvertinti dinamiškai kintantį tarpą tarp ritės ir ruošinio, o modeliams patikrinti būtini patikimi eksperimentiniai magnetinio lauko matavimai.

Apibendrinant literatūros analizę nustatyta, kad esami diagnostikos metodai teikia ribotą informaciją apie lokalų pereinamųjų magnetinių laukų kitimą, ypač siauruose darbiniuose tarpuose. Todėl metodų, leidžiančių tiesiogiai matuoti pereinamuosius magnetinius laukus nemodifikuojant technologinės įrangos, kūrimas yra svarbus siekiant geriau suprasti, modeliuoti ir optimizuoti elektromagnetinio formavimo bei magnetinio impulsinio suvirinimo procesus.

2. METODOLOGIJA

Antrajame disertacijos skyriuje aprašyti tyrimo metodai: eksperimentiniai magnetinio impulsinio suvirinimo (MIS) tyrimai, tiesioginiai pereinamųjų magnetinių laukų matavimai, skaitinis elektromagnetinių ir mechaninių procesų modeliavimas bei suformuotų jungčių mechaninių savybių vertinimas.

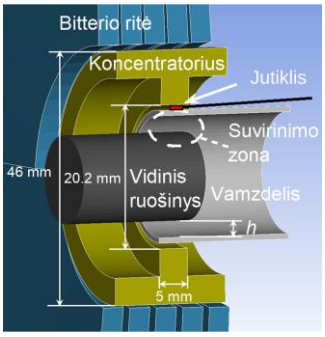
Eksperimentiniai tyrimai atlikti su specialiai sukurta magnetinio impulsinio suvirinimo įranga, kurią sudaro aukštosios įtampos maitinimo šaltinis, impulsinis kondensatorius, valdomasis kibirkštinis iškroviklis ir Bitterio ritė su magnetinio lauko koncentratoriumi (2.1a pav.). Bendras eksperimentinės darbo vietos vaizdas su Bitterio rite, magnetinio lauko matavimo sistema, aliuminio vamzdiniu (judančiu) ruošiniu ir plieniniu strypu (nejudančiu ruošiniu) pateiktas 2.1b pav. Įrangoje buvo naudojamo vamzdžio konfigūracijos ruošiniai, o magnetinio lauko matavimo sistema buvo sinchronizuota su iškrovos valdymo įranga. Tyrimuose keista iškrovos energija, pradinis atstumas tarp judančio ir nejudančio ruošinio bei ruošinių



2.1 pav. (a) Bendras eksperimentinės įrangos vaizdas. (b) Bitter ritė su sumontuotu deformuojamuoju vamzdeliu, cilindriniu vidiniu ruošiniu, mechaniniais ribotuvais ir magnetinio lauko matavimo sistema su CMR B-skaliariniu jutikliu.

geometrija, siekiant nustatyti šių parametrų įtaką magnetinio lauko kitimui laike, deformacijos eigai ir suformuotų jungčių mechaninėms savybėms. Magnetinio lauko koncentratoriaus skerspjūvis su prieš suvirinimą įtaisytais ruošiniais pateiktas 2.2 pav.

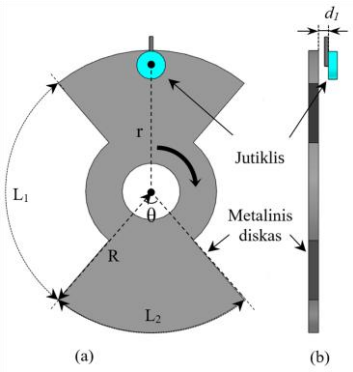
Magnetinio impulsinio suvirinimo eksperimentuose naudoti AA6063 aliuminio vamzdiniai ruošiniai ir AISI 304 nerūdijančiojo plieno cilindriniai strypai, pradinį atstumą tarp jų keičiant nuo 0,5 iki 2,0 mm.



2.2 pav. Magnetinio lauko koncentratoriaus skerspjūvis su įstatytu plieniniu vidiniu cilindriniu ruošiniu ir aliuminio deformuojamuoju vamzdeliu. CMR B-skaliarinis jutiklis įvestas į tarpą tarp magnetinio lauko koncentratoriaus ir deformuojamojo vamzdelio. Eksperimentų metu buvo keičiamas pradinis atstumas *h*.

CMR B-skaliariniu jutikliu pagrįsto magnetinio atstumo jutiklio dinaminiam atsakui tirti sukurta atskira eksperimentinė sistema su segmentuotais besisukančiais diuraliuminio ir plieno diskais. Ji leido keisti taikinio sukimosi dažnį ir atstumą iki jutiklio ir taip nustatyti šių dydžių įtaką jutiklio atsakui. Eksperimentinės sistemos schema pateikta 2.3 pav.

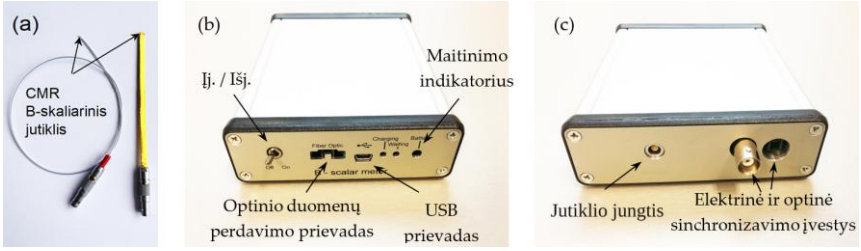
Elektromagnetinių procesų analizei iškrovos srovė matuota specialiai pagaminta Rogovskio rite, o srovės kitimo laike kreivės atkurtos skaitiniu integravimu. Keičiant kondensatoriaus įkrovos įtampą gautos 1,6–2,5 kJ iškrovos energijos, atitinkančios 76–95 kA didžiausias iškrovos sroves. Šie duomenys naudoti elektromagnetinių procesų analizei ir skaitiniam modeliui patikrinti.



2.3 pav. CMR magnetinio atstumo jutiklio dinaminių parametrų tyrimo sistemos schema: (a) bendras vaizdas iš priekio; (b) šoninis vaizdas, kai naudojamas jutiklis su vientisu nuolatiniu magnetu.

Atsižvelgiant į taikymo sritį pagaminti dviejų tipų CMR B-skaliariniai jutikliai, PI-MOCVD metodu suformuoti ant Al_2O_3 padėklų. Atstumo jutikliams pasirinkti didesnės savitosios varžos manganito sluoksniai, o pereinamųjų magnetinių laukų matavimams – mažesnės savitosios varžos sluoksniai, tinkamesni trumpiems didelės amplitudės magnetinio lauko impulsams registruoti.

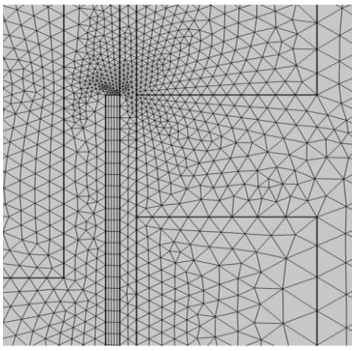
Vienas svarbiausių darbo metodinių rezultatų – plonų CMR B-skaliarinių magnetinio lauko jutiklių ir specializuotos matavimo sistemos sukūrimas. Suprojektuoti jutikliai su plonais laidais ir jutikliai ant lanksčios spausdintinės plokštės; tokios konstrukcijos leido įtaisyti jutiklius siaurame darbiniame tarpe tarp magnetinio lauko koncentratoriaus ir judančio aliuminio vamzdinio ruošinio ir tiesiogiai registruoti magnetinio srauto tankio kitimą laike magnetinio slėgio veikimo srityje. Siekiant eliminuoti jutiklio laiduose ir kontaktuose indukuotą parazitinę elektrovaros jėgą, sukurtame matavimo modulyje CMR jutiklis maitintas bipoliniais stačiakampiais įtampos impulsais, o elektronika įtaisyta ekranuojančiame korpuse. Matavimo duomenys perduoti optiniu kabeliu, taip užtikrinant galvaninį atskyrimą ir atsparumą stipriems elektromagnetiniams trikdžiams. Sukurta sistema leidžia registruoti apie 16 μs trukmės magnetinio lauko impulsus. Jutikliai buvo sukalibruoti iki 20 T, o šiuose eksperimentuose išmatuoti iki 16,5 T laukai. Magnetinio lauko jutikliai ir matavimo modulis pateikti 2.4 pav.



2.4 pav. (a) Plokščio ir apvalaus jutiklių konstrukcijos. (b) Magnetinio lauko matavimo modulis (priekinis ir nugarinis vaizdas).

Pereinamiesiems elektromagnetiniams ir mechaniniams procesams modeliuoti COMSOL Multiphysics programine įranga buvo sukurtas susietasis, dvimatis, ašiai simetrinis baigtinių elementų modelis. Oro tarpas tarp judančio vamzdinio ruošinio ir magnetinio lauko koncentratoriaus aprašytas deformuojamu tinkleliu, sekančiu ruošinio paviršiaus poslinkį, todėl elektromagnetinis uždavinys kiekvienu laiko momentu sprendžiamas esamos, deformuotos, geometrijos srityje. Taip sukuriamas grįžtamasis ryšys: magnetinis slėgis greitina ruošinį, o dėl deformacijos kintantis tarpas veikia magnetinio lauko pasiskirstymą jame. Elektromagnetinis laukas apskaičiuotas

sprendžiant Maksvelo lygtis kvazistacionariuoju artiniu, taikant magnetinio vektorinio potencialo formuluotę. Lorenco jėga taikyta kaip tūrinės apkrovos mechaniniam uždaviniui. Modelio šaltinis – eksperimentiškai išmatuota iškrovos srovė, o ruošinio medžiaga aprašyta eksperimentiškai nustatyta aliuminio įtempių–deformacijų kreive. Vamzdinio ruošinio 0,5 mm storio sienelė padalyta į penkis baigtinių elementų sluoksnius, nes esant iškrovos dažniui skvarbos gylis yra artimas sienelės storiui, ir toks skaidymas užtikrina teisingą srovės tankio pasiskirstymo sienelėje aprašymą. Skaičiavimo sritis ir baigtinių elementų tinklelis pateikti 2.5 pav.



2.5 pav. COMSOL Multiphysics skaičiavimo sritis ir baigtinių elementų tinklelis.

Mechaninėms medžiagų ir suformuotų jungčių savybėms įvertinti TIRA 2300 bandymų įrenginiu atlikti tempimo bandymai. Iš aliuminio vamzdinių ruošinių bandymų gautos įtempių–deformacijų kreivės panaudotos skaitiniame modelyje. Suvirintų jungčių kokybė vertinta pagal didžiausią tempimo jėgą, pagal tempimo pobūdį – ar veikiama sandūra tarp medžiagų, ar pats aliuminis – ir pagal tai optiniu mikroskopu nustatytas prie plieninio ruošinio prilipusio aliuminio sluoksnio plotis, kuris faktiškai parodo suvirintos srities plotį.

3. REZULTATAI IR APTARIMAS

3.1 Trumpų didelės amplitudės magnetinio lauko impulsų matavimai

Trumpi impulsiniai magnetiniai laukai, susidarantys EMIT procesuose, gali siekti kelias dešimtis teslų ir kinta per mikrosekundes. Tokiomis sąlygomis tiesioginius matavimus apsunkina parazitinė elektrovaros jėga (EVJ), indukuojama jutiklio kontaktuose ir jungiamuosiuose laiduose. Išmatuotas signalas U_{mat} susideda iš dviejų dedamųjų: naudingojo CMR jutiklio magnetovaržinio atsako U_{CMR} ir pagal Faradėjaus dėsnį indukuotos įtampos U_{EVJ}:

$$U_{mat}(t) = U_{CMR}(t) + U_{EVJ}(t)$$

Indukuotoji dedamoji priklauso nuo magnetinio srauto kitimo greičio ir kontūro, kurį sudaro jutiklio laidai, ploto. Darbe išnagrinėti keli šios dedamosios slopinimo būdai. Vienas jų – bifiliariškai susukti jutiklio laidai. Toks sprendimas sumažina indukuotą įtampą, nes priešingo poliškumo

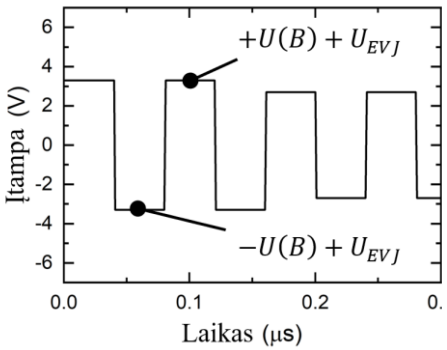
signalai iš dalies kompensuoja vienas kitą, tačiau sparčiai kintančio magnetinio lauko atveju jo visiškai nepašalina. Kitas nagrinėtas būdas pagrįstas papildomomis kompensacinėmis kilpomis, tačiau jis reikalauja tikslaus geometrinio suderinimo ir kalibravimo, o esant dideliems magnetinio lauko gradientams tai sunkiai įgyvendinama.

Šiems apribojimams įveikti pritaikytas bipolinis jutiklio maitinimo metodas: CMR jutiklis maitinamas pakaitomis teigiamo ir neigiamo poliškumo įtampos impulsais. Magnetovaržinis atsakas keičia poliškumą kartu su maitinimo įtampos kryptimi, o indukuotoji EVJ išlieka praktiškai nepakitusi, todėl atėmus dviejų iš eilės einančių teigiamo ir neigiamo maitinimo atsakus parazitinė dedamoji yra eliminuojama:

$$U(B) = \frac{\left[+U(B) + U_{EVJ}\right] - \left[-U(B) + U_{EVJ}\right]}{2}$$

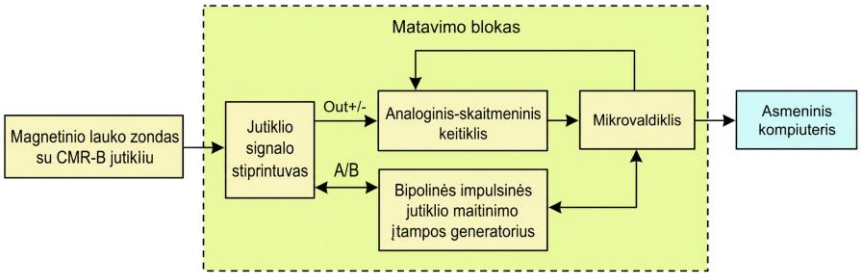
Šis metodas leidžia atskirti nuo magnetinio lauko priklausantį jutiklio atsaką nuo parazitinės dedamosios nenaudojant papildomų kompensacinių kilpų. Įtampos signalai, išmatuoti per du gretimus teigiamo ir neigiamo poliškumo jutiklio maitinimo impulsus, pateikti 3.1 pav.

Šiam EVJ slopinimo metodui įgyvendinti sukurtas specializuotas magnetinio lauko matuoklis. Jį sudaro CMR B-skaliarinis magnetinio lauko jutiklis, bipolinės impulsinės maitinimo įtampos generatorius, signalo stiprinimo grandinė, analoginis-skaitmeninis keitiklis, mikrovaldikliu pagrįsta signalų apdorojimo sistema bei USB ir optinio ryšio sąsajos. Matuoklio struktūrinė schema pateikta 3.2 pav. Optinis duomenų perdavimas užtikrina galvaninį atrišimą tarp matavimo elektronikos ir kompiuterio ir taip sumažina magnetinio impulsinio suvirinimo įrangos kibirkštinio iškroviklio keliamų elektromagnetinių trikdžių poveikį.



3.1 pav. Įtampos signalai, išmatuoti dviejų gretimų teigiamojo ir neigiamojo jutiklio maitinimo metu.

Vienas svarbiausių matavimo sistemos reikalavimų – mažos elektrinės varžos CMR jutikliai: dėl mažos jutiklio RC laiko konstantos maitinimo įtampos impulsai iškraipomi mažiau. Šiam tikslui sukurti specialūs mažos varžos CMR jutikliai. Sukurta sistema generuoja iki 12,5 MHz dažnio bipolinį

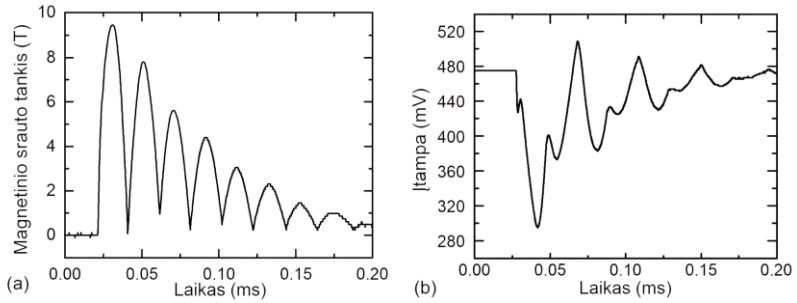


3.2 pav. Impulsinio magnetinio lauko matuoklio struktūrinė schema.

maitinimo signalą, leidžiantį slopinti parazitinę EVJ matuojant mikrosekundinės trukmės didelės amplitudės magnetinio lauko impulsus.

Sukurtas magnetinio lauko matuoklis eksperimentiškai patikrintas magnetinio impulsinio suvirinimo procesus atitinkančiomis sąlygomis. Matuoklis išbandytas magnetinio impulsinio suvirinimo įrangoje: CMR jutiklis įtaisytas magnetinio lauko koncentratoriuje, įstatytame į Bitterio ritę, per kurią iškraunamas kondensatorius. 3.3a pav. pateiktas magnetinio srauto tankio kitimas laike, gautas taikant bipolinį jutiklio maitinimą, kai parazitinė EVJ nuslopinta, o jutiklio įtampos signalas perskaičiuotas į magnetinio srauto tankį. Palyginti 3.3b pav. pateiktas jutiklio įtampos signalas, išmatuotas įprastu nuolatinės srovės maitinimu.

Eksperimentiniai rezultatai parodė, kad bipolinis jutiklio maitinimas sumažina parazitinės EVJ įtaką ir padidina matavimo sistemos atsparumą didelės impulsinės galios įrangos keliamiems elektromagnetiniams trikdžiams. Tai leido patikimai registruoti trumpus didelės amplitudės magnetinio lauko impulsus ir tiesiogiai nustatyti jų kitimą laike elektromagnetinių impulsų technologijos procesuose.

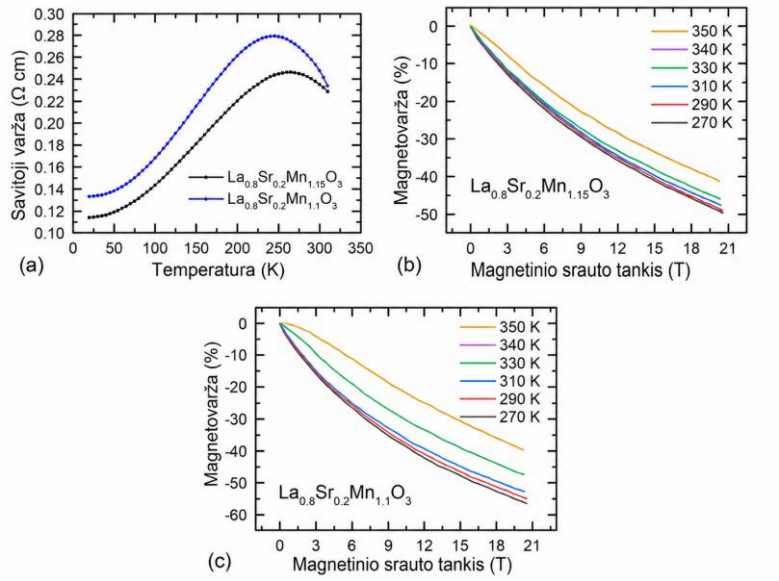


3.3 pav. (a) Magnetinio srauto tankio priklausomybė nuo laiko Bitter ritėje, išmatuota magnetinio lauko matuokliu. (b) Jutiklio įtampos signalas, išmatuotas taikant įprastą nuolatinės srovės maitinimą.

Apibendrinant šiame skyriuje gautus rezultatus, pagrindinė išspręsta problema – tiesioginis didelės amplitudės, keliolikos mikrosekundžių trukmės magnetinio lauko impulsų matavimas stiprių elektromagnetinių trikdžių aplinkoje. Sukurtą CMR B-skaliarinę magnetinio lauko matavimo sistemą sudaro specialiai suprojektuotos mažos varžos CMR struktūros, bipolinis jutiklio maitinimas, elektromagnetinių trikdžių slopinimo sprendimai, signalų apdorojimas ir kalibravimo procedūros. Sukurtas magnetinio lauko matuoklis leidžia tiesiogiai eksperimentiškai tirti pereinamuosius magnetinio lauko reiškinius magnetinio impulsinio suvirinimo sistemose, kurių netiesioginiais iškrovos srovės matavimais nustatyti negalima. Šio skyriaus rezultatai sudaro eksperimentinį pagrindą tolesnei magnetinio lauko kitimo laike analizei judančiam vamzdiniam ruošiniui deformuojantis ir elektromagnetinės bei mechaninės sąveikos modelių patikrinimui, nagrinėjamiems kituose disertacijos skyriuose.

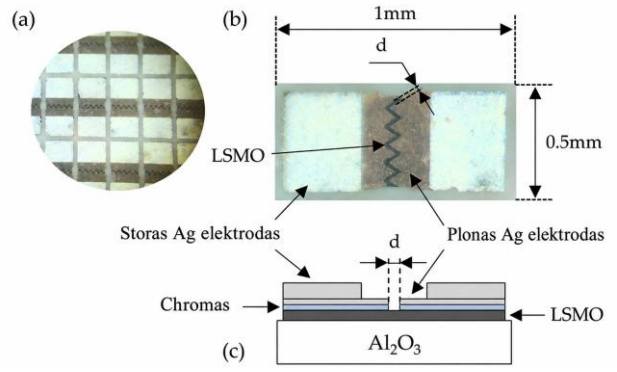
3.2 CMR B-skaliarinių magnetinio lauko jutiklių kūrimas

Siekiant sukurti miniatiūrinius magnetinio lauko jutiklius, tinkamus pereinamiesiems magnetiniams laukams matuoti magnetinio impulsinio suvirinimo įrangoje, pirmiausia optimizuota La–Sr–Mn–O plonųjų sluoksnių sudėtis. Tirti skirtingą mangano perteklių turintys $La_{0.8}Sr_{0.2}Mn_yO_3$ sluoksniai: matuota jų savitoji elektrinė varža ir magnetovarža plačiame temperatūrų intervale bei impulsiniuose magnetiniuose laukuose iki 20 T (3.4 pav.). Nustatyta, kad elektrinės ir magnetovaržinės savybės priklauso nuo mangano kiekio. Sluoksnių, kurių $y = 1{,}15$, dielektriko ir metalo virsmo temperatūra T_m yra 270 K, o savitosios varžos maksimumas ρm – 0,245 Ω·cm; sluoksnių, kurių $y = 1{,}1$, T_m sumažėja iki 240 K, o ρm padidėja iki 0,28 Ω·cm (3.4 pav. a). Kambario temperatūroje ir aukštesnėse temperatūrose didesne magnetovarža pasižymi $y = 1{,}15$ sluoksniai (3.4 pav. b, c), todėl miniatiūriniams magnetinio lauko jutikliams, veikiantiems kambario temperatūroje ir aukščiau, pasirinkta būtent tokia sudėtis. Peršviečiančio elektronų mikroskopo tyrimai parodė, kad abiejų sudėčių sluoksnių koloninių grūdelių plotis ir grūdelių ribų tankis nesiskiria, todėl elektrinių ir magnetovaržinių savybių skirtumai siejami su mangano kiekio įtaka Mn^{4+}/Mn^{3+} jonų santykiui, o ne su mikrostruktūros skirtumais.



3.4 pav. $La_{0.8}Sr_{0.2}Mn_yO_3$ sluoksnių elektrinės varžos ir magnetovaržos priklausomybės.

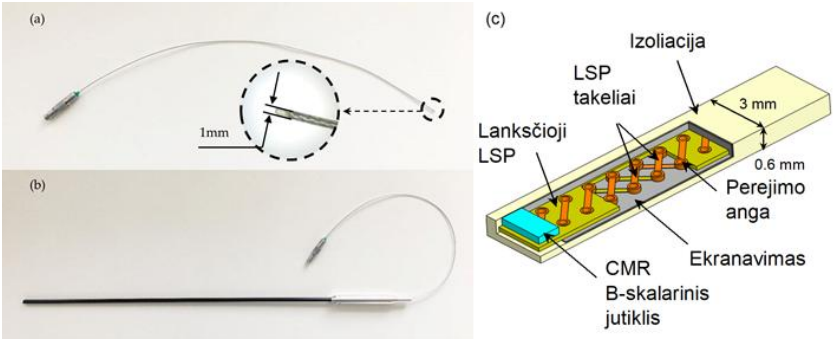
Optimizavus manganito sluoksnių sudėtį, sukurta miniatiūrinių CMR B-skaliarinių magnetinio lauko jutiklių gamybos technologija. Taikant fotolitografiją, cheminį ėsdinimą, Cr/Ag elektrinių kontaktų formavimą ir terminį atkaitinimą pagaminti 1 × 0,5 mm² dydžio jutikliai, kurių elektrinė varža apie 500 Ω. Aktyviosios jutiklio srities ilgis 400 μm, plotis 20 μm, manganito sluoksnio storis 350 nm. Jutiklio sandara ir optinis vaizdas pateikti 3.5 pav.



3.5 pav. Jutiklių vaizdas po fotolitografijos proceso (a). Vieno jutiklio vaizdas (b) ir skerspjūvio schema (c).

Pereinamųjų magnetinių laukų matavimams sukurtos dvi jutiklių konstrukcijos: jutiklis su plonais laidais ir jutiklis ant lanksčios spausdintinės plokštės. Jutiklis su plonais laidais pagamintas iš 50 μm skersmens bifiliariškai susuktų varinių laidų, įtaisytų į pintą elektromagnetinius trikdžius slopinantį ekraną ir PTFE izoliaciją, apsaugančią nuo aukštosios įtampos; visos konstrukcijos skersmuo apie 1 mm. Jutiklis ant lanksčios spausdintinės plokštės yra plonesnis – apie 0,6 mm storio, todėl būtent jis įtaisytas darbiniame tarpe tarp magnetinio lauko koncentratoriaus ir judančio ruošinio ir naudotas magnetinio impulsinio suvirinimo eksperimentuose. Abi konstrukcijos leidžia įtaisyti jutiklį siaurose magnetinio impulsinio suvirinimo įrangos vietose mažai įtakojant magnetinį lauką.

Didžiausia dėmesio skirta jutiklio ant lanksčios spausdintinės plokštės konstrukcijai. Joje CMR jutiklis tiesiogiai integruotas į lanksčios spausdintinės plokštės laidžiuosius takelius, sudarančius bifiliarinę jungtį. Jutiklio sandara ir pagrindiniai elementai pateikti 3.6 pav. Jutiklis ekranuotas aliuminio folija elektromagnetinių trikdžių poveikiui sumažinti ir elektriškai izoliuotas poliamido sluoksniu. Pagrindiniai šios konstrukcijos ypatumai – mažas storis (0,6 mm), galimybė įtaisyti jutiklį siaurame darbiniame tarpe negręžiant papildomų angų ir nekeičiant magnetinio lauko koncentratoriaus konstrukcijos, bei maža įtaka proceso elektromagnetinėms sąlygoms. Tai leidžia įtaisyti jutiklį tarpe tarp magnetinio lauko koncentratoriaus ir judančio ruošinio ir tiesiogiai matuoti magnetinio lauko kitimą laike suvirinimo zonoje nekeičiant technologinės įrangos geometrijos.



3.6. pav. Sukurtų CMR B-skaliarinių magnetinio lauko jutiklių konstrukcijos

Visi pagaminti jutikliai sukalibruoti impulsiniuose magnetiniuose laukuose iki 20 T, esant 273–333 K temperatūroms. Kalibravimui naudotas impulsinio magnetinio lauko generatorius, sukuriantis iki 20 T amplitudės ir apie 1 ms trukmės magnetinio lauko impulsus. Kalibravimo metu gautos jutiklių charakteristikos įrašytos į matuoklio atmintį ir naudojamos

išmatuotam jutiklio signalui perskaičiuoti į absoliučiąsias magnetinio srauto tankio vertes.

Matavimų rezultatų atsikartojamumui užtikrinti ir jutiklio padėties įtakai sumažinti 3D spausdinimo būdu pagamintas jutiklio pozicionavimo laikiklis. Jo sandara ir naudojimas eksperimentuose pateikti 3.8 pav. Laikiklis užtikrino tikslią ir per visus eksperimentus nekintančią jutiklio padėtį matavimo vietoje. Tai būtina, nes dėl didelių magnetinio lauko gradientų darbiniame tarpe net nedideli jutiklio padėties pokyčiai reikšmingai keičia išmatuotą magnetinio srauto tankį.

Taigi optimizavus manganito sluoksnių sudėtį sukurti miniatiūriniai CMR B-skaliariniai magnetinio lauko jutikliai, o jų pagrindu pagaminti ir sukalibruoti dviejų konstrukcijų magnetinio lauko jutikliai. Jutikliai kartu su sukurtu matuokliu sudaro eksperimentinį įrankį tiesioginiams pereinamųjų magnetinių laukų tyrimams magnetinio impulsinio suvirinimo įrangoje. Sukurtos konstrukcijos leidžia matuoti magnetinį lauką siaurose technologinės įrangos vietose nekeičiant suvirinimo įrankio konstrukcijos ir sudaro pagrindą tolesniems elektromagnetinių ir susietųjų elektromagnetinių–mechaninių procesų tyrimams, pateiktiems kituose disertacijos skyriuose.

3.3 Elektromagnetinių ir mechaninių procesų tyrimas magnetinio impulsinio suvirinimo metu

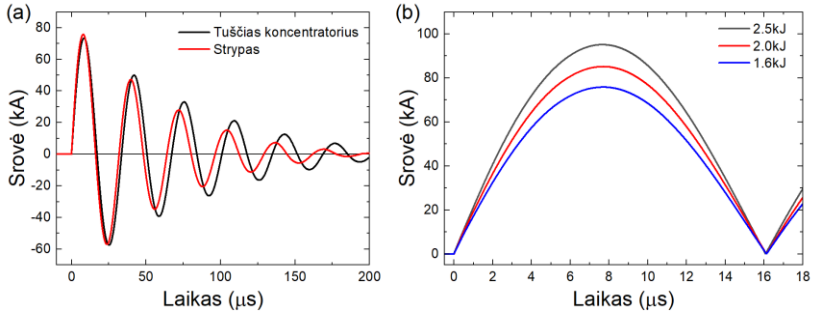
Šiame poskyryje pateikti pagrindiniai pereinamųjų elektromagnetinių procesų eksperimentiniai tyrimai magnetinio impulsinio suvirinimo (MIS) metu, atlikti sukurta CMR B-skaliarine magnetinio lauko matavimo sistema. Tyrimo tikslas – tiesiogiai nustatyti magnetinio lauko kitimą laike siaurame tarpe tarp magnetinio lauko koncentratoriaus ir judančio aliuminio vamzdinio ruošinio ir susieti išmatuotą elektromagnetinį atsaką su suvirinimo metu vykstančiais mechaniniais procesais: ruošinio deformacija, jo greitėjimu ir susidūrimu su nejudančiu ruošiniu.

Pirmiausia išanalizuotas per Bitterio ritę tekančios iškrovos srovės kitimas laike. Magnetinio lauko stipris tarpe tarp koncentratoriaus ir judančio ruošinio tiesiogiai priklauso nuo ritėje tekančios srovės, todėl tiksliai ją išmatuoti būtina ir magnetinio lauko kitimui interpretuoti bei, skaitiniam modeliavimui atlikti. Kondensatoriaus iškrovos metu per ritę tekanti srovė matuota Rogovskio rite. Išmatuotoji srovė kito slopstančiais svyravimais, kuriuos aprašo išraiška: $I(t) = I_0 e^{-\alpha t} \sin(\omega t)$ kur I_0 – srovės amplitudės pradinė vertė, α – slopinimo koeficientas, ω – svyravimų kampinis dažnis.

Eksperimentai atlikti dviem konfigūracijomis: su tuščiu magnetinio lauko koncentratoriumi ir su į jį įstatytu aliuminio strypu. Matavimai parodė (3.7a

pav.), kad laidaus ruošinio įstatymas į magnetinio lauko koncentratorių keičia ritės–koncentratoriaus–ruošinio sistemos elektrinius parametrus dėl elektromagnetinės šių elementų sąveikos. Įstačius aliuminio strypą, didžiausia iškrovos srovės amplitudė padidėjo nuo maždaug 73 kA iki 76 kA, o svyravimų periodas sumažėjo nuo 34 μs iki 32 μs. Šie pokyčiai ir padidėjęs slopinimas siejami su ritės–koncentratoriaus–ruošinio sistemos efektyviosios varžos ir induktyvumo pokyčiais, kuriuos lemia laidžiame ruošinyje indukuotos sūkurinės srovės.

Didinant Didėjant iškrovos energijai, didėjo ir didžiausia iškrovos srovė: esant 1,6; 2,0 ir 2,5 kJ energijoms, gautos atitinkamai apie 76 kA, 85 kA ir 95 kA srovės amplitudės (3.7b pav.). Išmatuotos srovės kitimo laike kreivės toliau naudotos kaip įvesties duomenys susietajame elektromagnetiniame–mechaniniame skaitiniame modelyje, taip užtikrinant, kad eksperimento ir modeliavimo rezultatai atitiktų tą pačią iškrovą.

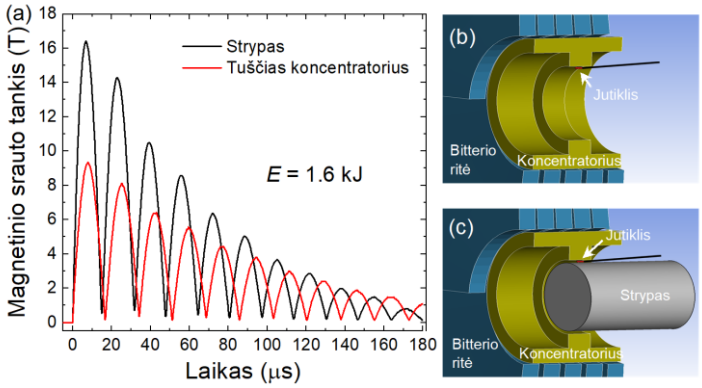


3.7 pav. (a) Iškrovos srovės kitimo formos esant 1,6 kJ energijai tuščiam lauko koncentratoriui ir su įstatytu aliuminio strypu; (b) Pirmasis absoliučiosios iškrovos srovės pusperiodis esant skirtingoms iškrovos energijoms magnetinio impulsinio suvirinimo metu.

Srovės matavimo rezultatai rodo, kad magnetinio impulsinio suvirinimo metu ruošinys yra elektromagnetiškai susietas su magnetinio lauko koncentratoriumi ir tiesiogiai veikia jį patį veikiančio magnetinio slėgio dydį.

Toliau atlikti tiesioginiai pereinamojo magnetinio lauko kitimo laike matavimai siaurame tarpe tarp magnetinio lauko koncentratoriaus ir judančio vamzdinio ruošinio sukurtais CMR B-skaliariniais jutikliais. Prieš magnetinio impulsinio suvirinimo eksperimentus atlikti parengiamieji matavimai, siekiant nustatyti magnetinio lauko kitimą esant skirtingoms įrankio konfigūracijoms. Visuose eksperimentuose magnetinio lauko jutiklis įtaisytas prie vidinės magnetinio lauko koncentratoriaus sienelės, o kondensatoriaus iškrovos energija buvo vienoda – 1,6 kJ.

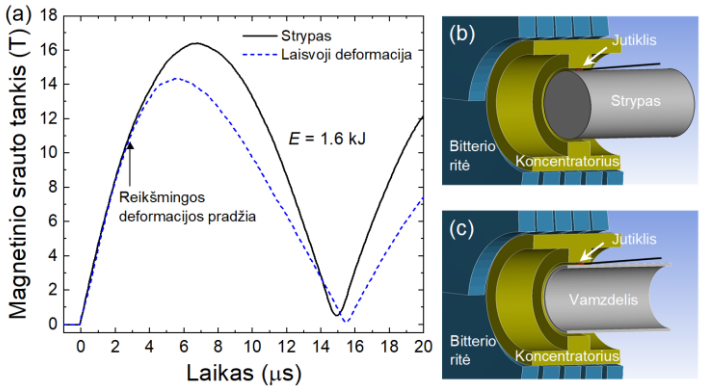
3.8a pav. pateiktos magnetinio srauto tankio kitimo laike kreivės, išmatuotos dviem konfigūracijomis: su tuščiu magnetinio lauko koncentratoriumi (raudona kreivė) ir su į jį įstatytu aliuminio strypu (juoda kreivė). Abiejų konfigūracijų skerspjūviai pateikti 3.8b, c pav. Magnetinio srauto tankis, kaip ir iškrovos srovė, kito slopstančiais svyravimais. Slopimą aprašanti eksponentinė laiko konstanta τ sumažėjo nuo 110 μs, kai koncentratorius buvo tuščias, iki 80 μs, kai į jį įstatytas 19 mm skersmens aliuminio strypas. Įstačius laidų ruošinį, magnetinio srauto tankio amplitudė padidėjo nuo 9,4 T iki 16,5 T, t. y. 1,8 karto, o svyravimų periodas sumažėjo.



3.8 pav. Magnetinio srauto tankio laikinė priklausomybė lauko koncentratoriuje, kai jis tuščias (raudona kreivė), ir kai į lauko koncentratorių įstatytas aliuminio strypas (juoda kreivė). Eksperimentinių konfigūracijų skerspjūvio schemos: (b) be ruošinio, parodant jutiklio padėtį tuščiame lauko koncentratoriuje; (c) su aliuminio strypu.

Magnetinio srauto tankio padidėjimą lemia koncentratoriaus sukuriamo lauko ir antrinio lauko, kurį sukuria aliuminio strype indukuotos sūkurinės srovės, superpozicija: tarpe tarp strypo ir koncentratoriaus šių laukų kryptys sutampa, todėl laukai sudedami. Rezultatai rodo, kad tiesioginiai magnetinio lauko matavimai teikia informacijos, kurios vien iš iškrovos srovės matavimų gauti negalima, nes magnetinio srauto tankį lemia ne tik ritėje tekanti srovė, bet ir laidaus ruošinio elektromagnetinis atsakas bei kintanti sistemos geometrija.

Toliau magnetinio lauko kitimas tirtas vietoj nedeformuojamo strypo naudojant judantį aliuminio vamzdinį ruošinį. 3.9a pav. pateiktas pirmasis magnetinio srauto tankio impulsas, išmatuotas į magnetinio lauko koncentratorių įstačius 19 mm išorinio skersmens aliuminio vamzdinį ruošinį, kuriam kondensatoriaus iškrovos metu leista laisvai deformuotis (mėlyna punktyrinė kreivė). Palyginti tame pačiame paveiksle pateikta magnetinio



3.9 pav. Magnetinio lauko kitimas pirmojo pusperiodžio metu, kai į lauko koncentratorių įdėtas aliuminio vamzdis (mėlyna punktyrinė kreivė), palyginti su tokio pat skersmens aliuminio strypu (juoda kreivė). (b) eksperimentinių konfigūracijos skerspjūvio schema su aliuminio strypu. (c) su aliuminio vamzdžiu.

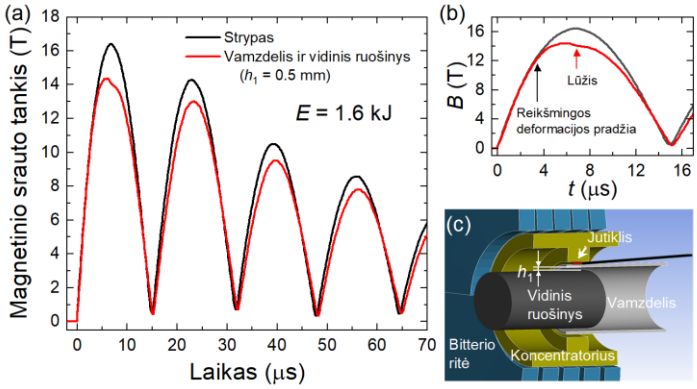
srauto tankio kitimo laike kreivė, išmatuota su tokio paties skersmens vientisu aliuminio strypu (juoda ištisinė kreivė).

Impulso pradžioje abi kreivės sutampa, tačiau maždaug nuo 3 μs jos ima skirtis. Deformuojamo ruošinio atveju magnetinio srauto tankio maksimumas pasiekiamas anksčiau ir yra mažesnis negu nedeformuojamo strypo atveju. Taip yra todėl, kad prasidėjus ruošinio deformacijai didėja tarpas tarp jo išorinio paviršiaus ir magnetinio lauko koncentratoriaus, todėl jutiklio registruojamas magnetinio srauto tankis mažėja. Be to, pirmojo pusperiodžio trukmė ilgesnė negu nedeformuojamo strypo atveju, nes dėl deformacijos padidėja sistemos induktyvumas.

Šie rezultatai rodo, kad magnetinio srauto tankio kitimas laike atspindi ruošinio deformacijos eigą ir gali būti naudojamas deformacijos pradžiai nustatyti.

Kito eksperimento metu magnetinio lauko kitimas tirtas į aliuminio vamzdinį ruošinį įstačius nerūdijančiojo plieno strypą. Išmatuotas magnetinio srauto tankio kitimas laike pateiktas 3.10a pav. (raudona kreivė), padidintas pirmojo pusperiodžio vaizdas – 3.10b pav., o eksperimentinės sistemos skerspjūvis – 3.10c pav. Naudotas 17 mm skersmens plieninis strypas, todėl tarp vidinės vamzdinio ruošinio sienelės ir nejudančio ruošinio paviršiaus susidarė h_1 = 0,5 mm pradinis atstumas (3.10c pav.). Eksperimentai atlikti esant 1,6 kJ iškrovos energijai.

Rezultatams palyginti 3.10a, b pav. pateikta ir ankstesnio eksperimento su vientisu aliuminio strypu magnetinio srauto tankio kitimo laike kreivė (juoda kreivė). Ties pirmuoju magnetinio srauto tankio maksimumu matyti aiškus

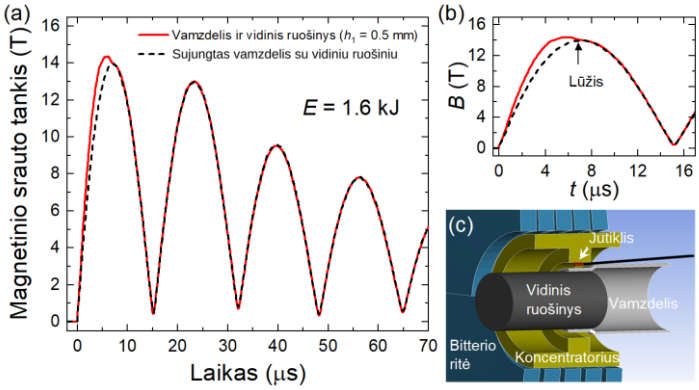


3.10 pav. ((a) Magnetinio srauto tankio kitimas tarpe tarp magnetinio lauko koncentratoriaus ir nedeformuojamo standaus aliuminio strypo (juoda kreivė) bei tarpe tarp magnetinio lauko koncentratoriaus ir suvirinimo proceso metu deformuojamo aliuminio vamzdelio (raudona kreivė). (b) Padidintas pirmojo magnetinio lauko piko vaizdas, rodantis intensyvios vamzdelio deformacijos pradžią ir charakteringą raudonos kreivės lūžį suvirinimo proceso metu. (c) Eksperimentinės sistemos ir ruošinių scheminis skerspjūvis prieš suvirinimo procesą.

kreivės lūžis, kurį lemia aliuminio vamzdinio ruošinio susidūrimas su nejudančiu ruošiniu. Po susidūrimo visi vėlesni pusperiodžiai įgauna taisyklingą slopstančio sinusinio svyravimo formą; tai rodo, kad ruošinys toliau nebedeformuojamas ir jo geometrija nebekinta.

Šiai išvadai patvirtinti tas pats bandinys veiktas antru magnetinio lauko impulsu. Palyginus pirmojo ir antrojo impulsų magnetinio srauto tankio kitimo laike kreives nustatyta, kad nuo antrojo maksimumo jos visiškai sutampa, o pirmojo impulso metu sutapimas prasideda iš karto pasibaigus būdingam kreivės lūžiui (3.11 pav.). Tai patvirtino, kad lūžiui pasibaigus ruošinio deformacija ir jo susidūrimas su nejudančiu ruošiniu jau yra įvykę, o toliau sistema veikia kaip vientisas nedeformuojamas darinys.

Toliau tirta pradinio atstumo tarp ruošinių ir iškrovos energijos įtaka magnetinio srauto tankio kitimui laike. Nustatyta, kad didėjant pradiniam atstumui būdingas kreivės lūžis slenka į vėlesnį laiką, nes judančiam ruošiniui reikia daugiau laiko nejudančiam ruošiniui pasiekti. Didinant iškrovos energiją nuo 1,6 iki 2,0 ir 2,5 kJ, magnetinio srauto tankio amplitudė padidėjo atitinkamai nuo 14,4 T iki 15,8 T ir 16,5 T, o susidūrimas įvyko anksčiau dėl didesnio magnetinio slėgio ir didesnio judančio ruošinio pagreičio.



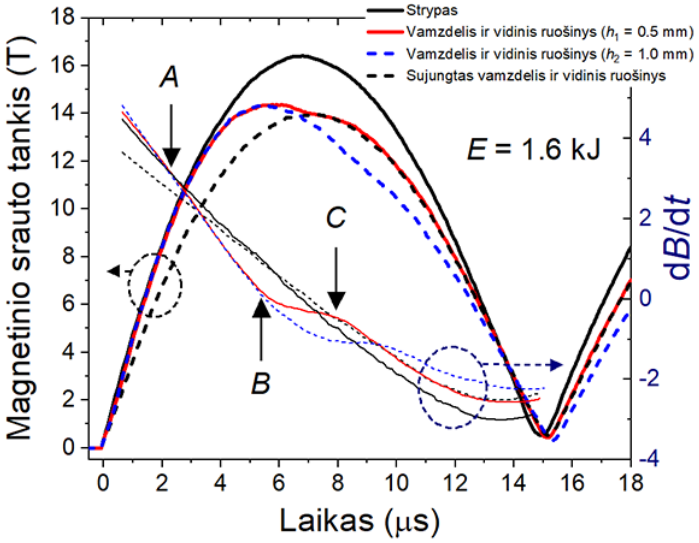
3.11. pav. (a) Magnetinio srauto tankio kitimas magnetinio impulsinio suvirinimo metu (raudona kreivė) ir po suvirinimo, pakartotinai sužadinus jau sujungtą vamzdelio ir pagrindinio ruošinio jungtį (juoda punktyrinė kreivė). (b) Padidintas pirmojo magnetinio lauko piko vaizdas, rodantis raudonos ir juodos punktyrinės kreivių sutapimą po charakteringo lūžio. (c) Eksperimentinės sistemos ir suvirinimo proceso metu sujungtų ruošinių scheminis skerspjūvis.

Rezultatai rodo, kad magnetinio srauto tankio kitimas laike leidžia nustatyti ne tik deformacijos ir susidūrimo momentus, bet ir kiekybiškai įvertinti technologinių parametrų – pradinio atstumo tarp ruošinių ir iškrovos energijos – įtaką magnetinio impulsinio suvirinimo procesui.

Matavimo rezultatams palyginti visų pagrindinių eksperimentų magnetinio srauto tankio kitimo laike kreivės pateiktos 3.12 pav. (storos linijos), o tame pačiame paveiksle – šių kreivių išvestinės pagal laiką dB/dt (plonos linijos). Išvestinių kreivėse nustatyti trys būdingi taškai, atitinkantys skirtingus deformacijos ir susidūrimo etapus.

Taškas A atitinka judančio ruošinio deformacijos pradžią, kai jį ima veikti magnetinis slėgis. Šis taškas nustatytas praėjus maždaug 2,4 μs nuo iškrovos pradžios ir yra toks pat abiem atvejais – kai pradinis atstumas tarp ruošinių h_1 = 0,5 mm ir kai h_2 = 1,0 mm. Taip yra todėl, kad abiejuose eksperimentuose vamzdinio ruošinio geometrija ir iškrovos energija buvo vienodos, o nejudantis ruošinys deformacijos pradžiai įtakos neturi, nes judantis ruošinys jo dar nepasiekęs.

Taškas B žymi judančio ruošinio susidūrimo su plieniniu nejudančiu ruošiniu pradžią. Kai h_1 = 0,5 mm, susidūrimas prasidėjo ties 5,4 μs, o kai h_2 = 1,0 mm – ties 7,0 μs. Taškas C atitinka susidūrimo pabaigą: nuo jo judantis ir nejudantis ruošiniai toliau veikia kaip vientisas nedeformuojamas darinys. Šis momentas nustatytas ties 8,0 μs, kai h_1 = 0,5 mm, ir ties 9,8 μs, kai h_2 = 1,0 mm.



3.12 pav. Magnetinio srauto tankis *B(t)* (storos linijos) ir jo išvestinė laiko atžvilgiu dB/dt (plonos linijos) pirmojo slopstančiųjų osciliacijų piko metu keturiomis eksperimentinėmis sąlygomis: kai į koncentratorių (LK) įstatytas aliuminio strypas (juoda kreivė), suvirinant aliuminio vamzdelį su 17 mm skersmens plieniniu pagrindiniu ruošiniu (h_1 = 0,5 mm, raudona kreivė), po suvirinimo su šiuo pagrindiniu ruošiniu (juoda punktyrinė kreivė) ir kai vamzdelis suvirinamas su 16 mm skersmens pagrindiniu ruošiniu (h_2 = 1 mm, mėlyna punktyrinė kreivė). Taškai A, B ir C atitinkamai žymi vamzdelio deformacijos pradžią, vamzdelio susidūrimo su pagrindiniu ruošiniu pradžią ir susidūrimo pabaigą.

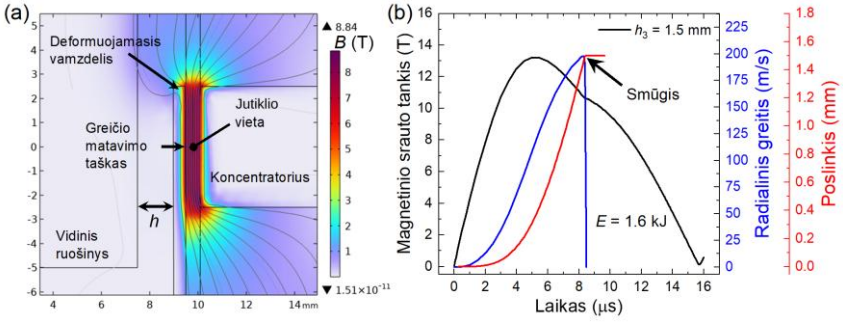
Laiko intervalas tarp taškų B ir C apibrėžia judančio ir nejudančio ruošinio sąveikos trukmę susidūrimo metu. Nustatyta, kad didinant pradinį atstumą tarp ruošinių vėluoja ir susidūrimo pradžia, ir jo pabaiga, nes judantis ruošinys ilgiau greitinamas, kol pasiekia nejudantį ruošinį.

Taigi sukurtas magnetinio lauko matavimo metodas leidžia neinvaziškai nustatyti deformacijos pradžios, susidūrimo pradžios ir pabaigos momentus bei susidūrimo trukmę magnetinio impulsinio suvirinimo metu. Šie laiko momentai yra tiesiogiai išmatuoti proceso parametrai, tinkami magnetinio impulsinio suvirinimo mechanizmams tirti ir susietiesiems elektromagnetiniams–mechaniniams skaitiniams modeliams patikrinti.

Toliau atliktas judančio aliuminio ruošinio deformacijos ir susidūrimo skaitinis tyrimas magnetinio impulsinio suvirinimo metu, taikant COMSOL Multiphysics aplinkoje sukurtą susietąjį elektromagnetinį–mechaninį modelį. Modelis sudarytas pagal eksperimentinę konfigūraciją ir taikytas magnetinio srauto tankio kitimui tarpe tarp magnetinio lauko koncentratoriaus ir judančio

ruošinio bei šio ruošinio radialiniam greičiui apskaičiuoti. Skaičiavimai atlikti esant 1,6; 2,0 ir 2,5 kJ iškrovos energijoms, atitinkančioms eksperimento sąlygas.

3.13 pav. pateiktas magnetinio srauto tankio ir judančio ruošinio radialinio greičio kitimas laike deformacijos ir susidūrimo metu. Modeliuota magnetinio srauto tankio kreivė pirmojo pusperiodžio metu atkartoja eksperimentiškai stebėtą būdingą lūžį. Radialinio greičio kitimas rodo, kad šis lūžis sutampa su judančio ruošinio susidūrimo su plieniniu nejudančiu ruošiniu momentu. Esant pradiniam atstumui tarp ruošinių h_3 = 1,5 mm ir 1,6 kJ iškrovos energijai, susidūrimas įvyko ties 8,3 μs, kai judantis ruošinys buvo pasiekęs didžiausią 198 m/s radialinį greitį. Po susidūrimo radialinis greitis staigiai sumažėjo iki nulio, todėl magnetinio srauto tankio kreivės lūžis siejamas su perėjimu nuo laisvos ruošinio deformacijos prie mechaninės sąveikos su nejudančiu ruošiniu.

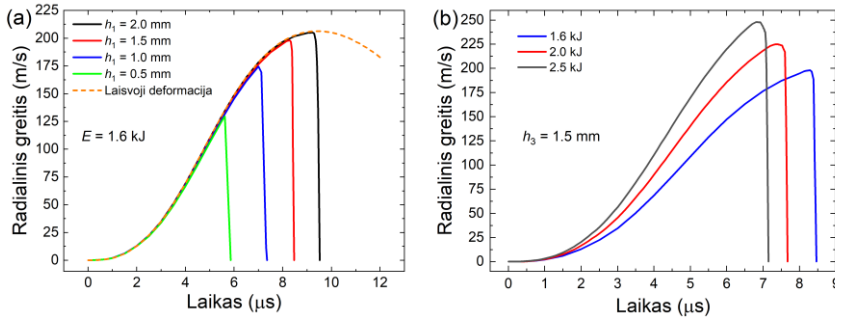


3.13 pav. Dvimatis COMSOL Multiphysics magnetinio impulso suvirinimo proceso modeliavimas, kuriame pavaizduotas lauko koncentratorius, aliuminio lakštinis vamzdelis ir plieninis pagrindinis ruošinys. Magnetinio srauto tankio matavimo jutiklio padėtis nurodyta oro tarpe tarp lauko koncentratoriaus ir vamzdelio sienelės, tarpo vidurinėje dalyje. Greičio matavimo taškas yra ant lakštinio vamzdelio paviršiaus, šalia jutiklio padėties. (b) Magnetinio srauto tankio priklausomybės nuo laiko modeliavimas (juoda kreivė) oro srityje magnetinio impulso suvirinimo metu, kai iškrovos energija yra 1,6 kJ, o atramos atstumas h_3 = 1,5 mm. Lakštinio vamzdelio paviršiaus radialinio greičio priklausomybė nuo laiko (mėlyna kreivė) matavimo taške pateikta dešinėje ašyje.

3.14 pav. parodyta pradinio atstumo tarp ruošinių ir iškrovos energijos įtaka judančio ruošinio radialinio greičio kitimui laike. 3.14a pav. pateiktos radialinio greičio kreivės esant skirtingiems pradiniams atstumams (ištisinės linijos) ir laisvos deformacijos atveju (brūkšninė linija). Didinant pradinį atstumą ilgėja laikas iki susidūrimo, tačiau prieš susidūrimą judantis ruošinys pasiekia didesnį radialinį greitį. Esant 2,0 mm pradiniam atstumui, greitis

susidūrimo momentu siekė 204 m/s ir buvo artimas didžiausiam laisvos deformacijos atveju pasiekiamam greičiui (206 m/s). Taigi didesnis pradinis atstumas leidžia elektromagnetinei jėgai ilgiau veikti ruošinį, todėl prieš susidūrimą pasiekiamas didesnis greitis.

3.14b pav. pateiktos radialinio greičio kreivės, kai pradinis atstumas h_3 = 1,5 mm nekinta, o keičiama iškrovos energija. Didinant iškrovos energiją didėja susidūrimo metu pasiekiamas greitis ir trumpėja laikas, per kurį judantis ruošinys pasiekia nejudantį ruošinį. Tai lemia didesnis magnetinis slėgis, susidarantis esant didesnei iškrovos energijai.



3.14 pav. COMSOL Multiphysics vamzdelio radialinio greičio modeliavimas esant skirtingiems atramos atstumams h ir 1,6 kJ iškrovos energijai. (b) Vamzdelio radialinio greičio kreivės esant pastoviam atramos atstumui h_3 = 1,5 mm ir trims skirtingoms iškrovos energijoms.

Skaitinių ir eksperimentinių rezultatų palyginimas parodė, kad modelis atkartoja eksperimentiškai stebėtą magnetinio srauto tankio kitimą laike ir jo būdingus požymius, o apskaičiuoti ir išmatuoti susidūrimo momentai sutampa ±0,4 μs tikslumu. Tai patvirtina, kad magnetinio srauto tankio kitimas laike tinka judančio ruošinio deformacijos ir jo susidūrimo su nejudančiu ruošiniu etapams nustatyti, o sukurtas susietasis elektromagnetinis–mechaninis modelis – magnetinio impulsinio suvirinimo pereinamiesiems elektromagnetiniams ir mechaniniams reiškiniams analizuoti.

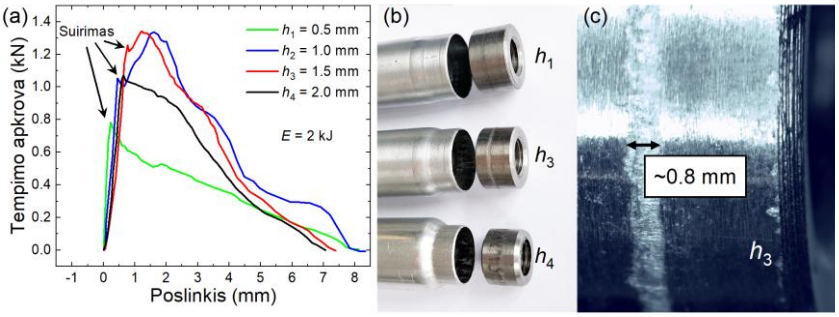
Toliau tirtos magnetiniu impulsiniu suvirinimu suformuotų aliuminio vamzdinio ruošinio ir nerūdijančiojo plieno strypo jungčių mechaninės savybės. Suvirinti bandiniai tempti iki suirimo TIRA 2300 bandymų įrenginiu, siekiant nustatyti didžiausią jungties atlaikomą tempimo apkrovą ir įvertinti iškrovos energijos bei pradinio atstumo tarp ruošinių įtaką jungties stiprumui.

3.15a pav. pateiktos tempimo bandymų apkrovos ir poslinkio kreivės bandiniams, suvirintiems esant 2,0 kJ iškrovos energijai ir naudojant skirtingo skersmens plieninius strypus. Kreivėse matyti tamprios ir plastinės deformacijos tarpsniai, po kurių pasiekiama didžiausia apkrova, atitinkanti

jungties irimo pradžią. Ją pasiekus, aliuminio ruošinys atsiskiria nuo plieninio strypo ir apkrova staiga sumažėja.

Nustatyta, kad didžiausia tempimo apkrova priklauso nuo pradinio atstumo tarp ruošinių. Padidinus jį nuo h_1 = 0,5 mm iki h_3 = 1,5 mm, didžiausia tempimo apkrova padidėjo nuo 0,78 kN iki 1,26 kN. Tai siejama su didesniu judančio ruošinio greičiu prieš susidūrimą. Tačiau toliau didinant pradinį atstumą iki h_4 = 2,0 mm, didžiausia tempimo apkrova sumažėjo iki 1,07 kN, nors būtent šiuo atveju apskaičiuotas susidūrimo greitis yra didžiausias. Vadinasi, didelis susidūrimo greitis savaime neužtikrina didžiausio jungties stiprumo: svarbi ir deformacijos tolygumas. Eksperimentiniai stebėjimai parodė, kad esant h_4 = 2,0 mm aliuminio ruošinio sienelė deformuojasi netolygiai – susidaro išilginės klostės, o skerspjūvis tampa daugiakampis, todėl su plieniniu strypu kontaktuoja tik įlinkusios sienelės dalys. Dėl to suvirintos jungties stiprumas sumažėja.

3.15b ir 3.15c pav. pateiktos aliuminio vamzdinių ruošinių ir plieninių strypų nuotraukos po tempimo bandymų. Jose matyti skirtingas aliuminio ruošinių deformacijos pobūdis ir nevienodo pločio prilipusio aliuminio pėdsakai ant plieninių strypų paviršiaus. Esant mažam pradiniam atstumui (h_1 = 0,5 mm), po bandymo ant plieninio paviršiaus lieka tik pavieniai nedideli aliuminio pėdsakai; tai rodo silpną sukibimą ir adhezinį jungties irimą, kai ardoma pati medžiagų sandūra. Padidinus pradinį atstumą iki h_3 = 1,5 mm, ant plieninio paviršiaus lieka ištisinis aliuminio sluoksnis, t. y. irimas vyksta jau pačiame aliuminyje (kohezinis irimas), o tai rodo stipresnę jungtį. Esant h_4 = 2,0 mm matyti didelė aliuminio ruošinio plastinė deformacija, o plieninio ruošinio paviršiuje – išilginių sienelės klosčių įspaudai; jie rodo, kad



3.15 pav. Tempimo apkrovos–poslinkio kreivės keturiems bandiniams, suvirintiems esant 2 kJ iškrovos energijai ir skirtingiems pradiniams tarpams h_1, h_2, h_3 ir h_4. (b) Aliuminio vamzdelių ir plieninių strypų vaizdai po tempimo bandymų. (c) Bandinio, suvirinto esant h_3 = 1,5 mm pradiniam tarpui ir 2 kJ iškrovos energijai, suirimo paviršius ir suvirinimo zonos plotis.

susidūrimo metu kontaktas buvo netolygus, ir dėl to jungties stiprumas sumažėjo.

Šie rezultatai rodo, kad magnetinio impulsinio suvirinimo procese esama optimalaus pradinio atstumo tarp judančio ir nejudančio ruošinio: šioje konfigūracijoje didžiausia tempimo apkrova gauta esant h_3 = 1,5 mm, ir taip yra prie visų trijų tirtų iškrovos energijų. Per mažas pradinis atstumas riboja judančio ruošinio greitį prieš susidūrimą ir sumažina suvirintos srities plotį, o per didelis lemia perteklinę plastinę deformaciją ir netolygų kontaktą su nejudančiu ruošiniu. Tempimo bandymų, tiesioginių magnetinio lauko matavimų ir skaitinio modeliavimo rezultatai rodo, kad jungties susidarymą lemia susidūrimo greičio, susidūrimo kampo ir kontakto tolygumo derinys, o ne vien susidūrimo greitis.

Apibendrinant šio poskyrio rezultatus, sukurta CMR B-skaliarinė magnetinio lauko matavimo sistema leidžia tirti pereinamuosius elektromagnetinius procesus magnetinio impulsinio suvirinimo metu nekeičiant suvirinimo įrangos konstrukcijos. Magnetinio srauto tankio matavimai tarpe tarp magnetinio lauko koncentratoriaus ir judančio ruošinio teikia tiesioginę informaciją apie elektromagnetinio lauko ir ruošinio mechaninio atsako sąveiką.

Nustatyta, kad vien per ritę tekančios iškrovos srovės magnetinio impulsinio suvirinimo procesui analizuoti nepakanka. Magnetinio srauto tankio matavimai ir jo išvestinės pagal laiką analizė leido nustatyti pagrindinius proceso etapus: judančio ruošinio deformacijos pradžią ir susidūrimo su nejudančiu ruošiniu pradžios bei pabaigos momentus.

Sukurtas COMSOL Multiphysics modelis patvirtino eksperimentinių rezultatų interpretaciją: jis atkartojo būdingus magnetinio srauto tankio kitimo požymius, o apskaičiuoti ir išmatuoti susidūrimo momentai sutampa ±0,4 μs tikslumu. Patikrintas dviem nepriklausomais dydžiais – magnetinio srauto tankio kitimu ir susidūrimo momentu – modelis leido apskaičiuoti judančio ruošinio radialinį greitį prieš susidūrimą, kurio iš išmatuoto magnetinio lauko kitimo tiesiogiai gauti negalima.

Tempimo bandymai parodė, kad suvirintos jungties stiprumas priklauso ir nuo iškrovos energijos, ir nuo pradinio atstumo tarp ruošinių. Didesnis pradinis atstumas padidina judančio ruošinio greitį prieš susidūrimą, tačiau pernelyg didelis lemia perteklinę plastinę deformaciją, netolygų kontaktą su nejudančiu ruošiniu ir mažesnį jungties stiprumą.

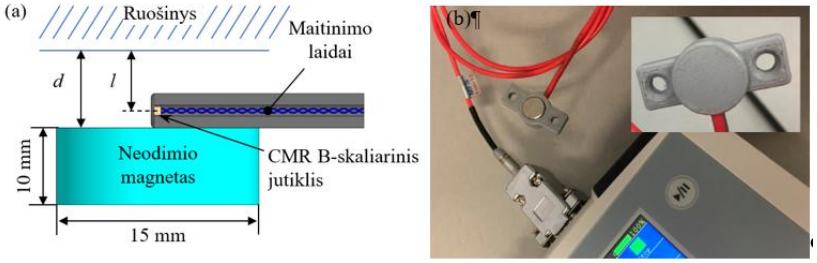
Taigi tiesioginiai magnetinio lauko matavimai siaurame tarpe tarp magnetinio lauko koncentratoriaus ir judančio ruošinio yra tinkamas metodas susietiems elektromagnetiniams ir mechaniniams reiškiniams magnetinio impulsinio suvirinimo metu tirti. Sukurtas metodas leidžia nustatyti

pagrindinius proceso etapus, įvertinti technologinių parametrų įtaką ruošinio deformacijai, susidūrimo eigai ir jungties stiprumui bei sudaro eksperimentinį pagrindą skaitiniams modeliams patikrinti.

3.4 Magnetinio artumo matavimų CMR B-skaliariniais jutikliais tyrimas

Šiame poskyryje pateikti magnetinio atstumo matavimų CMR B-skaliariniais jutikliais eksperimentinių tyrimų rezultatai. Nagrinėti du artumo matavimo principai: pirmasis pagrįstas nuolatinio magneto sukuriamo statinio magnetinio lauko pokyčių, atsirandančių dėl metalinio objekto judėjimo, registravimu, antrasis – magnetinio impulsinio suvirinimo metu sukuriamo pereinamojo magnetinio lauko panaudojimu galutinei suvirinto mazgo geometrijai nustatyti.

Pirmuoju atveju sukurtas CMR B-skaliariniu jutikliu pagrįstas magnetinio artumo jutiklis su N35 klasės neodimio nuolatiniu magnetu, sukuriančiu statinį magnetinį lauką; CMR jutiklis registruoja šio lauko pokyčius, atsirandančius keičiantis metalinio objekto padėčiai. Jutiklio sandara ir matavimo principas pateikti 3.16 pav.



3.16 pav. Magnetinio artumo jutiklio konstrukcijos, pagrįstos CMR B-skaliariniu jutikliu ir nuolatiniais magnetais: (a) CMR pagrindu sukurto MPP skerspjūvis su vientisu magnetiniu cilindru; (b) prie magnetinio lauko matuoklio prijungto MPP nuotrauka. Įterptame paveikslėlyje pateikta pagaminto jutiklio priekinės dalies nuotrauka.

Į jutiklį integruotas Pt1000 temperatūros jutiklis. Jis leidžia stebėti jutiklio temperatūrą matavimo metu ir parinkti atitinkamą kalibravimo kreivę, pagal kurią jutiklio varžos pokytis perskaičiuojamas į magnetinio srauto tankio vertę.

Antrasis principas pagrįstas paties magnetinio impulsinio suvirinimo metu sukuriamo impulsinio magnetinio lauko panaudojimu žadinimo šaltiniu. Šiuo atveju tas pats CMR B-skaliarinis jutiklis, kuriuo tirtas magnetinio lauko

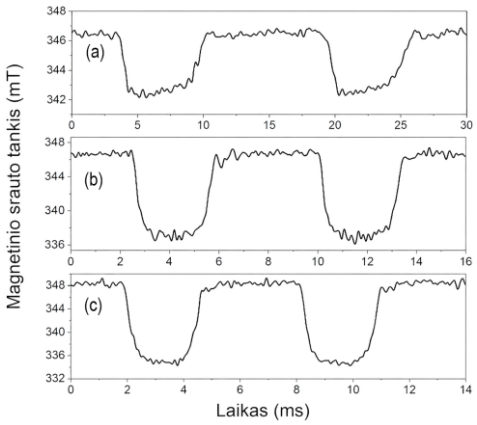
kitimas ruošinio deformacijos ir susidūrimo metu, naudojamas ir galutinei ruošinio padėčiai po suvirinimo nustatyti.

Jutiklio tinkamumui metalinių objektų padėčiai ir judėjimui nustatyti įvertinti atlikti statiniai ir dinaminiai matavimai. Statiniai matavimai atlikti su nejudančia feromagnetine plienine plokšte, dinaminiai – su besisukančiais feromagnetiniais (plieno) ir neferomagnetiniais (diuraliuminio) diskais.

Matavimai su nejudančia plienine plokšte parodė, kad magnetinio srauto tankio pokytis ΔB didėja mažėjant atstumui l tarp jutiklio ir objekto. Eksperimentinė priklausomybė $\Delta B(l)$ aproksimuota empirine interpoliacine išraiška, galiojančia išmatuotame atstumų intervale.

Dinaminiai matavimai su besisukančiu plieno disku parodė, kad feromagnetiniam objektui artėjant prie jutiklio magnetinio srauto tankio pokytis yra teigiamas. Esant 30 Hz sukimosi dažniui, atsako impulse matyti du būdingi maksimumai, atitinkantys objekto priartėjimą prie jutiklio ir nutolimą nuo jo. Didinant sukimosi dažnį impulso trukmė trumpėjo, o jo forma keitėsi, tačiau didžiausia signalo amplitudė beveik nekito. Tai rodo, kad atsako amplitudę lemia objekto padėtis, o ne jo greitis: plieno plokštėje įmagnetinimą sukelia magneto laukas, ir šis įmagnetinimas nuo greičio nepriklauso.

3.17 pav. pateiktas jutiklio atsakas į besisukantį diuraliuminio diską. Skirtingai negu plieno atveju, magnetinio srauto tankio pokytis neigiamas ($\Delta B < 0$). Didinant sukimosi dažnį atsako impulso trukmė trumpėjo, o amplitudė didėjo. Esant mažam sukimosi dažniui signalas asimetriškas – greitai didėja ir lėčiau mažėja; didėjant dažniui asimetrija mažėja. Šie požymiai siejami su judančiame neferomagnetiniame laidininke indukuojamomis sūkurinėmis srovėmis, kurių dydis priklauso nuo objekto greičio.

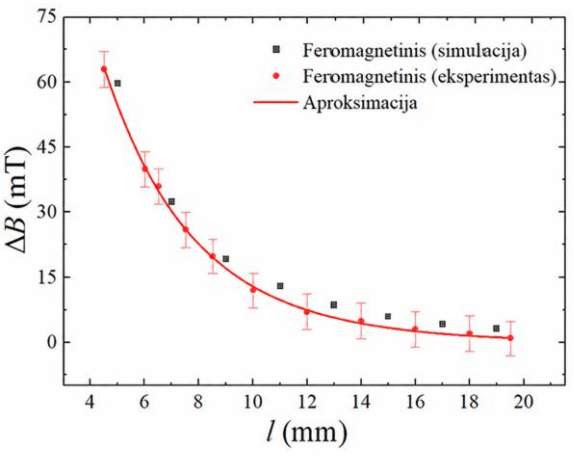


3.17 pav. CMR pagrindu sukurto MPP atsakas į duraliuminio plokštelę esant skirtingiems sukimosi dažniams: (a) 30 Hz, (b) 65 Hz, (c) 80 Hz.

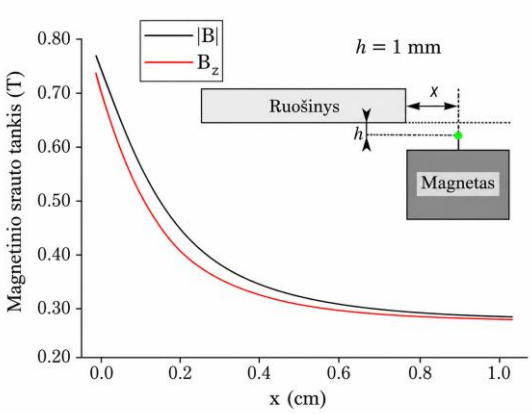
Taigi atsako ženklas nurodo objekto pobūdį: feromagnetinio objekto atveju magnetinio srauto tankis jutiklio vietoje didėja, neferomagnetinio laidaus objekto atveju – mažėja. Šie du mechanizmai – įmagnetinimo sukeltas magnetinio lauko persiskirstymas ir sūkurinių srovių laukas – leidžia vienu skaliariniu matavimu atskirti feromagnetinį objektą nuo neferomagnetinio laidaus objekto.

Eksperimentiškai nustatytai priklausomybei $\Delta B(l)$ paaiškinti atliktas magneto ir objekto sistemos skaitinis modeliavimas: dvimačiu ašiai simetriniu baigtinių elementų modeliu COMSOL Multiphysics aplinkoje apskaičiuotas magnetinio lauko pasiskirstymas. Skaičiuojant naudotos nepriklausomai nustatytos magneto liekamojo magnetinio srauto tankio ir plokštės santykinės magnetinės skvarbos vertės; nė vienas parametras prie artumo matavimo duomenų nederintas. Apskaičiuota $\Delta B(l)$ priklausomybė atitinka eksperimentinę (3.18 pav.). Modeliavimas parodė, kad feromagnetinis objektas padidina magnetinio srauto tankį tarpe tarp magneto ir objekto dėl magnetinio srauto koncentracijos šiame tarpe.

Objekto padėties magneto ašies atžvilgiu įtaka pateikta 3.19 pav. Toliau nuo ašies magnetinio lauko trikdys įgyja stiprią radialinę dedamąją, kurios tik vieną lauko dedamąją matuojantis jutiklis neužfiksuoja. CMR B-skaliarinis jutiklis matuoja magnetinio srauto tankio modulį, todėl šioje srityje jo signalas didesnis ir mažiau priklauso nuo objekto padėties.



3.18 pav. Magnetinio srauto tankio pokytis priklausomai nuo atstumo l tarp CMR jutiklio ir plieninio objekto CMR pagrindu veikiančiame artumo jutiklio: eksperimentiniai rezultatai (raudoni taškai), modeliavimo rezultatai (juodi kvadratai).



3.19 pav. Paveiksle pateiktos MPP schemoje parodyto magnetinio srauto tankio modulio ir vertikaliosios komponentės priklausomybės. X ašis žymi radialinį atstumą *x* tarp magneto ašies ir matuojamo objekto.

Besisukančio plieno disko skaitinis modeliavimas parodė, kad esant mažam sukimosi dažniui atsako formą lemia objekto geometrija ir jo padėtis jutiklio atžvilgiu; tai patvirtino statiniai trimačiai skaičiavimai. Didėjant sukimosi dažniui atsako forma kinta dėl paties plieno disko, kaip laidininko, judėjimo magneto lauke sukeliamų sūkurinių srovių: šis indukcinis dėmuo proporcingas greičiui ir keičia ženklą tarp objekto priartėjimo ir nutolimo, todėl impulso forma tampa asimetriška, o įmagnetinimo lemiama didžiausia amplitudė nekinta.

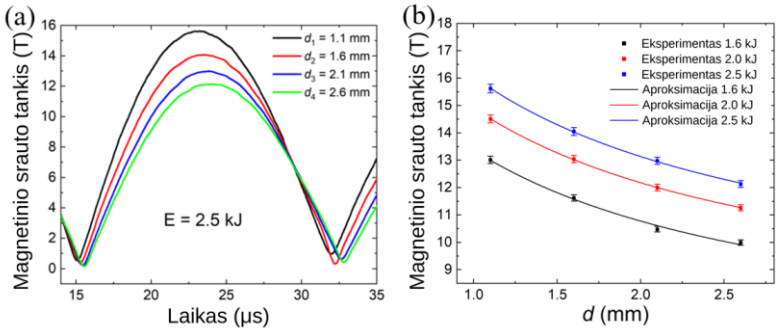
Besisukančio diuraliuminio disko atveju atsakas paaiškintas laidžioje neferomagnetinėje medžiagoje indukuojamomis sūkurinėmis srovėmis. Jų sukurtas antrinis laukas priešinasi magnetinio srauto pokyčiui, todėl registruojamas neigiamas magnetinio srauto tankio pokytis. Didėjant sukimosi dažniui atsako amplitudė didėjo, o impulso trukmė trumpėjo.

Toliau parodyta galimybė CMR B-skaliarinį jutiklį naudoti artumo diagnostikai paties magnetinio impulsinio suvirinimo metu. Pirmasis magnetinio lauko pusperiodis teikia informaciją apie ruošinio deformaciją ir susidūrimo momentą, o vėlesnių, jau po susidūrimo registruojamų pusperiodžių maksimumai priklauso nuo galutinio atstumo d tarp lauko koncentratoriaus vidinio paviršiaus ir suvirinto mazgo išorinio paviršiaus. Didžiausias iš jų yra antrojo pusperiodžio maksimumas, todėl jis pasirinktas galutinio atstumo rodikliu.

3.20 pav. pateiktos antrojo pusperiodžio maksimumo vertės, išmatuotos esant skirtingiems pradiniams atstumams tarp ruošinių. Mažesnis pradinis atstumas tarp ruošinių atitinka mažesnį galutinį atstumą d tarp koncentratoriaus ir ruošinio paviršiaus, o kartu – didesnę antrojo pusperiodžio

amplitudę. Esant 2,5 kJ iškrovos energijai amplitudė padidėjo nuo 12,13 T iki 15,62 T, galutiniam atstumui sumažėjus nuo 2,6 iki 1,1 mm; ta pati monotoninė priklausomybė gauta ir esant 1,6 bei 2,0 kJ energijoms.

Taigi tarp magnetinio lauko koncentratoriaus ir judančio ruošinio įtaisytas CMR B-skaliarinis jutiklis leidžia nustatyti galutinę ruošinio paviršiaus padėtį nejudančios koncentratoriaus ir jutiklio poros atžvilgiu nenaudojant papildomos poslinkio matavimo sistemos.



3.20 pav. Magnetinio srauto tankio antroji pusbangė esant 2,5 kJ iškrovos energijai; (b) Didžiausia antrojo magnetinio lauko piko amplitudė kaip galutinio atstumo tarp vamzdelio ir jutiklio funkcija.

Apibendrinant šio poskyrio rezultatus, CMR B-skaliariniais jutikliais pagrįstas magnetinio lauko matavimo metodas tinka metalinių objektų artumui matuoti ir galutinei ruošinio padėčiai magnetinio impulsinio suvirinimo metu nustatyti. Ištirti du artumo matavimo būdai: su nuolatiniu magnetu kaip statinio lauko šaltiniu ir su paties suvirinimo proceso sukuriamu impulsiniu magnetiniu lauku.

Sukurtas atstumo jutiklis parodė aiškią jutiklio signalo priklausomybę nuo atstumo iki feromagnetinio objekto: magnetinio srauto tankio pokytis didėjo mažėjant atstumui ir buvo aproksimuotas empirine išraiška. Baigtinių elementų modeliavimas atkartojo eksperimentinę priklausomybę ir paaiškino objekto įmagnetinimo įtaką jutiklio atsakui.

Matavimai su besisukančiais plieno ir diuraliuminio diskais parodė skirtingus signalo susidarymo mechanizmus: feromagnetinio objekto atveju atsaką lemia įmagnetinimo sukeltas magnetinio lauko persiskirstymas dėl didelės medžiagos magnetinės skvarbos, neferomagnetinio – judėjimo metu indukuojamos sūkurinės srovės. Atsako ženklas leidžia šiuos objektus atskirti.

Atstumo matavimo principas pritaikytas ir tiesiogiai magnetinio impulsinio suvirinimo procese: magnetinio srauto tankio kitimas laike teikia informaciją ir apie ruošinio deformaciją bei susidūrimą pirmojo pusperiodžio metu, ir apie galutinę suvirinto mazgo geometriją, t. y. atstumą d tarp

koncentratoriaus ir mazgo išorinio paviršiaus, kurį nusako antrojo pusperiodžio amplitudė. Taigi CMR B-skaliariniais jutikliais pagrįstas magnetinio lauko matavimo metodas leidžia vienu neinvaziniu matavimu tirti elektromagnetinius procesus, ruošinio deformaciją ir susidūrimo eigą bei nustatyti galutinę suvirintos jungties geometriją.

BENDROSIOS IŠVADOS

1. Plonųjų $La_{0.8}Sr_{0.2}Mn_{1.15}O_3$ sluoksnių pagrindu sukurti ir eksperimentiškai ištirti kompaktiški CMR B-skaliariniai jutikliai, skirti matuoti trumpos trukmės magnetiniams laukams didelės galios impulsinėse sistemose. Jutikliai pagaminti dviejų konfigūracijų – plonų laidų ir lanksčiosios spausdintinės plokštės – pagrindu ir sukalibruoti magnetiniuose laukuose iki 20 T. Dėl mažų matmenų ir skaliarinio atsako jie leidžia atlikti neinvazinius matavimus ribotos erdvės srityse, įskaitant iki 0,6 mm siaurumo tarpus tarp lauko koncentratoriaus ir judančios detalės, kur įprastus magnetinio lauko jutiklius panaudoti būtų sunku.
2. Sukurtas specializuotas matavimo modulis, kuris naudodamas CMR B-skaliarinius jutiklius registruoja magnetinio lauko laikinę dinamiką. Bipolinis jutiklio maitinimas ir diferencinis signalo apdorojimas eliminuoja parazitinę elektrovaros jėgą bei leidžia matuoti apie 16 μs trukmės magnetinio lauko impulsus, kurių amplitudė siekia iki 20 T.
3. Sukurtas CMR B-skaliarinis matavimo metodas leidžia iš magnetinio lauko laikinės dinamikos nustatyti būdingus magnetinio impulsinio suvirinimo etapus. Lauko ir jo išvestinės laiko atžvilgiu analizė įgalina iš pirmojo kondensatoriaus iškrovos pusperiodžio nustatyti judančios detalės deformacijos pradžią ir jos susidūrimą su nejudančia detale.
4. Judančios detalės deformacijai ir judėjimo supratimui magnetinio impulsinio suvirinimo metu, sukurtas susietas elektromagnetinis-mechaninis COMSOL Multiphysics modelis. Siekiant įvertinti nuolat kintančią geometriją judant detaliai ir jos įtaką magnetiniam laukui, modelyje įvesta deformuojama oro tarpo tarp lauko koncentratoriaus ir judančios detalės sritis, kurios baigtinių elementų tinklelio žingsnis neviršija pradinio tarpo tarp koncentratoriaus ir pačios detalės. Modelis atkartoja eksperimentiškai stebėtą judančios detalės deformaciją, magnetinio srauto tankio dinamiką ir susidūrimą su nejudančia detale: sumodeliuotas susidūrimo momentas 5% tikslumu sutampa su išmatuota susidūrimo pradžia, o sumodeliuotas magnetinio srauto tankio maksimumas yra maždaug 8% mažesnis už išmatuotąjį. Modelis taip pat leidžia apskaičiuoti judančios detalės radialinio greičio kitimą laike.

5. CMR B-skaliariniai jutikliai suteikia neinvazinę priemonę skirtą magnetinio impulsinio suvirinimo procesui sekti: judančios detalės deformacija, jos susidūrimas su nejudančia detale ir galutinė radialinė padėtis nustatomi netiesiogiai iš išmatuoto magnetinio lauko laikinės dinamikos. Dėl atstumu pagrįsto matavimo principo galutinė judančios detalės padėtis lauko koncentratoriaus atžvilgiu nustatoma iš antrojo ir vėlesnių pusperiodžių esant tai pačiai kondensatoriaus iškrovai, kurioje pirmasis pusperiodis apibūdina deformacijos ir smūgio dinamiką. Šio nustatymo neapibrėžtis kinta nuo 0,06 iki 0,14 mm ir neviršija 5,5 % nustatomo atstumo, kai atstumas tarp lauko koncentratoriaus ir judančios detalės yra nuo 1,1 iki 2,6 mm.
6. Sukurtasis magnetinio lauko matavimo modulis kartu su išmatuotos lauko dinamikos analize bei su sumodeliuotu judančios detalės smūgio greičiu ir suvirintų jungčių tempimo bandymais leidžia susieti suvirinimo parametrus ir judančios detalės deformaciją su gautos jungties kokybe. Tempimo bandymai parodė, kad jungties stiprumą lemia ne vien judančios detalės smūgio greitis: jis priklauso ir nuo lokalių susidūrimo sąlygų bei sujungimo zonos vientisumo.

PUBLIKACIJŲ SARAŠAS

Disertacijos pagrindas

(A1) Balevičius, Saulius; **Piatrou, Pavel;** Vertelis, Vilius; Stankevič, Voitech; Keršulis, Skirmantas; Dobilas, Jorūnas; Dilys, Justas; Žurauskienė, Nerija. Magnetic proximity sensor based on colossal magnetoresistance effect. Sensors and Actuators A: Physical, 375, 2024, 115518.
doi: 10.1016/j.sna.2024.115518
(A2) **Piatrou, Pavel**; Stankevic, Voitech; Zurauskiene, Nerija; Kersulis, Skirmantas; Viliunas, Mindaugas; Baskys, Algirdas; Sapurov, Martynas; Bleizgys, Vytautas; Antonovic, Darius; Plausinaitiene, Valentina; Skapas, Martynas; Vertelis, Vilius; Levitas, Borisas. "Magnetic Field Meter Based on CMR-B-Scalar Sensor for Measurement of Microsecond Duration Magnetic Field Pulses." – Sensors, 25(6), 2025, 1640.
doi: 10.3390/s25061640
(A3) **Pavel Piatrou**, Voitech Stankevic, Skirmantas Kersulis, Vilius Vertelis, Elisabetta Sieni, Vitalijus Rudzinskas, Jorunas Dobilas, Milita Vagner, Nerija Zurauskiene, Direct Measurement Of Magnetic Field Dynamics For Characterization Of Magnetic Pulse Welding Process. IEEE Access, 2026.
doi: 10.1109/ACCESS.2026.3715879

Kitos publikacijos

(A4) Sapurov, Martynas; Baskys, Algirdas; Slivka, Kazimieras; Bleizgys, Vytautas; Stasys, Karolis; Simniskis, Rimantas; Zlosnikas, Valerijus; Urbonas, Kęstutis; Dervinis, Aldas; Paulikas, Sarunas; Paulauskas, Nerijus; Pomarnacki, Raimondas; Gursnys, Darius; Mazeiko, Leslav; Cymliakova, Violeta; Piatrou, Pavel; Dilys, Justas. " RF power saving system for smart homes." – Heliyon, 10(21), 2024, e39862.
doi: 10.1016/j.heliyon.2024.e39862

Konferencijos

(C1) V. Stankevič, **P. Piatrou**, N. Žurauskienė, S. Keršulis, Magnetic Field Measurement in Magnetic Pulse Forming and Welding Systems, Workshop on IEEE MTTW Conference, Riga Technical University, Latvia, October 4-6, 2023

(C2) **P. Piatrou**, J. Dobilas, V. Stankevič, Magnetic Field Dynamics During Magnetic Pulse Forming, Workshop on IEEE MTTW Conference, Riga Technical University, Latvia, October 4-6, 2023

(C3) **P. Piatrou**, V. Vertelis, V. Stankevič, S. Keršulis, J. Dilys, V. Rudokas, V. Bleizgys, V. Plaušinaitiene, M. Viliūnas, N. Žurauskienė, Short Pulsed Magnetic Field Measurement System for Analysis of Magnetic Field Dynamics During Magnetic Pulse Welding and Forming, 10th Euro-Asian Pulsed Power Conference (EAPPC 2024), Amsterdam, Netherlands, September 22 to 26, 2024.

(C4) **P.Piatrou**, V. Stankevič, Magnetic Field Dynamics During Magnetic Pulse Forming And Crimping, FTMC Doctoral and Young Scientists Conference FizTeCh2024, October 15–17 2024

(C5) **P. Piatrou**, V. Stankevic, N. Žurauskienė, S. Keršulis, V. Vertelis, Recent Advances In The Study Of Magnetic Field Dynamics During Magnetic Pulse Crimping, 12th IEEE Workshop on Advances in Information, Electronic and Electrical Engineering (AIEEE'2025), Vilnius, Lithuania, May 15–17, 2025.

(C6) **P. Piatrou**, V. Stankevič, S. Keršulis, V. Vertelis, N. Žurauskienė Magnetic Lauko Dinamika Magnetinio Impulsinio Suvirinimo Procese. 46-oji Lietuvos nacionalinė fizikos konferencija, 2025 m. spalio 8 – 10 d. KTU, Kaunas, Lietuva

(C7) **P.Piatrou**, V. Stankevič, Investigation Of Electromagnetic Processes During Magnetic Pulse Forming And Welding, FTMC Doctoral and Young Scientists Conference FizTeCh2025 October 21–22 2025

(C8) **P. Piatrou**, V. Stankevic, S. Kersulis and N. Zurauskiene Investigation Of Transient Processes in Magnetic Pulse Welding System Using CMR B-scalar Sensors, Advanced Properties and Processes in Optoelectronic Materials and Systems (20th APROPOS), Vilnius, Lithuania, 30 September – 2 October 2026.

CURRICULUM VITAE

Pavel Piatrou
Born in 1984, Republic of Belarus.

Education

2001–2006: studies in Radiophysics and Computer Technologies, Belarusian State University; diploma thesis “Digital measurement devices”.

2006–2009: doctoral studies, Department of Radiophysics and Computer Technologies, Chair of Electronics and Nanotechnology, Belarusian State University; research topic “Spectral distribution of X-ray microbeams focused by refractive lens”.

2022–2026: doctoral studies in Natural Sciences, Physics (N 002), Center for Physical Sciences and Technology (FTMC).

Professional experience

2009–2020: teaching assistant, Chair of Electronics and Nanotechnology, Belarusian State University.

2009–2022: electronics engineer, Chair of Electronics and Nanotechnology, Belarusian State University.

2023–2024: engineer, project “Microsecond duration pulsed magnetic field meter” (No. P-TPP-23-081), FTMC.

Research interests

Physical properties of manganites and manganite-film magnetic field sensors; measurement of pulsed magnetic fields; technologies and devices for magnetic pulse welding, forming and crimping; numerical modelling of electromagnetic processes; refractive X-ray optics and Monte Carlo modelling of X-ray beam propagation.

REFERENCES

[1] W. Zhang and J. Xu, "Advanced lightweight materials for Automobiles: A review," *Materials & Design,* vol. 221, p. 110994, 2022.

[2] A. Taub, E. De Moor, A. Luo, D. K. Matlock, J. G. Speer and U. Vaidya, "Materials for Automotive Lightweighting," *Annual Review of Materials Research,* vol. 49, pp. 327-359, 2019.

[3] H. Z. Hassan and N. M. Saeed, "Advancements and applications of lightweight structures: a comprehensive review," *Discover Civil Engineering,* vol. 1, no. 1, p. 47, 2024.

[4] H. Yin, J. Liu and F. Yang, "Hybrid Structure Design of Lightweight Robotic Arms Based on Carbon Fiber Reinforced Plastic and Aluminum Alloy," *IEEE Access,* vol. 7, 2019.

[5] L. Liu, D. Ren and F. Liu, "A Review of Dissimilar Welding Techniques for Magnesium Alloys to Aluminum Alloys," *Materials (Basel, Switzerland),* vol. 7, no. 5, pp. 3735-3757, 2014.

[6] S. Zhang, X. Liu, S. Cui, H. Li, G. Mo, H. Li and H. Cai, "Study on the Microstructure and Corrosion Behavior of Dissimilar Aluminum Alloy Welded Joints Formed Using Laser Welding," *Materials,* vol. 17, no. 23, p. 5968, 2024.

[7] D. H. Kim, W. Lee, J. B. Park and J. U. Lee, "Metal Surface Treatments for Enhanced Heat Transfer in Metal–Composite Hybrid Structures," *Micromachines,* vol. 16, no. 4, p. 399, 2025.

[8] V. Psyk, D. Risch, B. Kinsey, A. Tekkaya and M. Kleiner, "Electromagnetic forming—A review," *Journal of Materials Processing Technology,* vol. 211, no. 5, pp. 787-829, 2011.

[9] R. Schäfer and P. Pasquale, "Electromagnetic pulse forming technology. Keys for allocating the industrial market segment," in *4th International Conference on High Speed Forming,* The Ohio State University, 2010.

[10] H. Dietz, H. J. Lippmann and H. Schenk, "Theorie des Magneform-Verfahrens: Erreichbarer Druck," *Elektronische Zeitschrift ETZ-A.,* vol. 88, no. 9, pp. 217-222, 1967.

[11] T. Sapanathan, R. Raoelison, N. Buiron, M. Rachik and M. Ishak, Magnetic Pulse Welding: An Innovative Joining Technology for Similar and Dissimilar Metal Pairs, London: IntechOpen, 2016.

[12] M. Kim and J. Shim, "Selection of Magnetic Pulse Crimping Process Conditions to Improve Crimped Terminal Quality," *Metals*, vol. 13, no. 11, p. 1903, 2023.

[13] J. Bellmann, S. Schettler, S. Schulze, M. Wagner, J. Standfuss, M. Zimmermann, E. Beyer and C. Leyens, "Improving and monitoring the magnetic pulse welding process between dissimilar metals," *Welding in the World*, vol. 65, no. 2, pp. 199-209, 2021.

[14] A. Kapil and A. Sharma, "Magnetic pulse welding: an efficient and environmentally friendly multi-material joining technique," *Journal of Cleaner Production*, vol. 100, pp. 35-58, 2015.

[15] A. El-Azab, M. Garnich and A. Kapoor, "Modeling of the electromagnetic forming of sheet metals: state-of-the-art and future needs," *Journal of Materials Processing Technology*, vol. 142, no. 3, pp. 744-754, 2003.

[16] R. Shotri, K. Faes and A. De, "Magnetic pulse welding of copper to steel tubes–Experimental investigation and process modelling," *Journal of Manufacturing Processes*, vol. 58, pp. 249-258, 2020.

[17] J. Bellmann, J. Lueg-Althoff, S. Schulze, S. Gies, E. Beyer and A. E. Tekkaya, "Measurement and analysis technologies for magnetic pulse welding: established methods and new strategies," *Advances in Manufacturing*, vol. 4, no. 4, pp. 322-339, 2016.

[18] V. Stankevic, J. Lueg-Althoff, M. Hahn, A. E. Tekkaya, N. Zurauskiene, J. Dilys, J. Klimantavicius, S. Kersulis, C. Simkevicius and S. Balevicius, "Magnetic Field Measurements during Magnetic Pulse Welding Using CMR-B-Scalar Sensors," *Sensors*, vol. 20, no. 20, p. 5925, 2020.

[19] J. Broeckhove, L. Willemsens, K. Faes and W. D. Waele, "Magnetic pulse welding," *International Journal of Sustainable Construction and Design*, vol. 1, no. 1, pp. 21-28, 2010.

[20] R. Merte, D. Peier and J. Teunissen, "Optical Position and Time Resolved Measurement of Magnetic Field Distribution in High Speed Metal Forming," in *1st International Conference on High Speed Forming – 2004* , Dortmund, Germany, 2004.

[21] S. Balevičius, N. Žurauskienė, V. Stankevič, T. Herrmannsdörfer, S. Zherlitsyn, Y. Skourski, F. Wolff-Fabris and J. Wosnitza, "CMR-B-Scalar Sensor Application for High Magnetic Field Measurement in Nondestructive Pulsed Magnets," *IEEE Transactions on Magnetics*, vol. 49, no. 11, pp. 5480-5484, 2013.

[22] J. R. Melcher, Continuum Electromechanics, Cambridge: MA: MIT Press, 1981.

[23] W. H. Hayt and J. A. Buck, Engineering Electromagnetics, 8th ed., New York, NY, USA: McGraw-Hill, 2010.

[24] A. Mühlbauer and E. von Finckenstein, "Magnetumformung rohrförmiger Werkstücke," *Bänder Bleche Rohre*, vol. 8, no. 2, pp. 86-92, 1967.

[25] T. Zhang, D. Chen, J. Liu, Y. Wang and Y. Qiu, "Research of an electromagnetically actuated spark gap switch," *Review of Scientific Instruments*, vol. 84, no. 11, p. 114706, 2013.

[26] S. H. Nam, H. Rahaman, H. Heo, S. S. Park, J. W. Shin, J. H. So and W. Jang, "Breakdown strength criteria of a spark gap switch in high pressure SF6 gas for pulsed power," *2009 IEEE Pulsed Power Conference*, pp. 582-586, 2009.

[27] M. Rezal, D. Ishak and M. Sabri, "High voltage magnetic pulse generation using capacitor discharge technique," *Alexandria Engineering Journal*, vol. 53, no. 4, pp. 803-808, 2014.

[28] J. Perez, T. Sugai, W. Jiang, A. Tokuchi, M. Horie, Y. Ohshio and K. Ueno, "High current pulse forming network switched by static induction thyristor," *Matter and Radiation at Extremes*, vol. 3, no. 5, pp. 261-266, 2018.

[29] E. Shahriari, T. Maysonnave, A. I. Gusev, A. S. de Ferron and L. Pecastaing, "Series–Parallel Connection of Thyristors Triggered in Impact-Ionization Wave Mode," *IEEE Transactions on Plasma Science*, vol. 52, no. 9, pp. 4286-4293, 2024.

[30] W. H. Hayt, J. E. Kemmerly and S. M. Durbin, Engineering Circuit Analysis, 9th ed., New York: NY: McGraw-Hill Education, 2019.

[31] C. Khalil, S. Marya and G. Racineux, "Magnetic Pulse Welding and Spot Welding with Improved Coil Efficiency—Application for

Dissimilar Welding of Automotive Metal Alloys," *Journal of Manufacturing and Materials Processing,* vol. 4, no. 3, p. 69, 2020.

[32] C. Weddeling, O. K. Demir, P. Haupt and A. E. Tekkaya, "Analytical methodology for the process design of electromagnetic crimping," *Journal of Materials Processing Technology,* vol. 222, pp. 163-180, 2015.

[33] P. Zhang, M. Kimchi, H. Shao, J. E. Gould and G. S. Daehn, "Analysis of the Electromagnetic Impulse Joining Process with a Field Concentrator," *AIP Conference Proceedings,* vol. 712, no. 1, pp. 1253-1258, 2004.

[34] K. Sofi, M. Hamzaoui, H. Elidrissi, A. Nait Sidi Moh and A. Hamzaoui, "Experimental study of magnetic pulse generator and the field shaper effect on the current pulse," *Renewable Energies, Power Systems & Green Inclusive Economy (REPS-GIE),* pp. 1-5, 2018.

[35] S. Dond, T. Kolge, H. Choudhary, A. Sharma and G. Dey, "Determination of magnetic coupling and its influence on the electromagnetic tube forming and discharge circuit parameters," *Journal of Manufacturing Processes,* vol. 54, pp. 19-27, 2020.

[36] J. Lueg-Althoff, A. Lorenz, S. Gies, C. Weddeling, G. Goebel, A. E. Tekkaya and E. Beyer, "Magnetic Pulse Welding by Electromagnetic Compression: Determination of the Impact Velocity," *Advanced Materials Research,* Vols. 966-967, pp. 489-499, 2014.

[37] H. Dietz, H. J. Lippmann and H. Schenk, "Theorie des Magneform-Verfahrens: Die Bewegung," *ETZ – A,* vol. 89, no. 12, pp. 273-278, 1968.

[38] R. Shotri, K. Faes, G. Racineux and A. De, "Improved Coil Design for Magnetic Pulse Welding of Metallic Sheets," *Journal of Manufacturing and Materials Processing,* vol. 6, no. 6, p. 144, 2022.

[39] H. Zhang, X. Li and H. Ding, "Optimization design and experimental verification of magnetic pulse spot welding system of dissimilar metal sheets based on a field shaper," *Scientific Reports,* vol. 16, no. 1, p. 3228, 2025.

[40] E. Paese, M. Geier, J. L. Pacheco, R. P. Homrich and J. C. S. Ortiz, "Mathematical modeling of an electromagnetic forming

system with flat spiral coils as actuator," in *4th International Conference on High Speed Forming*, Ohio, USA, 2010.

[41] H.-G. Noh, W.-J. Song, B.-S. Kang and J. Kim, "Two-step electromagnetic forming process using spiral forming coils to deform sheet metal in a middle-block die," *The International Journal of Advanced Manufacturing Technology*, vol. 76, no. 9, pp. 1691-1703, 2015.

[42] K. Faes, R. Shotri and A. De, "Probing Magnetic Pulse Welding of Thin-Walled Tubes," *Journal of Manufacturing and Materials Processing*, vol. 4, no. 4, p. 118, 2020.

[43] O. Zaitov and V. A. Kolchuzhin, "Bitter coil design methodology for electromagnetic pulse metal processing techniques," *Journal of Manufacturing Processes*, vol. 16, no. 4, pp. 551-562, 2014.

[44] Y. B. Kim and E. D. Platner, "Flux Concentrator for High-Intensity Pulsed Magnetic Fields," *Review of Scientific Instruments*, vol. 30, no. 7, pp. 524-533, 1959.

[45] G. Babat and M. Losinsky, "Concentrator of Eddy Currents for Zonal Heating of Steel Parts," *Journal of Applied Physics*, vol. 11, no. 12, pp. 816-823, 1940.

[46] E. Zaytsev, V. Krutikov, A. Spirin and S. Paranin, "Development of Multi-Part Field-Shapers for Magnetic Pulse Welding Using Nanostructured Cu-Nb Composite," *Journal of Manufacturing and Materials Processing*, vol. 8, no. 3, p. 97, 2024.

[47] H. Zhang, N. Liu, X. Li, F. Deng, Q. Wang and H. Ding, "A novel field shaper with slow-varying central hole for electromagnetic pulse welding of sheet metal," *The International Journal of Advanced Manufacturing Technology*, vol. 108, no. 7, pp. 2595-2606, 2020.

[48] K. S. Gavel, M. Ahmed, A. Ali, H. N. Bhargaw, S. K. Panthi and A. Bhargav, "A novel tool design for magnetic pulse welding of sheet metal using compression coil," *Journal of Manufacturing Processes*, vol. 144, pp. 261-277, 2025.

[49] G. Avrillaud, G. Mazars, E. Cantergiani, F. Beguet, J.-P. Cuq-Lelandais and J. Deroy, "Examples of How Increased Formability through High Strain Rates Can Be Used in Electro-Hydraulic Forming and Electromagnetic Forming Industrial Applications,"

Journal of Manufacturing and Materials Processing, vol. 5, no. 3, p. 96, 2021.

[50] D. Oliveira, M. Worswick, M. Finn and D. Newman, "Electromagnetic forming of aluminum alloy sheet: Free-form and cavity fill experiments and model," *Journal of Materials Processing Technology*, vol. 170, no. 1, pp. 350-362, 2005.

[51] A. Stern, V. Shribman, A. Ben-Artzy and M. Aizenshtein, "Interface Phenomena and Bonding Mechanism in Magnetic Pulse Welding," *Journal of Materials Engineering and Performance*, pp. 3449-3458, 2014.

[52] B. Crossland and J. D. Williams, "Explosive welding," *Metallurgical reviews*, vol. 15, no. 1, pp. 79-100, 1970.

[53] M. Abdul Karim and Y.-D. Park, "A Review on Welding of Dissimilar Metals in Car Body Manufacturing," *Journal of Welding and Joining*, vol. 38, no. 1, pp. 8-23, 2020.

[54] A. Sadeghian and N. Iqbal, "A review on dissimilar laser welding of steel-copper, steel-aluminum, aluminum-copper, and steel-nickel for electric vehicle battery manufacturing," *Optics & Laser Technology*, vol. 146, p. 107595, 2022.

[55] W. Cai, G. Daehn, A. Vivek, J. Li, H. Khan, R. S. Mishra and M. Komarasamy, "A State-of-the-Art Review on Solid-State Metal Joining," *Journal of Manufacturing Science and Engineering*, vol. 141, no. 3, 2019.

[56] K.-i. Mori, N. Bay, L. Fratini, F. Micari and A. E. Tekkaya, "Joining by plastic deformation," *CIRP Annals*, vol. 62, no. 2, pp. 673-694, 2013.

[57] G. R. Cowan, O. R. Bergmann and A. H. Holtzman, "Mechanism of bond zone wave formation in explosion-clad metals," *Metallurgical Transactions*, vol. 2, no. 11, pp. 3145-3155, 1971.

[58] K. Wang, H. Wang, H. Zhou, W. Zheng and A. Xu, "Research Status and Prospect of Laser Impact Welding," *Metals*, vol. 10, no. 11, p. 1444, 2020.

[59] J. Li, R. Raoelison, T. Sapanathan, Y. Hou and M. Rachik, "Interface evolution during magnetic pulse welding under extremely high strain rate collision: mechanisms,

thermomechanical kinetics and consequences," *Acta Materialia,* vol. 195, pp. 404-415, 2020.

[60] R. Raoelison, N. Buiron, M. Rachik, D. Haye and G. Franz, "Efficient welding conditions in magnetic pulse welding process," *Journal of Manufacturing Processes,* vol. 14, no. 3, pp. 372-377, 2012.

[61] H. Yu, Z. Fan and C. Li, "Magnetic pulse cladding of aluminum alloy on mild steel tube," *Journal of Materials Processing Technology,* vol. 214, no. 2, pp. 141-150, 2014.

[62] K. Faes, W. De Waele, M. Müller and H. Cramer, "Design of Electromagnetic Pulse Crimp Torque Joints," in *6th International Conference on High Speed Forming*, Dortmund, Germany, 2014.

[63] Z. Zimniak, "Plastic Deformation Zone in Electromagnetic Cutting," *Archives of Metallurgy and Materials,* vol. 62, no. 4, pp. 2303-2308, 2017.

[64] J. Bellmann, E. Beyer, J. Lueg-Althoff, S. Gies, A. E. Tekkaya and S. Schulze, "Measurement of Collision Conditions in Magnetic Pulse Welding Processes," *Journal of Physical Science and Application,* vol. 7, no. 4, pp. 1-10, 2017.

[65] S. Veenaas, F. Vollertsen, M. Krüger, F. Meyer and M. Hartmann, "Determination of Forming Speed at a Laser Shock Stretch Drawing Process," in *7th International Conference on High Speed Forming*, Dortmund, Germany, 2016.

[66] D. H. Dolan, "Extreme measurements with Photonic Doppler Velocimetry (PDV)," *Review of Scientific Instruments,* vol. 91, no. 5, p. 051501, 2020.

[67] A. Jäger and A. E. Tekkaya, "Online measurement of the radial workpiece displacement in electromagnetic forming subsequent to hot aluminum extrusion," in *Proceedings of the 5th International Conference on High-Speed Forming*, Dortmund, Germany, 2012.

[68] J. R. Johnson, G. Taber, A. Vivek, Y. Zhang, S. Golowin, K. Banik, G. K. Fenton and G. S. Daehn, "Coupling Experiment and Simulation in Electromagnetic Forming Using Photon Doppler Velocimetry," *Steel Research International,* vol. 80, no. 5, pp. 359-365, 2009.

[69] M. Watanabe and S. Kumai, "High-Speed Deformation and Collision Behavior of Pure Aluminum Plates in Magnetic Pulse

Welding," *Materials Transactions,* vol. 50, no. 8, pp. 2035-2042, 2009.

[70] D. J. Sadler and C. H. Ahn, "On-chip eddy current sensor for proximity sensing and crack detection," *Sensors and Actuators A: Physical,* vol. 91, no. 3, pp. 340-345, 2001.

[71] X. Xue, Y. Dong and X. Wu, "Motion Induced Eddy Current Sensor for Non-Intrusive Vibration Measurement," *IEEE Sensors Journal,* vol. 20, no. 2, pp. 735-744, 2020.

[72] K. Kosmas, C. Sargentis, D. Tsamakis and E. Hristoforou, "Non-destructive evaluation of magnetic metallic materials using Hall sensors," *Journal of Materials Processing Technology,* vol. 161, no. 1, pp. 359-362, 2005.

[73] C. Zheng, K. Zhu, S. Cardoso de Freitas, J. -Y. Chang, J. E. Davies, P. Eames, P. P. Freitas, O. Kazakova, C. Kim, C. -W. Leung, S. -H. Liou, A. Ognev, S. N. Piramanayagam, P. Ripka, A. Samardak, K. -H. Shin, S. -Y. Tong, M. -J. Tung, S. X. Wang, S. Xue, X. Yin and P. W. T. Pong, "Magnetoresistive Sensor Development Roadmap (Non-Recording Applications)," *IEEE Transactions on Magnetics,* vol. 55, no. 4, pp. 1-30, 2019.

[74] T. Chady, "Evaluation of stress loaded steel samples using GMR magnetic field sensor," *IEEE Sensors Journal,* vol. 2, no. 5, pp. 488-493, 2002.

[75] A. S. A. Kumar, B. George and S. C. Mukhopadhyay, "Technologies and Applications of Angle Sensors: A Review," *IEEE Sensors Journal,* vol. 21, no. 6, pp. 7195-7206, 2021.

[76] S.-C. Wang, B.-R. Xie and S.-M. Huang, "Design and Analysis of Small Size Eddy Current Displacement Sensor," *Sensors,* vol. 22, no. 19, p. 7444, 2022.

[77] A. D. Eslamlou, A. Ghaderiaram, E. Schlangen and M. Fotouhi, "A review on non-destructive evaluation of construction materials and structures using magnetic sensors," *Construction and Building Materials,* vol. 397, p. 132460, 2023.

[78] E. Dagotto, T. Hotta and A. Moreo, "Colossal magnetoresistant materials: the key role of phase separation," *Physics Reports,* vol. 344, no. 1, pp. 1-153, 2001.

[79] D. Pla, C. Jimenez and M. Burriel, "Engineering of Functional Manganites Grown by MOCVD for Miniaturized Devices," *Advanced Materials Interfaces,* vol. 4, no. 8, 2017.

[80] V. I. Krutikov, "Welding of Steel Parts and Compaction of Iridium Nanopowders by Compression of Conductive Shells in Pulsed Magnetic Fields, Cand. Sci. (Tech.) dissertation," Institute of Electrophysics, Ural Branch of the Russian Academy of Sciences, Yekaterinburg, 2020 [In Russian].

[81] O. A. Mironov, S. Zherlitsyn, M. Uhlarz, Y. Skourski, T. Palewski and J. Wosnitza, "Microminiature Hall Probes for Applications at Pulsed Magnetic Fields up to 87 Tesla," *Journal of Low Temperature Physics,* vol. 159, no. 1, pp. 315-318, 2010.

[82] J. M. D. Coey, M. Viret and S. von Molnár, "Mixed-valence manganites," *Advances in Physics,* vol. 48, no. 2, pp. 167-293, 1999.

[83] A. Urushibara, Y. Moritomo, T. Arima, A. Asamitsu, G. Kido and Y. Tokura, "Insulator-metal transition and giant magnetoresistance in La1−*x*Sr*x*MnO3," *Physical Review B,* vol. 51, no. 20, pp. 14103-14109, 1995.

[84] O. Vitayaya, P. Z. Zul Nehan, D. R. Munazat, M. T. E. Manawan and B. Kurniawan, "Magnetoresistance (MR) properties of magnetic materials," *RSC Advances,* vol. 14, no. 26, p. 18617, 2024.

[85] S. Balevičius, N. Žurauskienė, V. Stankevič, S. Keršulis, A. Abrutis and V. Plaušinaitienė, "Electrical Conductivity of Thin Polycrystalline La0.83Sr0.17MnO3 Films in Pulsed High Electric and Magnetic Fields," *Journal of Low Temperature Physics,* vol. 159, no. 1, pp. 68-71, 2010.

[86] N. Zurauskiene, V. Stankevic, S. Kersulis, M. Vagner, V. Plausinaitiene, J. Dobilas, R. Vasiliauskas, M. Skapas, M. Koliada, J. Pietosa and A. Wisniewski, "Enhancement of Room-Temperature Low-Field Magnetoresistance in Nanostructured Lanthanum Manganite Films for Magnetic Sensor Applications," *Sensors,* vol. 22, no. 11, p. 4004, 2022.

[87] T. Stankevič, L. Medišauskas, V. Stankevič, S. Balevičius, N. Žurauskienė, O. Liebfried and M. Schneider, "Pulsed magnetic field measurement system based on colossal magnetoresistance-B-scalar sensors for railgun investigation," *Review of Scientific Instruments,* vol. 85, no. 4, p. 044704, 2014.

[88] M. Schneider, O. Liebfried, V. Stankevic, S. Balevicius and N. Zurauskiene, "Magnetic Diffusion in Railguns: Measurements Using CMR-Based Sensors," *IEEE Transactions on Magnetics*, vol. 45, no. 1, pp. 430-435, 2009.

[89] V. Stankevič, S. Keršulis, J. Dilys, V. Bleizgys, M. Viliūnas, V. Vertelis, A. Maneikis, V. Rudokas, V. Plaušinaitienė and N. Žurauskienė, "Measurement System for Short-Pulsed Magnetic Fields," *Sensors*, vol. 23, no. 3, p. 1435, 2023.

[90] N. Žurauskienė, V. Stankevič, S. Keršulis, J. Klimantavičius, Č. Šimkevičius, V. Plaušinaitienė, M. Vagner and S. Balevičius, "Increase of Operating Temperature of Magnetic Field Sensors Based on La–Sr–Mn–O Films With Mn Excess," *IEEE Transactions on Plasma Science*, vol. 47, no. 10, pp. 4530-4535, 2019.

[91] S. Balevičius, N. Žurauskienė, V. Stankevič, S. Keršulis, A. Baskys, V. Bleizgys, J. Dilys, A. Lucinskis, A. Tyshko and S. B. Brazil, "Hand-Held Magnetic Field Meter Based on Colossal Magnetoresistance-B-Scalar Sensor," *IEEE Transactions on Instrumentation and Measurement*, vol. 69, pp. 2808-2816, 2020.

[92] S. Balevičius, N. Žurauskienė, V. Stankevič, T. Stankevič, J. Novickij and M. Schneider, "High-Frequency CMR-B-Scalar Sensor for Pulsed Magnetic Field Measurement," *IEEE Transactions on Plasma Science*, vol. 41, no. 10, pp. 2885-2889, 2013.

[93] L. Xianlong, H. Liang and L. Jianjun, "An experiment and simulation study of the rebound effect in electromagnetic forming process," in *6th International Conference on High Speed Forming*, Dortmund, Germany, 2014.

[94] H. Ma, L. Huang, J. Li, X. Duan and F. Ma, "Effects of process parameters on electromagnetic sheet free forming of aluminium alloy," *The International Journal of Advanced Manufacturing Technology*, vol. 96, no. 1, pp. 359-369, 2018.

[95] J. Esmaeili, A. Asgharpour, M. Bakhshi-Jooybari, H. Gorji and M. J. Mirnia, "Experimental and numerical study of forming aluminum stepped tubes by electromagnetic forming method," *Discover Materials*, vol. 5, no. 1, p. 138, 2025.

[96] V. Psyk, C. Hofer, K. Faes, C. Scheffler and E. Scherleitner, "Testing of magnetic pulse welded joints – Destructive and non-

destructive methods," *AIP Conference Proceedings,* vol. 2113, no. 1, p. 050010, 2019.

[97] M. Lai, X. Liu, S. Wang, H. Jiang, G. Li and J. Cui, "Realizing quality inspection in magnetic pulse crimping manufacturing: Using Steger algorithm and self-attention," *Journal of Materials Processing Technology,* vol. 311, p. 117799, 2023.

[98] J. Lueg-Althoff, B. Schilling, J. Bellmann, S. Gies, S. Schulze, A. E. Tekkaya and E. Beyer, "Influence of the Wall Thicknesses on the Joint Quality During Magnetic Pulse Welding in Tubeto-Tube Configuration," in *7th International Conference on High Speed Forming*, Dortmund, Germany, 2016.

[99] Z. Xu, J. Cui, H. Yu and C. Li, "Research on the impact velocity of magnetic impulse welding of pipe fitting," *Materials and Design,* vol. 49, pp. 736-745, 2013.

[100] J. Li, S. Muraishi and S. Kumai, "Experimental and Numerical Analyses of Wavy Interface Formation and Local Melting Phenomena at the Magnetic Pulse Welded Al/Fe Joint Interface," *Materials Transactions,* vol. 62, no. 8, pp. 1184-1193, 2021.

[101] P. L'Eplattenier, I. Caldichoury and J. Anton, "LS-Dyna R7: Update on the electromagnetism module (EM)," in *9th European LS-Dyna Conference Manchester*, Manchester, UK, 2013.

[102] P. Groche and C. Pabst, "Numerical simulation of impact welding processes with LS-Dyna," in *10th European LS-Dyna Conference 2015*, Wurzburg, Germany, 2015.

[103] O. K. Demir, V. Psyk and A. E. Tekkaya, "Simulation of Wrinkle Formation in Free Electromagnetic Tube Compression," in *4th International Conference on High Speed Forming*, Dortmund, Germany, 2010.

[104] J. Körner, G. Göbel, B. Brenner and E. Beyer, "Numerical Simulation of Magnetic Pulse Welding: Insights and Useful Simplifications," in *5th International Conference on High Speed Forming*, Dortmund, Germany, 2012.

[105] A. Amardas and B. R. Doshi, "3-D Magneto-Structural Analysis of Magnetic Pulse Welding (MPW)," in *COMSOL Conference*, Bangalore, 2019.

[106] A. R. Dhiware, S. D. Kore and M. R. Kulkarni, "Numerical and Experimental Studies on Electromagnetic Pulse Crimping of

Joining D9 Steel Tube on SS316L (N) Plug," in *10th International Conference on High Speed Forming*, Dortmund, Germany, 2025.

[107] P. Piatrou, V. Stankevic, N. Zurauskiene, S. Kersulis, M. Viliunas, A. Baskys, M. Sapurov, V. Bleizgys, D. Antonovic, V. Plausinaitiene, M. Skapas, V. Vertelis and B. Levitas, "Magnetic Field Meter Based on CMR-B-Scalar Sensor for Measurement of Microsecond Duration Magnetic Field Pulses," *Sensors*, vol. 25, no. 6, p. 1640, 2025.

[108] R. Drehmann, C. Scheffler, S. Winter, V. Psyk, V. Kräusel and T. Lampke, "Experimental and Numerical Investigations into Magnetic Pulse Welding of Aluminum Alloy 6016 to Hardened Steel 22MnB5," *Journal of Manufacturing and Materials Processing*, vol. 5, no. 3, p. 66, 2021.

[109] C. Khalil, S. Marya and G. Racineux, "Magnetic Pulse Welding and Spot Welding with Improved Coil Efficiency—Application for Dissimilar Welding of Automotive Metal Alloys," *Journal of Manufacturing and Materials Processing*, vol. 4, no. 3, p. 69, 2020.

[110] M. Kleiner and A. Brosius, "Determination of Flow Curves at High Strain Rates using the Electromagnetic Forming Process and an Iterative Finite Element Simulation Scheme," *CIRP Annals*, vol. 55, no. 1, pp. 267-270, 2006.

[111] A. Grainys, J. Novickij, T. Stankevič, V. Stankevič, V. Novickij and N. Žurauskienė, "Single Pulse Calibration of Magnetic Field Sensors Using Mobile 43 kJ Facility," *Measurement Science Review*, vol. 15, no. 5, pp. 244-247, 2015.

[112] P. B. Tavares, V. S. Amaral, J. P. Araújo, J. B. Sousa, A. A. C. S. Lourenço and J. M. Vieira, "Substrate, annealing, and Mn excess effects on La–Ca–MnO3 thin films grown by metalorganic chemical vapor deposition: A way to room-temperature Tc," *Journal of Applied Physics*, vol. 85, no. 8, pp. 5411-5413, 1999.

[113] H. Yu, Z. Xu, Z. Fan, Z. Zhao and C. Li, "Mechanical property and microstructure of aluminum alloy-steel tubes joint by magnetic pulse welding," *Materials Science and Engineering: A*, vol. 561, pp. 259-265, 2013.

Vilniaus universiteto leidykla
Saulėtekio al. 9, III rūmai, LT-10222 Vilnius
El. p. info@leidykla.vu.lt, www.leidykla.vu.lt
bookshop.vu.lt, journals.vu.lt
Tiražas 25 egz.